1996

Finite element modeling of ultrasonic wave propagation with application to acoustic microscopy

Tianji Xue
Iowa State University

INFORMATION TO USERS

This manuscript has been reproduced from the microfilm master. UMI films the text directly from the original or copy submitted. Thus, some thesis and dissertation copies are in typewriter face, while others may be from any type of computer printer.

The quality of this reproduction is dependent upon the quality of the copy submitted. Broken or indistinct print, colored or poor quality illustrations and photographs, print bleedthrough, substandard margins, and improper alignment can adversely affect reproduction.

In the unlikely event that the author did not send UMI a complete manuscript and there are missing pages, these will be noted. Also, if unauthorized copyright material had to be removed, a note will indicate the deletion.

Oversize materials (e.g., maps, drawings, charts) are reproduced by sectioning the original, beginning at the upper left-hand corner and continuing from left to right in equal sections with small overlaps. Each original is also photographed in one exposure and is included in reduced form at the back of the book.

Photographs included in the original manuscript have been reproduced xerographically in this copy. Higher quality 6" x 9" black and white photographic prints are available for any photographs or illustrations appearing in this copy for an additional charge. Contact UMI directly to order.

UMI

A Bell & Howell Information Company
300 North Zeeb Road, Ann Arbor MI 48106-1346 USA
313/761-4700 800/521-0600

Finite element modeling of ultrasonic wave propagation with application to acoustic microscopy

by

Tianji Xue

A Dissertation Submitted to the

Graduate Faculty in Partial Fulfillment of the

Requirements for the Degree of

DOCTOR OF PHILOSOPHY

Department: Electrical and Computer Engineering
Major: Electrical Engineering (Electromagnetics)

Approved:

Signature was redacted for privacy.

In Charge of Major Work

Signature was redacted for privacy.

For the Major Department

Signature was redacted for privacy.

For the Graduate College

Members of the Committee:

Signature was redacted for privacy.

Signature was redacted for privacy.

Signature was redacted for privacy.

Signature was redacted for privacy.

Iowa State University
Ames, Iowa
1996

TABLE OF CONTENTS

LIST OF FIGURES

CHAPTER 1. INTRODUCTION

Nondestructive evaluation (NDE) plays a very important role in modern industries, such as aerospace, transportation, electronic and nuclear engineering. It involves the detection and characterization of flaws in materials and devices to predict and prevent failure. Among the major techniques for NDE, the ultrasonic method [1,2] is probably the most versatile due to the capability of ultrasound to penetrate a wide range of media. The acoustic microscope [3] is an advanced ultrasonic measurement and imaging system developed for the achievement of superior resolution.

Even though NDE is essentially an inverse process, its realization is largely based on a valid forward model covering the energy/material interaction process. A firm understanding of the interaction is critical for correctly interpreting measurement data. In this work a finite element model is developed for ultrasonic systems with emphasis on the acoustic microscope. Numerous wave/material or defect interaction phenomena are characterized..

Ultrasonic NDE and Acoustic Microscopy

It is well known that the sound wave, which can propagate in both fluid and solid media, is a common means of communication. The frequency for this purpose is generally below twenty kilohertz. When the frequency goes above this limit the

sound is known as ultrasound which is inaudible to the human being but finds wide applications in nondestructive evaluation. With ultrasonic transmission through or reflection from some material or device, the characteristics of the medium are detected without changing its state. Unlike electromagnetic waves, such as light, which can propagate through vacuum, ultrasound is a mechanical wave which propagates by the oscillations of the particles in the medium. But the underlying principles and formulations of the two types of energy are similar.

Traditional ultrasonic measurement and imaging have been performed at intermediate frequencies with wavelengths in the order of millimeters. The acoustic microscope, which utilizes focused ultrasound at hundreds of megahertz or even a few gigahertz, can have comparable wavelength, and therefore resolution, to the optical microscope since the velocity of ultrasound is five orders lower than that of light in fluid media [4]. The idea of the acoustic microscope originated with Sokolov. With extensive research and development over the last several decades, notably by the work of Quate et al. [5], the acoustic microscope has become a powerful tool for ultrasonic NDT. With this instrument, high contrast micrographs can be obtained which contain unique information not available in other imaging tools and the elastic properties of optically opaque materials can be determined. It is particularly suitable for detecting surface and subsurface defects in metal and ceramic materials and for examining integrated circuits and biological cells.

Figure 1.1 is a block diagram of a typical scanning acoustic microscope system operating in the reflection mode. The computer is for general control and data acquisition. It also contains devices for data/image processing and display. The pulser/receiver generates the high voltage pulses which excite the piezoelectric (usu-

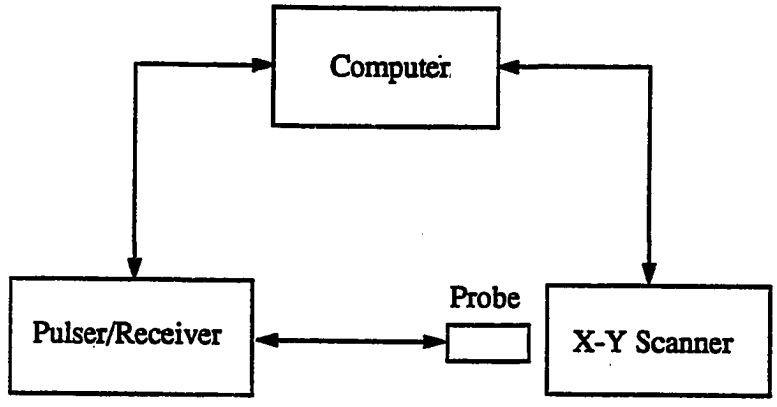

Figure 1.1: System diagram for the scanning acoustic microscope.

ally zinc oxide) transducer on the probe and also collects reflected signals. With the x-y scanner, the probe is scanned in a raster fashion with respect to the specimen to form a complete image. A detailed structure for the probe is shown in Figure 1.2. The lens rod is made of material such as sapphire and fused quartz, etc., which support high ultrasonic velocity. A liquid, typically water, serves as the coupling medium between the lens and the sample, since ultrasound decays dramatically in the air. When the ultrasonic pulse generated from the piezoelectric transducer reaches the spherical lens surface, it will be focused into the coupling medium with negligible aberration, because of the large ratio of the ultrasonic velocities in the solid and liquid media. A reflection also occurs at the interface although it can be significantly reduced by a quarter wavelength matching layer. The sample is normally placed in the focal plane

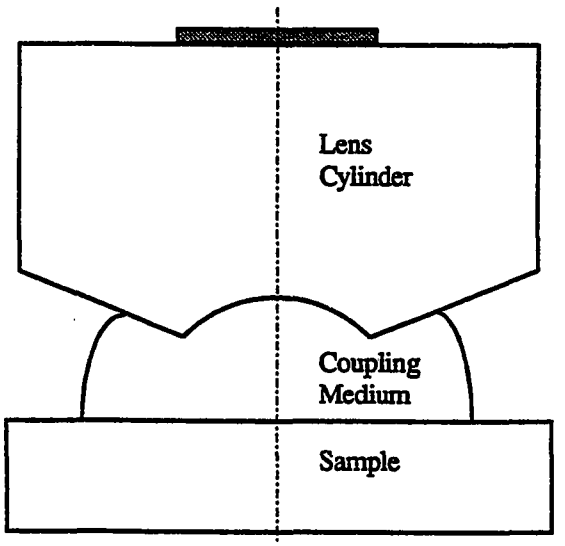

Figure 1.2: The ultrasonic probe configuration.

of the lens. With negative defocusing, however, a new contrast mechanism will take effect due to the excitation of leaky Rayleigh waves along the sample surface.

The lateral resolution is obtained by focusing radiation to a diffraction-limited spot. As with optical microscopes

$$\Delta = 0.61\lambda f/a = 0.61\lambda/NA \tag{1.1}$$

where f is the focal length, a is the radius of the lens aperture, and $NA = a/f$ is the numerical aperture of the microscope. So it is obvious that shorter wavelength or higher frequency will yield better resolution, which comes at the expense of reduced penetration since the attenuation of the ultrasonic waves in water is generally proportional to the square of frequency [6]. By using low attenuation couplants such as liquid helium the operating frequency can be raised and the resolution can be improved to a level better than that of the corresponding optical microscope. The axial resolution is determined by the bandwidth of the ultrasonic pulse [7]. Shorter

pulses have larger bandwidth and give increased axial resolution.

The acoustic microscope is not only used for imaging but also for ultrasonic measurement of material properties. A basic measurement model of the reflection system, excluding the electromechanical effect, can be represented as

$$y(t) = x(t) * h_1(t) * h_2(t) * h_3(t) * f(t) * h_3(t) * h_2(t) * h_1(t) = h(t) * f(t) \quad (1.2)$$

where $y(t)$ is the output signal, $x(t)$ is pulse generated by the transducer, h_1, h_2 and h_3 are the impulse response functions of the lens, the coupling medium and the specimen respectively, and $f(t)$ is the scattering function or object function of the flaw. $h(t)$ is used for the overall nonscattering response of the system or simply noted as the system response function. In the frequency domain,

$$Y(\omega) = H(\omega)F(\omega) \quad (1.3)$$

Then F can be determined by the ratio of Y and H and its inverse Fourier transform yields the defect function. Thus a thorough knowledge of the system function is of fundamental importance. Obviously, a boundary value problem with coupled elastodynamic and acoustic governing equations has to be solved.

Review of Solution Methods

The modeling of the complete acoustic microscope system is a complicated process. Through the following brief review of available solution methods, a numerical procedure is found to be necessary.

Analytical methods

In predicting the perturbed fields caused by the inhomogeneities and defects, the governing equations need to be solved with appropriate boundary conditions. Purely analytical solutions, if available, are of course desirable. The most common analytical procedure is the separation of variables in which the solutions are expressed in terms of eigenfunction expansions. Problem geometries have to fit in limited coordinate systems for the governing equation to be separable [8]. Early works in this categories include the elastic wave scattering by cylindrical discontinuities [9], by spherical obstacles [10], and a penny-shaped cracks in unbounded or half-plane solids [11]. A comprehensive treatment is presented in [12]. Because of the strict limitation of this approach, various approximations have been introduced to extend it to more general problems. The following are brief outlines of the Born approximation, the Kirchhoff approximation, the T-matrix approach and the geometrical theory of diffraction (GTD).

In the Born and quasistatic approximation [13] the displacements are represented in terms of the Born series expansion. If only the first term is kept, the displacements in the scatterer are simply approximated by the incident fields. This approach is suitable for low frequencies and therefore weak scattering under which condition the scattered displacements can be easily obtained. Explicit inverse schemes have also been developed with the Born approximation for characterizing simple defect shapes [14].

The Kirchhoff approximation [15,16] assumes that the illuminated side of crack acts as a specular reflector to the incident field and the other side has a zero wavefield. The Kirchhoff approximation is a high frequency approximation which is valid for

large scatterer size with respect to the wavelength. The approach is suited for surface problems with edges for which both the reflected and diffracted wavefields can be accurately predicted. For half-space cracks the approach fails to predict the reflected compressional and shear waves as well as the critical angle head wave.

The geometrical theory of diffraction (GTD) [17,18] is an extension of the traditional ray theory in optics which introduces diffracted rays through the generalization of Fermat's principle. It is a high frequency approximation based on a series expansion in terms of the inverse powers of frequency. The GTD fails at shadow boundaries and caustic surfaces. This difficulty has been overcome with the development of the uniform geometrical theory of diffraction (UTD). A more efficient way is to use the Kirchhoff approximation at these singular surfaces [18].

For crack dimensions comparable to the wavelength, the transition matrix (T-matrix) method [19,20] is a suitable choice. In this approach, the governing equation is represented in terms of a surface integral over the scatterer. Both the incident and scattered fields are expanded by a set of orthogonal basis functions. Then a matrix equation is derived relating the scattered and the incident fields and incorporating the boundary conditions. The resulting T-matrix can be truncated at an appropriate point for numerical evaluation [21]. This method has been applied for various scatterers under the time-harmonic condition. However, ill-conditioned T-matrix could result for scatterers of particular geometries. In this approach some effort may be required in formulating the basis functions and in performing the intensive numerical computations.

Additional approaches include the Cagniard-de Hoop method [22], which was developed for the study of transient wave propagation by utilizing integral transforms..

Numerical methods

It is seen that the analytical approaches are either restricted to problems of simple geometries or subject to assumptions that may not be realistic. This has motivated the development of fully numerical procedures with the availability of modern electronic computers. The most widely accepted numerical methods for solving boundary value problems (BVP) include the finite difference method (FDM), the finite element method (FEM) and the boundary element method (BEM).

The finite difference method is conceptually a simple approach. In this method the problem domain is usually divided into uniform meshgrids, and the derivatives in the governing differential equations are approximated by the corresponding parameter differences among neighboring grids based on the Taylor series expansion. A system of algebraic equations results from all the difference equations for unknowns each grid node incorporating the appropriate boundary conditions. For transient elastic wave propagation problems, the system of equations is formulated at discretized times and the time-stepping process can be performed by either explicit or implicit approaches. The explicit finite difference schemes for the study of elastic wave problems were initiated by Alterman and coworkers [23]. Valuable tools based on the FDM have been developed for ultrasonic NDE. Finite difference models for the ultrasonic transducer fields have been reported by Harumi et al. [24], as well as by Rose and Meyer [25]. Interaction models of body or surface waves with targets or discontinuities have been studied by Bond et al. [26,27]. More recently, the implementation of the method has been carried out on connection machines (CE) to raise the computational efficiency [28]. However, the application of the method is limited in that it is incapable or weak in handling problems of more complex geometry with appropriate boundary

conditions.

In the finite element method, the governing differential equations are reformulated in the form of integral equations using either the variational principle or the weighted-residual principle. The problem domain is also discretized into meshes of elements. But unlike finite difference meshes, the finite element meshes are usually non-uniform to handle complex geometries. The minimization of the so called functional, which represents the internal energy of the formulated system, or the evaluation of the weighted residuals leads to a system of linear equations. This actually involves two steps, the matrix equations are derived for each element and the assembly of all the elemental matrix equations yields the global matrix equation. The final solution explicitly incorporates the appropriate boundary conditions.

The FEM is the most popular numerical technique in engineering analysis. Originally developed for application to solid mechanics and structure analysis, the method has subsequently been applied to every branch of engineering and physical science following the establishment of its mathematical foundation. The work on fields and wave propagation problems can be dated back to Lysmer and Drake [29] who applied the method in seismology. Their work on surface waves was later extended by Smith [30] to the application of body waves in seismology. The applications of the finite element method for solid/fluid interaction has been reported by different authors [30-33]. The time-dependent finite element formulation of wave/crack interaction was reported by Bazant et al. [34]. A more comprehensive finite element model for ultrasonic NDE has been developed by Lord and coworkers [35-41],originally for 2D isotropic media and later extended to more general anisotropic and attenuative media. Though the finite element method is powerful in terms of versatility in handling

complex geometries, its applications are usually confined to 2D and axisymmetric problems. General 3D implementations may require enormous computer resources in terms of memory, storage and CPU time, especially for transient problems which adopt explicit or implicit time integration schemes.

In the boundary element method, the governing equations are represented by a system of boundary integral equations (BIE) and therefore the integrated unknown parameters appear only in the integrals over the boundary. The boundary is discretized into piece-wise sub-boundaries called boundary elements in a similar fashion to that of the finite element method but the dimensionality is reduced by one. The unknowns at any position inside the problem domain can be evaluated directly following the determination of the boundary solutions. Thus, the BEM is a more efficient approach for dealing with arbitrary 3D geometries than the finite element method and is the ideal method for problems with infinite domains such as in solid mechanics, fluid mechanics and acoustics, etc. The ideas of the boundary element method have been applied in acoustics and structural analysis. The application of the method for general transient elastodynamics was initiated by Cruse and Rizzo [42]. Subsequently the method has been employed for modeling more general acoustic and elastic wave scattering problems [43]. The combined use of boundary and finite elements has been an efficient way to model solid/fluid interaction problems. However, the boundary element method has difficulties or inefficiencies in handling anisotropy, inhomogeneity, and nonlinear problems.

Objectives of Dissertation

The acoustic microscope is a powerful tool in ultrasonic NDE for characterizing defects. However, the output signal is a combined effect of the system including the transducer/lens assembly, the coupling fluid and its interface with the sample, and the defects. Usually the defect signal is retrieved by a deconvolution process which requires knowledge of the system response. The determination of this response is not a straight-forward process. It is a coupled acoustic/elastodynamic problem involving multiple media and interfaces. A complete numerical model based on the finite element approach is to be developed in this work as it can be seen from the above review that all the analytical and most of other numerical approaches would find difficulty in dealing with such a complex system. The displacement vector is adopted for the solid regions and a scalar pressure or potential variable is used for the fluid region with the satisfaction of appropriate boundary conditions. An explicit difference scheme is performed in the time domain. Various wave propagation and scattering phenomena are implicitly built in to the model.

The model is general and comprehensive in the following aspects. First, it deals with various material geometries such as 2D, axisymmetric, as well as 3D in Cartesian coordinates. Second, it models single and multiple media with full anisotropy and attenuation. Third, wave phenomena at arbitrary solid/fluid interfaces can be predicted. Fourth, various smooth as well as crack-like obstacles can be modeled. In addition, different wave forms such as the fields of point sources, finite aperture transducers, as well as plane waves can be successfully simulated. To meet the requirement of the acoustic microscope, a high frequency must be adopted. This necessarily requires more computer resources and parallel processing is appropriate.

The foundations of dynamic elasticity are presented in Chapter 2 which facilitates the later numerical development. Chapter 3 presents the finite element formulations in the space domain and solution strategies in the time domain. In Chapter 4, the pulsed transducer fields in solids and their interactions with voids and cracks are simulated and compared with other models. The finite element treatment for acoustic media and fluid/solid interfaces is described in Chapter 5 where the visualizations of transient leaky Rayleigh waves are displayed. In Chapter 6, the fields of time-delay spherically focused arrays are numerically analyzed and compared with the impulse response method and good agreement is achieved. Application to acoustic microscopy is the contents of Chapter 8 where the finite element model simulates the spherically focused transducer, the ultrasonic lens based on the solid/fluid model, a focused wave probing a fluid/solid interface and a solid/solid interface with or without surface cracks. Conclusions and comments on possible future work are summarized in Chapter 8.

CHAPTER 2. ACOUSTIC WAVES IN ELASTIC MEDIA

This chapter does not attempt a thorough treatment of the topic as this can be found in standard references [44-46], rather it presents the necessary theoretical background for later numerical development.

Small displacements are assumed so that higher orders can be neglected. This approximation is appropriate for NDE applications. The wavelength is large enough so that the continuum model is valid for the medium. In addition, the medium under consideration is nonpiezoelectric. The derivations in this chapter mainly follow the classic text of Auld.

Deformation and Strain

Unless otherwise specified, the treatment is based on the Cartesian coordinate system. Assume a particle of position $\mathbf{X}$ at a reference time moves to $\mathbf{x}$ at time t. Here the particle means an infinitesimal volume in the continuum model. Then the displacement is defined as

$$\mathbf{u}(\mathbf{X}, t) = \mathbf{x}(\mathbf{X}, t) - \mathbf{X} \tag{2.1}$$

It is obvious that Eq. (2.1) can not fully characterize the deformation since it does not vanish for either rigid translation or rigid rotation. Assuming a neighboring particle is located at $\mathbf{X} + d\mathbf{X}$ and $\mathbf{x} + d\mathbf{x}$ at the reference time and the present time

t respectively, the differential displacement is then

$$d\mathbf{u} = d\mathbf{x}(\mathbf{X}, t) - d\mathbf{X} \tag{2.2}$$

It is seen that (2.2) does reduce to zero for rigid translation. If the displacement vector is written in terms of its Cartesian components, the differential displacement can be represented in terms of the displacement as follows,

$$d\mathbf{u} = \mathbf{e}_i du_i = \mathbf{e}_i u_{i,j} dX_j \tag{2.3}$$

where the indicial notation has been adopted, i.e., repeated indices indicate summation while a comma stands for differentiation. It is noted that $u_{i,j}$ is a second rank tensor. In matrix form it is represented as

$$\varepsilon = \begin{bmatrix} \frac{\partial u_1}{\partial X_1} & \frac{\partial u_1}{\partial X_2} & \frac{\partial u_1}{\partial X_3} \\ \frac{\partial u_2}{\partial X_1} & \frac{\partial u_2}{\partial X_2} & \frac{\partial u_2}{\partial X_3} \\ \frac{\partial u_3}{\partial X_1} & \frac{\partial u_3}{\partial X_2} & \frac{\partial u_3}{\partial X_3} \end{bmatrix} \tag{2.4}$$

The above matrix is known as the displacement gradient matrix. Though the displacement gradient matrix is zero for rigid translation, it does not reduce to zero for rigid rotation. So it is not a true measure of deformation. A usual definition of the deformation is as follows.

$$\Delta = d\mathbf{x} \cdot d\mathbf{x} - d\mathbf{X} \cdot d\mathbf{X} = dx_i dx_i - dX_i dX_i \tag{2.5}$$

which is zero for rigid motion, either translation, rotation or their combination. Since

$$dx_i = dX_i + u_{i,j} dX_j \tag{2.6}$$

Then

$$\begin{aligned}
\Delta &= (dX_i + u_{i,j}dX_j)(dX_i + u_{i,k}dX_k) - dX_i dX_i \\
&= u_{i,k}dX_i dX_k + u_{i,j}dX_i dX_j + u_{i,j}u_{i,k}dX_j dX_k \\
&= (u_{j,k} + u_{k,j} + u_{i,j}u_{i,k})dX_j dX_k \\
&= (u_{i,j} + u_{j,i} + u_{k,i}u_{k,j})dX_i dX_j \\
&= 2S_{ij}dX_i dX_j \qquad (2.7)
\end{aligned}$$

where

$$S_{ij} = \frac{1}{2}(u_{i,j} + u_{j,i} + u_{k,i}u_{k,j}) \qquad (2.8)$$

It should be noted that

$$S_{ij} = S_{ji} \qquad (2.9)$$

S_{ij} is referred to as the strain tensor. It is symmetric as indicated by (2.9). While vanishing for any rigid motion, it is a fundamental variable featuring the deformation of the elastic media. Usually the deformation caused by acoustic waves is very small, i.e., the magnitudes of $u_{i,j}$ are much smaller than unity. So it is reasonable to neglect the quadratic term and keep only the linear terms.

$$S_{ij} = \frac{1}{2}(u_{i,j} + u_{j,i}) \qquad (2.10)$$

It should be remembered that the derivatives in the above formulation are with respect to $\mathbf{X}$. But for the linearization approximation, the derivatives with respect to $\mathbf{X}$ and to $\mathbf{x}$ are the same [Auld], so there is no need to distinguish between them. Therefore

$$S_{ij}(\mathbf{X}, t) = S_{ij}(\mathbf{x}, t) = S_{ij} = \frac{1}{2}(u_{i,j} + u_{j,i}) \qquad (2.11)$$

Comparing with Eq. (2.4) it is seen that the strain tensor is actually the symmetric part of the displacement gradient matrix (also a second rank tensor). In vector notation, the displacement gradient matrix can be written as the gradient of the displacement vector, i.e,

$$\varepsilon = \nabla \mathbf{u} \tag{2.12}$$

and the corresponding strain can be be expressed as

$$S = \nabla_s \mathbf{u} = \frac{1}{2}(\nabla \mathbf{u} + \nabla \mathbf{u}^T) \tag{2.13}$$

Due to the symmetry of S, only six of the nine elements are independent, thus abbreviated subscripts can be adopted. In other words, the double subscripts can be converted into single subscripts according to the following rule: $11 \rightarrow 1$, $22 \rightarrow 2$, $33 \rightarrow 3$, $23/32 \rightarrow 4$, $13/31 \rightarrow 5$, $12/21 \rightarrow 6$. Therefore

$$S = \begin{bmatrix} S_{11} & S_{12} & S_{13} \\ S_{21} & S_{22} & S_{23} \\ S_{31} & S_{32} & S_{33} \end{bmatrix} = \begin{bmatrix} S_1 & \frac{1}{2}S_6 & \frac{1}{2}S_5 \\ \frac{1}{2}S_6 & S_2 & \frac{1}{2}S_4 \\ \frac{1}{2}S_5 & \frac{1}{2}S_4 & S_3 \end{bmatrix} \tag{2.14}$$

In addition, S can be expressed as a vector of six elements, and from Eq. (2.10) we have

$$S = \begin{Bmatrix} S_1 \\ S_2 \\ S_3 \\ S_4 \\ S_5 \\ S_6 \end{Bmatrix} = \begin{Bmatrix} \frac{\partial u_1}{\partial x_1} \\ \frac{\partial u_2}{\partial x_2} \\ \frac{\partial u_3}{\partial x_3} \\ \frac{\partial u_2}{\partial x_3} + \frac{\partial u_3}{\partial x_2} \\ \frac{\partial u_1}{\partial x_3} + \frac{\partial u_3}{\partial x_1} \\ \frac{\partial u_1}{\partial x_2} + \frac{\partial u_2}{\partial x_1} \end{Bmatrix} = \begin{bmatrix} \frac{\partial}{\partial x_1} & 0 & 0 \\ 0 & \frac{\partial}{\partial x_2} & 0 \\ 0 & 0 & \frac{\partial}{\partial x_3} \\ 0 & \frac{\partial}{\partial x_3} & \frac{\partial}{\partial x_2} \\ \frac{\partial}{\partial x_3} & 0 & \frac{\partial}{\partial x_1} \\ \frac{\partial}{\partial x_2} & \frac{\partial}{\partial x_1} & 0 \end{bmatrix} \begin{Bmatrix} u_1 \\ u_2 \\ u_3 \end{Bmatrix} \tag{2.15}$$

In indicial notation Eq.(2.15) is written as

$$S_I = \nabla_{Ii} u_i \tag{2.16}$$

where

$$[\nabla_{Ii}]^T = \begin{bmatrix} \frac{\partial}{\partial x_1} & 0 & 0 & 0 & \frac{\partial}{\partial x_3} & \frac{\partial}{\partial x_2} \\ 0 & \frac{\partial}{\partial x_2} & 0 & \frac{\partial}{\partial x_3} & 0 & \frac{\partial}{\partial x_1} \\ 0 & 0 & \frac{\partial}{\partial x_3} & \frac{\partial}{\partial x_2} & \frac{\partial}{\partial x_1} & 0 \end{bmatrix} \tag{2.17}$$

and $I = 1,2,3,4,5,6, i = 1,2,3$.

For cylindrical coordinates Eq. (2.16) is still applicable with the following corresponding definitions.

$$[\nabla_{Ii}]^T = \begin{bmatrix} \frac{\partial}{\partial r} & \frac{1}{r} & 0 & 0 & \frac{\partial}{\partial z} & \frac{1}{r}\frac{\partial}{\partial \phi} \\ 0 & \frac{1}{r}\frac{\partial}{\partial \phi} & 0 & \frac{\partial}{\partial z} & 0 & \frac{\partial}{\partial r} - \frac{1}{r} \\ 0 & 0 & \frac{\partial}{\partial z} & \frac{1}{r}\frac{\partial}{\partial \phi} & \frac{\partial}{\partial r} & 0 \end{bmatrix} \tag{2.18}$$

where $i = 1,2,3$ or r, ϕ, z, and $I = 1,2,3,4,5,6$.

Traction Force and Stress

In a vibrating solid medium, there may exist two types of forces. One is the body force and the other is the traction force. The body force is a long range force and acts on the interior particles of the medium. If the force acting on the volume ΔV around point P is $\Delta \mathbf{F}$, then the body force (the i^{th} component) per unit volume at P is

$$f_i = \lim_{\Delta V \to 0} \frac{\Delta F_i}{\Delta V} \tag{2.19}$$

The traction force is generated by the application of an excitation on the surface of a solid medium. It is transmitted through the medium by the interactions between

the neighboring particles. Unlike a body force which acts on the volumes in the medium, the traction force acts on surfaces of the medium. Assume the traction force acting on a surface ΔS around point P is $\Delta \mathbf{T}$, then the stress of the traction force is

$$T_i = \lim_{\Delta S \to 0} \frac{\Delta T_i}{\Delta S} \tag{2.20}$$

It is noted that the traction component T_i defined above is also dependent on the orientation of ΔS. In order to characterize the stress at some point, an orthogonal differential volume is taken and three force components are specified on each face of the volume. Then the traction forces on the three faces are respectively

$$\mathbf{T}_1 = \mathbf{e}_1 T_{11} + \mathbf{e}_2 T_{21} + \mathbf{e}_3 T_{31} \tag{2.21a}$$

$$\mathbf{T}_2 = \mathbf{e}_1 T_{12} + \mathbf{e}_2 T_{22} + \mathbf{e}_3 T_{32} \tag{2.21b}$$

$$\mathbf{T}_3 = \mathbf{e}_1 T_{13} + \mathbf{e}_2 T_{23} + \mathbf{e}_3 T_{33} \tag{2.21c}$$

In indicial notation

$$\mathbf{T}_j = \mathbf{e}_i T_{ij} \tag{2.22}$$

where $\mathbf{T}_j$ is the traction force per unit area on the j^{th} face of the volume and T_{ij} are called stress components or the stress tensor which stands for the i^{th} component of the traction force acting on the j^{th} face of the infinitesimal volume.

The traction force or stress vector acting on a surface of arbitrary orientation $\mathbf{n} = \mathbf{e}_i n_i$ can be determined from the balance of forces as follows.

$$\begin{Bmatrix} T_1^n \\ T_2^n \\ T_3^n \end{Bmatrix} = \begin{bmatrix} T_{11} & T_{12} & T_{13} \\ T_{21} & T_{22} & T_{23} \\ T_{31} & T_{32} & T_{33} \end{bmatrix} \begin{Bmatrix} n_1 \\ n_2 \\ n_3 \end{Bmatrix} \tag{2.23}$$

or in indicial notation

$$T_i^n = T_{ij} n_j \tag{2.24}$$

In the absence of body moment, it can be shown that

$$T_{ij} = T_{ji} \tag{2.25}$$

Dynamic Equation of Motion

For an arbitrary volume V and surface S of a medium with density ρ, it follows from Newton's law that

$$\oint_S T_{ij} n_j dS + \int_V f_i dV = \int_V \rho \ddot{u}_i dV \tag{2.26}$$

The divergence theorem states that

$$\oint_S T_{ij} n_j dS = \int_V T_{ij,j} dV \tag{2.27}$$

Then

$$\int_V T_{ij,j} dV + \int_V f_i dV = \int_V \rho \ddot{u}_i dV \tag{2.28}$$

or

$$\int_V (T_{ij,j} + f_i - \rho \ddot{u}_i) dV = 0 \tag{2.29}$$

Due to the arbitrariness of V, we have

$$T_{ij,j} + f_i = \rho \ddot{u}_i \tag{2.30}$$

where $i, j = 1, 2, 3$. In vector and matrix form

$$\nabla \cdot \mathbf{T} + \mathbf{f} = \rho \ddot{\mathbf{u}} \tag{2.31}$$

where

$$\nabla \cdot \mathbf{T} = \mathbf{e_i T_{ij,j}} \tag{2.32}$$

Analogous to the strain fields, the stress tensor can also be represented using the abbreviated subscripts because of their symmetry property.

$$\mathbf{T} = \begin{bmatrix} T_{11} & T_{12} & T_{13} \\ T_{21} & T_{22} & T_{23} \\ T_{31} & T_{32} & T_{33} \end{bmatrix} = \begin{bmatrix} T_1 & T_6 & T_5 \\ T_6 & T_2 & T_4 \\ T_5 & T_4 & T_3 \end{bmatrix} \tag{2.33}$$

In vector notation T can be simply written as

$$\mathbf{T} = \begin{bmatrix} T_1 & T_2 & T_3 & T_4 & T_5 & T_6 \end{bmatrix}^{\mathbf{T}} \tag{2.34}$$

Then the gradient of the stress tensor in Eq. (2.31) can be written in a vector form as

$$\nabla \cdot \mathbf{T} = \begin{bmatrix} \frac{\partial}{\partial x_1} & 0 & 0 & 0 & \frac{\partial}{\partial x_3} & \frac{\partial}{\partial x_2} \\ 0 & \frac{\partial}{\partial x_2} & 0 & \frac{\partial}{\partial x_3} & 0 & \frac{\partial}{\partial x_1} \\ 0 & 0 & \frac{\partial}{\partial x_3} & \frac{\partial}{\partial x_2} & \frac{\partial}{\partial x_1} & 0 \end{bmatrix} \begin{Bmatrix} T_1 \\ T_2 \\ T_3 \\ T_4 \\ T_5 \\ T_6 \end{Bmatrix} = \nabla_{\mathbf{iI}} \mathbf{T_I} \tag{2.35}$$

In terms of the abbreviated subscript notation for the stress, the equation of motion in Eq. (2.31) is represented as

$$\nabla_{iI} T_I + f_i = \rho \ddot{u}_i \tag{2.36}$$

where $i = 1, 2, 3$ or x, y, z, and $I = 1, 2, 3, 4, 5, 6$.

Stress-Strain Relationship

Hooke's law for a one dimensional isotropic medium states that the stress and strain are linearly related to each other, i.e.,

$$T = ES \tag{2.37}$$

where E is Young's modulus. For general multidimensional materials Hooke's law still holds as long as the stress and strain are small enough. Assume there is no residual stress at zero strain, T can be expressed in terms of S in the following series form,

$$T_{ij} = c_{ijkl}S_{kl} + \frac{1}{2}c_{ijklmn}S_{kl}S_{mn} + \cdots \tag{2.38}$$

By neglecting the terms of the second or higher order, it follows that

$$T_{ij} = c_{ijkl}S_{kl} \tag{2.39}$$

where c_{ijkl} are known as the elastic constants. Due to the following symmetry relations for the elastic constants

$$c_{ijkl} = c_{jikl} = c_{ijlk} = c_{klij} \tag{2.40}$$

only 21 of the 81 components are independent. This is the most general case. For many kinds of media, there are less than this number of independent constants due to special structural symmetries. For an isotropic medium, which is a special case, there exist only two independent elastic constants expressed as follows,

$$c_{ijkl} = \lambda\delta_{ij}\delta_{kl} + \mu(\delta_{ik}\delta_{jl} + \delta_{il}\delta_{jk}) \tag{2.41}$$

where λ and μ are known as Lame's constants. The corresponding stress-strain relationship becomes

$$T_{ij} = \lambda S_{kk}\delta_{ij} + 2\mu S_{ij} \tag{2.42}$$

or equivalently

$$S_{ij} = \frac{\lambda\delta_{ij}}{3\mu(3\lambda+2\mu)}T_{kk} + \frac{1}{2\mu}T_{ij} \tag{2.43}$$

In compatibility with the stress and strain, the elastic constants are also normally represented in terms of abbreviated subscripts. Under the following rule,

$$I = \begin{cases} i, & i = j \\ 9-i-j, & i \neq j \end{cases} \tag{2.44a}$$

$$J = \begin{cases} k, & k = l \\ 9-k-l, & k \neq l \end{cases} \tag{2.44b}$$

we have

$$C_{IJ} = c_{ijkl} \tag{2.45}$$

and the generalized Hooke's law is rewritten as follows,

$$T_I = C_{IJ}S_J \tag{2.46}$$

Substituting Eq. (2.46) into Eq. (2.16) and then Eq.(2.16) into Eq. (2.36) results in the following equation of motion in terms of displacements,

$$\nabla_{iI}C_{IJ}\nabla_{Jj}u_j - f_i = \rho\ddot{u}_i \tag{2.47}$$

where $i,j = 1,2,3$ and $I,J = 1,2,3,4,5,6$.

For an isotropic medium, Eq. (2.45) reduces to

$$[C_{IJ}] = \begin{bmatrix} \lambda+2\mu & \lambda & \lambda & 0 & 0 & 0 \\ \lambda & \lambda+2\mu & \lambda & 0 & 0 & 0 \\ \lambda & \lambda & \lambda+2\mu & 0 & 0 & 0 \\ 0 & 0 & 0 & \mu & 0 & 0 \\ 0 & 0 & 0 & 0 & \mu & 0 \\ 0 & 0 & 0 & 0 & 0 & \mu \end{bmatrix} \tag{2.48}$$

Substitution of Eq. (2.48) into Eq. (2.47) and a little algebraic manipulation yields

$$(\lambda + \mu)u_{j,ji} + \mu u_{i,jj} + f_i = \rho \ddot{u}_i \qquad (2.49)$$

which, in vector form, is

$$(\lambda + \mu)\nabla\nabla \cdot \mathbf{u} + \mu\nabla^2\mathbf{u} + \mathbf{f} = \rho\ddot{\mathbf{u}} \qquad (2.50)$$

or

$$(\lambda + 2\mu)\nabla\nabla \cdot \mathbf{u} - \mu\nabla \times \nabla \times \mathbf{u} + \mathbf{f} = \rho\ddot{\mathbf{u}} \qquad (2.51)$$

by noticing the following vector identity

$$\nabla \times \nabla \times \mathbf{u} = \nabla\nabla \cdot \mathbf{u} - \nabla^2\mathbf{u} \qquad (2.52)$$

Eqs. (2.49-2.51) are the common forms of governing equations for waves in isotropic media.

Major Wave Types in Isotropic Media

In a fluid medium, only the longitudinal or compressional wave is supported. Whereas in a solid medium, a variety of waves can be supported depending on the structure and boundary conditions. In order to facilitate later discussions, a survey of the wave types is presented here.

Bulk waves

In an unbounded medium, there exist possibly two kinds of waves, the longitudinal (L) or compressional wave and the shear (S) or transverse waves. In fact, the total displacement can be taken as the combination of two components, i.e.,

$$\mathbf{u} = \mathbf{u}_l + \mathbf{u}_s \qquad (2.53)$$

where

$$\mathbf{u}_l = \nabla\phi, \quad \mathbf{u}_s = \nabla \times \psi, \quad \nabla \cdot \psi = 0 \tag{2.54}$$

By substituting of Eq. (2.53) with (2.54) in Eq.(2.51) and noting that

$$\nabla \times \nabla\phi = 0, \quad \nabla \cdot \nabla \times \psi = 0 \tag{2.55}$$

we have

$$\nabla((\lambda + \mu)\nabla^2\phi - \rho\ddot{\phi}) + \nabla \times (\mu\nabla^2\psi - \rho\ddot{\psi}) = 0 \tag{2.56}$$

No body force has been assumed. Taking the curl and divergence of the above formula respectively, we obtain

$$\nabla^2\phi = \frac{1}{c_l^2}\ddot{\phi}, \quad \nabla^2\psi = \frac{1}{c_s^2}\ddot{\psi} \tag{2.57}$$

where

$$c_l^2 = \frac{\lambda + 2\mu}{\rho}, \quad c_s^2 = \frac{\mu}{\rho} \tag{2.58}$$

It is seen that the L and S waves satisfy the standard wave equations and propagate with velocities c_l and c_s, respectively. The L wave propagates in the same direction as the particle oscillates while the propagating direction of the S wave is perpendicular to that of the oscillating particle. Depending on the specific form of excitations, there may exist plane, cylindrical or spherical waves as well as their superposition. Subject to a discontinuity, wave phenomena such as reflection, refraction, diffraction and mode conversion may occur. Under these conditions, it is helpful to decompose the S wave into the SH and SV components with the former referring to the component parallel to the discontinuity and the latter parallel to the plane perpendicular to the discontinuity.

Surface and plate waves

Wave propagation in a bounded or semi-bounded medium is more common in practice. The wave-boundary interaction needs to satisfy the underlying boundary conditions. At a free surface, both the normal and tangential stresses vanish whereas on a rigid boundary the displacements are constrained to zero values. The interface between two solids in perfect contact requires continuity for both the stress and displacement. However, a slippery contact between two solids requires the continuity of the normal stress and displacement components and does not support the tangential stress. Similarly for the solid/fluid interface, the normal stress or pressure and the normal displacement are continuous and tangential stress vanishes.

Rayleigh surface waves. Consider an elastic solid with a free surface. Besides the L and S waves which propagate in the interior of the media, there could exist a third kind of waveform called the Rayleigh surface wave whose propagation is largely confined at the surface and decays dramatically from the surface deeper into the interior. It can be shown [44] that the Rayleigh wave velocity c_R is determined from the following equation

$$\left(\frac{c_R}{c_S}\right)^6 - 8\left(\frac{c_R}{c_S}\right)^4 + 8\left[3 - 2\left(\frac{c_S}{c_l}\right)^2\right]\left(\frac{c_R}{c_S}\right)^2 - 16\left[1 - \left(\frac{c_S}{c_l}\right)^2\right] = 0 \qquad (2.59)$$

This is a cubic equation for $\left(\frac{c_R}{c_S}\right)^2$, and there should be three associated roots. However, there is only one acceptable root which is real and positive. An approximate solution is given by [3] as

$$c_R = c_S(1.14418 - 0.25771\nu + 0.12661\nu^2)^{-1} \qquad (2.60)$$

where ν is the Poisson ratio.

For a sinusoidal excitation, the particle movement associated with the Rayleigh wave follows an elliptical path while the elliptical shape changes from the surface to the interior. Of the two displacement components, the one normal to the surface , i.e., the shear component, dominates. The Rayleigh wave decays much less during propagation than that of the bulk L and S waves since the propagation dimension is reduced by one, and is therefore the dominant wave type in seismology. The Rayleigh wave plays a major role in surface acoustic devices and finds applications in NDE for surface and subsurface defect detection and characterization.

Generalized Rayleigh and Stoneley waves. A propagating wave can also exist on the interface of two different media. The wave propagating along the fluid/solid interface is known as the generalized Rayleigh wave and its velocity c'_R is given in the following equation [47]

$$\left[2-\left(\frac{c'_R}{c_s}\right)^2\right]^2 - 4\left[1-\left(\frac{c'_R}{c_s}\right)^2\right]^{\frac{1}{2}}\left[1-\left(\frac{c'_R}{c_l}\right)^2\right]^{\frac{1}{2}} = -\frac{\rho_f}{\rho}\left(\frac{c'_R}{c_s}\right)^4\left[\frac{1-(c'_R/c_l)^2}{1-(c'_R/c_f)^2}\right]^{\frac{1}{2}} \tag{2.61}$$

There is only one positive root for c'_R which is slightly larger than c_R for the same solid medium. If $\rho_f = 0$, Eq. (2.61) reduces to Eq. (2.59) and c'_R reduces to c_R. It should be pointed out that the Rayleigh wave at the fluid/solid interface is a leaky wave, i.e., it continuously radiates energy into the fluid medium with the decrease of its magnitude. The wave propagating along the solid/solid interface is known as the Stoneley wave. Realistic Stoneley wave velocities can be obtained for only a certain range of the density ratio and shear modulus ratio of the two media. Similar to the

Rayleigh wave, the Stoneley wave is also nondispersive which means that it's velocity is independent of frequency for linear, homogeneous and isotropic media.

Lamb and Love waves. The lamb wave is a coupled L and SV wave propagating in a thin plate of wide extension with both surfaces traction free. For simplicity consider the plane strain case where the plate is parallel to the xy plane and the two surfaces are located at $z = \pm h$. The propagation of the Lamb wave is along the x direction and there is no displacement in the y direction. Assume that the wave number associated with the Lamb wave is ξ, the corresponding L and SV wave numbers in the normal direction are

$$\alpha = \sqrt{\left(\frac{\omega}{c_l}\right)^2 - \xi^2}, \quad \beta = \sqrt{\left(\frac{\omega}{c_s}\right)^2 - \xi^2} \tag{2.62}$$

The characterization equation associated with the given boundary conditions leads to the following decoupled Rayleigh-Lamb frequency equations

$$\frac{\tan\beta h}{\tan\alpha h} = -\frac{4\alpha\beta\xi^2}{(\xi^2 - \beta^2)^2}, \quad \frac{\tan\beta h}{\tan\alpha h} = -\frac{(\xi^2 - \beta^2)^2}{4\alpha\beta\xi^2} \tag{2.63}$$

which correspond to the symmetric and antisymmetric modes respectively. Symmetry or antisymmetry refers to the displacement vector with respect to the mid-plane of the plate. Unlike the Rayleigh wave which is nondispersive, the Lamb wave is dispersive in that its phase velocity $c_L = \frac{\omega}{\xi}$ determined from the Rayleigh-Lamb equations is a function of frequency ω. The Love wave propagates in the SH mode along a layered medium on the surface of a solid half-space. It is of major interest in seismology but also finds application in surface acoustic devices. Detailed analysis of Lamb waves is available in the literature.

CHAPTER 3. FINITE ELEMENT MODELING

The boundary value problem for a solid geometry is formulated by the governing equations of elastodynamics with the underlying boundary conditions. Semi-discretized finite element equations in the space domain are derived on the basis of the principle of variations. Direct time integration is carried out through the explicit central difference scheme. Absorbing boundary conditions are implemented for modeling infinite media. Two-dimensional and axisymmetric geometries are considered as special examples of 3D in Cartesian or cylindrical coordinates.

Semi-discretized Finite Element Formulation

Governing equations

To simulate a general ultrasonic testing problem, we consider an elastic medium of volume V and boundary S. The governing equations and relevant boundary conditions comprise the boundary value problem. It is shown in the last chapter that the general equation of motion is

$$T_{ij,j} + f_i = \rho \ddot{u}_i \tag{3.1}$$

or, in the abbreviated notation

$$\nabla_{iI} T_I + f_i = \rho \ddot{u}_i \tag{3.2}$$

In order to be able to model the viscous damping effect, the generalized Hooke's law is modified in the following form

$$T_{ij} = c_{ijkl}S_{kl} + \eta_{ijkl}\dot{S}_{kl} \tag{3.3}$$

in the standard index form, or

$$T_I = C_{IJ}S_J + H_{IJ}\dot{S}_J \tag{3.4}$$

in the abbreviated index form.

Analogous to the derivation of Eq. (2.47), the corresponding governing displacement equation, neglecting body force, is

$$c_{ijkl}u_{k,lj} + \eta_{ijkl}\dot{u}_{k,lj} = \rho\ddot{u}_i \tag{3.5}$$

in the standard index notation, or

$$\nabla_{iI}C_{IJ}\nabla_{Jj}u_j - f_i\nabla_{iI}H_{IJ}\nabla_{Jj}\dot{u}_j - f_i = \rho\ddot{u}_i \tag{3.6}$$

in the abbreviated indicial notation.

For the bounded medium, the boundary condition might be either of Dirichlet type or Neumann type with the former referring to the specification of the displacement and the latter referring to the specification of the traction force. For generality, the boundary is assumed to contain both types of conditions, i.e.,

$$u_i = u_i^S \quad \text{on } S_u \tag{3.7}$$

$$t_i = T_{ij}n_j = t_i^S \quad \text{on } S_t \tag{3.8}$$

where

$$S_u \cup S_t = S, \quad S_u \cap S_t = 0 \tag{3.9}$$

Zero values for Eqs. (3.7) and (3.8) correspond to the rigid and traction free boundaries, respectively. It can be shown that the above described boundary conditions lead to unique solutions. In addition, mixed boundary conditions of the two types over either the whole or part of the boundary also yield unique solutions [44].

Solutions of the governing hyperbolic equations also require the following initial conditions for the displacements,

$$u_i|_{t=0} = u_i^0, \quad \dot{u}_i|_{t=0} = v_i^0 \tag{3.10}$$

in domain V.

Variational formulation

The above boundary value problem can be solved numerically through the weighted residual approach. It can be shown by variational calculus that the solution corresponds to the minimization of a scalar functional which is related to the total energy of the system. An appropriate energy functional [48] can be defined as

$$F(\mathbf{u},t) = P(\mathbf{u},t) + K(\mathbf{u},t) + W_d(\mathbf{u},t) - W_e(\mathbf{u},t) \tag{3.11}$$

where

$$P(\mathbf{u},t) = \frac{1}{2}\int_V S_{ji}c_{ijkl}S_{kl}dV = \frac{1}{2}\int_V S_I C_{IJ} S_J dV \tag{3.12a}$$

$$K(\mathbf{u},t) = \frac{1}{2}\int_V \rho\dot{u}_i\dot{u}_i dV = \int_V \rho\ddot{u}_i u_i dV \tag{3.12b}$$

$$W_d(\mathbf{u},t) = \int_V \dot{S}_{ji}\eta_{ijkl}S_{kl}dV = \int_V \dot{S}_I H_{IJ} S_J dV \tag{3.12c}$$

$$W_e(\mathbf{u},t) = \int_{S_t} t_i u_i ds \tag{3.12d}$$

In the above equations, P is the potential or strain energy, K is the kinetic energy, W_d represents the energy lost through viscous damping, and W_e is the work

done by the boundary traction force under the assumption of zero body force. Upon substituting Eq. (3.12) into Eq. (3.11), we have

$$F(\mathbf{u},t) = \frac{1}{2}\int_V C_{IJ}S_I S_J dV + \int_V H_{IJ}\dot{S}_I S_J dV + \int_V u_i \rho \ddot{u}_i dv - \int_{S_t} u_i t_i ds \quad (3.13)$$

The variation of the energy functional δF due to the variation of displacement δu and therefore δS is

$$\delta F = \int_V \delta S_I C_{IJ} S_J dV + \int_V \delta S_I H_{IJ} \dot{S}_J dV + \int_V \delta u_i \rho \ddot{u}_i dV - \int_S \delta u_i t_i dS \quad (3.14)$$

The first term on the right hand side is derived as follows by noticing the symmetry property of C.

$$\begin{aligned} \frac{1}{2}\delta(S_I C_{IJ} S_J) &= \frac{1}{2}(\delta S_I C_{IJ} S_J + S_I C_{IJ}\delta S_J) \\ &= \frac{1}{2}(\delta S_I C_{IJ} S_J + S_J C_{JI}\delta S_I) \\ &= \frac{1}{2}(\delta S_I C_{IJ} S_J + S_J C_{IJ}\delta S_I) \\ &= \delta S_I C_{IJ} S_J \end{aligned} \quad (3.15)$$

It follows from Eq. (2.16) that

$$S_I = \nabla_{Ii} u_i, \quad \delta S_I = \nabla_{Ii}\delta u_i \quad (3.16)$$

Setting Eq. (3.16) into (3.14) gives

$$\begin{aligned} \delta F &= \int_V \nabla_{Ii}\delta u_i C_{IJ} \nabla_{Jj} u_j dV + \int_V \nabla_{Ii}\delta u_i H_{IJ}\nabla_{Jj}\dot{u}_j dV \\ &\quad + \int_V \delta u_i \rho \ddot{u}_i dV - \int_S \delta u_i t_i dS \end{aligned} \quad (3.17)$$

Finite element approximation

The domain V is discretized into subdomains called elements, denoted by V^e, and the intersection points of neighboring elements are known as nodes. The dis-

placements in each element u are expressed in terms of the unknown nodal values U through the interpolation or shape functions N, i.e.,

$$u_i(\mathbf{x};t) = N^m(\mathbf{x})U_i^m(t) \tag{3.18}$$

where the repeated superscripts m sum over the number of nodes per element N_e. Upon discretization, the overall energy functional and its variation can be taken as the superposition from each element, i.e.,

$$F = \sum_e F^e, \quad \delta F = \sum_e \delta F^e \tag{3.19}$$

and it follows from Eq. (3.17)

$$\begin{aligned} \delta F^e &= \int_{V^e} \nabla_{Ii}\delta u_i C_{IJ} \nabla_{Jj} u_j dV + \int_{V^e} \nabla_{Ii}\delta u_i H_{IJ} \nabla_{Jj} \dot{u}_j dV \\ &\quad + \int_{V^e} \delta u_i \rho \ddot{u}_i dV - \int_{S^e} \delta u_i t_i dS \end{aligned} \tag{3.20}$$

Substituting Eq. (3.18) into (3.20) and having $\delta F^e = 0$ for stationarity yields

$$\delta U_{im}^e (M_{ij}^{mn} \ddot{U}_{nj}^e + D_{ij}^{mn} \dot{U}_{nj} + K_{ij}^{mn} U_{nj} - R_{im}) = 0 \tag{3.21}$$

where

$$\begin{aligned} M_{ij}^{mn} &= \int_{V^e} \rho N^m N^n \delta_{ij} dV \\ D_{ij}^{mn} &= \int_{V^e} \nabla_{Ii} N^m H_{IJ} \nabla_{Jj} N^n dV \\ K_{ij}^{mn} &= \int_{V^e} \nabla_{Ii} N^m C_{IJ} \nabla_{Jj} N^n dV \\ R_{im} &= \int_{S_t^e} N^m t_i dS \end{aligned} \tag{3.22a}$$

The nodal displacements for each element can be rewritten in the form of a column vector

$$\begin{aligned} \{U^e\}^T &= \left[\begin{array}{ccccccccc} U_x^1 & U_y^1 & U_z^1 & U_x^2 & U_y^2 & U_z^2 & \cdots & U_x^{Ne} & U_y^{Ne} & U_z^{Ne} \end{array} \right] \\ &= \left[\begin{array}{ccccccc} U_1^e & U_2^e & U_3^e & U_4^e & U_5^e & \cdots & U_{N_d Ne-1}^e & U_{N_d Ne}^e \end{array} \right] \end{aligned} \tag{3.23}$$

Correspondingly

$$\begin{aligned}\{R^e\}^T &= \left[\begin{array}{cccccccccc} R_x^1 & R_y^1 & R_z^1 & R_x^2 & R_y^2 & R_z^2 & \cdots & R_x^{Ne} & R_y^{Ne} & R_z^{Ne} \end{array}\right] \\ &= \left[\begin{array}{ccccccc} R_1^e & R_2^e & R_3^e & R_4^e & R_5^e & \cdots & R_{N_dNe-1}^e \quad R_{N_dNe}^e \end{array}\right] \end{aligned} \tag{3.24}$$

and

$$[M^e] = \left[\begin{array}{ccc} M_{xx}^{mn} & 0 & 0 \\ 0 & M_{yy}^{mn} & 0 \\ 0 & 0 & M_{zz}^{mn} \end{array}\right] = \left[\begin{array}{ccc} M_{11}^e & \cdots & M_{1N_p}^e \\ \vdots & \ddots & \vdots \\ M_{N_p1}^e & \cdots & M_{N_pN_p}^e \end{array}\right] \tag{3.25}$$

$$[D^e] = \left[\begin{array}{ccc} D_{xx}^{mn} & D_{xy}^{mn} & D_{xz}^{mn} \\ D_{yx}^{mn} & D_{yy}^{mn} & D_{yz}^{mn} \\ D_{zx}^{mn} & D_{zy}^{mn} & D_{zz}^{mn} \end{array}\right] = \left[\begin{array}{ccc} D_{11}^e & \cdots & D_{1N_p}^e \\ \vdots & \ddots & \vdots \\ D_{N_p1}^e & \cdots & D_{N_pN_p}^e \end{array}\right] \tag{3.26}$$

$$[K^e] = \left[\begin{array}{ccc} K_{xx}^{mn} & K_{xy}^{mn} & K_{xz}^{mn} \\ K_{yx}^{mn} & K_{yy}^{mn} & K_{yz}^{mn} \\ K_{zx}^{mn} & K_{zy}^{mn} & K_{zz}^{mn} \end{array}\right] = \left[\begin{array}{ccc} K_{11}^e & \cdots & K_{1N_p}^e \\ \vdots & \ddots & \vdots \\ K_{N_p1}^e & \cdots & K_{N_pN_p}^e \end{array}\right] \tag{3.27}$$

where $N_p = N_d N_e$. Eq. (3.21) can then be rewritten as

$$\{\delta U^e\}^T (M^e \ddot{U}^e + D^e \dot{U}^e + K^e U^e - R^e) = 0 \tag{3.28}$$

Due to the arbitrariness of variations δU^e, we obtain

$$M^e \ddot{U}^e + D^e \dot{U}^e + K^e U^e = R^e \tag{3.29}$$

where M^e, D^e and K^e are the elemental mass, damping and stiffness matrices, respectively. All the matrices can be seen to be symmetric. M^e is positive definite

while D^e and K^e are positive semi-definite. R^e is a vector carrying the traction boundary conditions for element e along a traction boundary. The assembly of all the elemental matrix equations leads to the following global matrix equation

$$M\ddot{U}_t + D\dot{U}_t + KU_t = R_t \tag{3.30}$$

where U_t is the displacement vector containing all the components at all the nodal points in the problem domain. M, D, K and R_t are the global mass, damping, stiffness matrices and traction force vector, respectively. The formulation leading to Eq. (3.30) is general in that full anisotropy, viscous damping, inhomogeneity and multi-media are built into the model through the material parameters. The finite element equations are to be solved in the time domain.

Two-Dimensional and Axisymmetric Approximations

The finite element formulations in the last section are valid for general three dimensional geometries in either Cartesian or cylindrical coordinates which are most common in NDE applications. However, the implementations are restricted to rather simple and small geometries due to the limited computer resources. 2D and axisymmetry are suitable approximations for a range of practical problems with the attractive feature of the reduction of dimensions by one. This section summarizes the elemental matrix forms for the two types of approximations

Two-dimensional approximation

A two-dimensional or plane problem results when the quantities under consideration are independent of one of the directions in Cartesian coordinates. Without

losing generality, assume the direction is along the z axis. There exist two types of plane problems, i.e., plane strain and plane stress. Plane strain assumes that all the nonzero strains and displacements are in the xy plane, i.e., no component exists in the z direction. This condition applies when the dimension of the geometry in the z direction is large with respect to the x and y directions. On the other hand, plane stress assumes that the normal stress along the z direction is zero and this condition applies when the dimension of the geometry is small in the z direction with respect to the x and y directions. Only plane strain is presented here due to its better approximation in NDE applications. Under this condition, we have

$$u_x = u_x(x,y), \quad u_y = u_y(x,y), \quad u_z = 0 \tag{3.31}$$

and the equation of motion is reduced to the following form

$$\nabla \cdot T = \rho \ddot{\mathbf{u}} \tag{3.32}$$

where

$$\nabla\cdot = \begin{bmatrix} \frac{\partial}{\partial x} & 0 & \frac{\partial}{\partial y} \\ 0 & \frac{\partial}{\partial y} & \frac{\partial}{\partial x} \end{bmatrix} \tag{3.33}$$

The stress tensor is expressed in the abbreviated notation

$$T = \begin{bmatrix} T_{xx} & T_{yy} & T_{xy} \end{bmatrix}^T = CS + H\dot{S} \tag{3.34}$$

where

$$C = \begin{bmatrix} C_{11} & C_{12} & C_{16} \\ C_{12} & C_{22} & C_{26} \\ C_{16} & C_{26} & C_{66} \end{bmatrix}, \quad H = \begin{bmatrix} H_{11} & H_{12} & H_{16} \\ H_{12} & H_{22} & H_{26} \\ H_{16} & H_{26} & H_{66} \end{bmatrix} \tag{3.35}$$

For an isotropic medium, the C and H matrices are reduced to

$$C = \begin{bmatrix} \lambda+2\mu & \lambda & 0 \\ \lambda & \lambda+2\mu & 0 \\ 0 & 0 & \mu \end{bmatrix} \quad H = \begin{bmatrix} H_{11} & H_{12} & 0 \\ H_{12} & H_{11} & 0 \\ 0 & 0 & H_{66} \end{bmatrix} \tag{3.36}$$

where $H_{66} = (H_{11} - H_{12})/2$. The normal stress component T_{zz} can is related to T_{xx} and T_{yy} through the Poisson ratio ν

$$T_{zz} = -\nu(T_{xx} + T_{yy}) \tag{3.37}$$

The strain tensor is in the following form

$$S = \begin{bmatrix} S_{xx} & S_{yy} & 2S_{xy} \end{bmatrix}^T = A\mathbf{u} \tag{3.38}$$

where

$$A = \begin{bmatrix} \frac{\partial}{\partial x} & 0 & \frac{\partial}{\partial y} \\ 0 & \frac{\partial}{\partial y} & \frac{\partial}{\partial x} \end{bmatrix}^T, \quad \mathbf{u} = \begin{Bmatrix} u_x \\ u_y \end{Bmatrix} \tag{3.39}$$

Upon discretization, the interpolation in an element is written as

$$\mathbf{u} = NU \tag{3.40}$$

and therefore

$$S = A\mathbf{u} = ANU = BU \tag{3.41}$$

The elemental matrices can be derived in the same procedure as in the last section

$$M^e = \int\int \rho N^T N dxdy \tag{3.42a}$$

$$K^e = \int\int B^T C B dxdy \tag{3.42b}$$

$$D^e = \int\int B^T \eta B dxdy \tag{3.42c}$$

$$R^e = \int_{S_t^e} N^T \underline{t} ds \tag{3.42d}$$

where

$$B = AN \tag{3.43}$$

$$N = \begin{bmatrix} N_1 & 0 & N_2 & 0 & \cdots & N_{Ne} & 0 \\ 0 & N_1 & 0 & N_2 & \cdots & 0 & N_{Ne} \end{bmatrix} \tag{3.44}$$

$$U = \begin{bmatrix} U_x^1 & U_y^1 & U_x^2 & U_y^2 & \cdots & U_x^{Ne} & U_y^{Ne} \end{bmatrix}^T \tag{3.45}$$

For a general four-node quadrilateral isoparametric element, $N_e = 4$, and the shape functions in the natural (ξ, η) coordinates can be derived based on the bilinear interpolation

$$\begin{aligned} N_1 &= \frac{1}{4}(1-\xi)(1-\eta) \quad N_2 = \frac{1}{4}(1+\xi)(1-\eta) \\ N_3 &= \frac{1}{4}(1+\xi)(1+\eta) \quad N_4 = \frac{1}{4}(1-\xi)(1+\eta) \end{aligned} \tag{3.46}$$

and for an eight-node quadrilateral isoparametric element, $N_e = 8$, the shape functions are

$$\begin{aligned} N_1 &= \frac{1}{4}(1-\xi)(1-\eta)(-1-\xi-\eta) \quad N_5 = \frac{1}{2}(1-\xi^2)(1-\eta) \\ N_2 &= \frac{1}{4}(1+\xi)(1-\eta)(-1+\xi-\eta) \quad N_6 = \frac{1}{2}(1+\xi)(1-\eta^2) \\ N_3 &= \frac{1}{4}(1+\xi)(1+\eta)(-1+\xi+\eta) \quad N_7 = \frac{1}{2}(1-\xi^2)(1+\eta) \\ N_4 &= \frac{1}{4}(1-\xi)(1+\eta)(-1-\xi+\eta) \quad N_8 = \frac{1}{2}(1-\xi)(1-\eta^2) \end{aligned} \tag{3.47}$$

The coordinate transformations satisfy the following relationship

$$x_i = \sum_{i=1}^{Ne} N_i \xi_i, \quad y_i = \sum_{i=1}^{Ne} N_i \eta_i \tag{3.48}$$

which is similar to the unknown variable transformation. The evaluations of the matrices are usually performed in natural coordinates through Gaussian quadrature.

Axisymmetric approximation

Axisymmetry assumes that both the geometry and boundary conditions (including driving forces) are symmetric with respect to the z axis and no variations exist along the θ direction. Under this condition, $S_{r\theta}$, $S_{\theta z}$,$T_{r\theta}$ and $T_{\theta z}$ all vanish and

$$u_r = u_r(r,z), \quad u_z = u_z(r,z), \quad u_\theta = 0 \tag{3.49}$$

The equation of motion can also be written in the form of Eq. (3.32) with the following definition for the operator

$$\nabla\cdot = \begin{bmatrix} (\frac{\partial}{\partial r}+\frac{1}{r}) & 0 & \frac{\partial}{\partial z} & -\frac{1}{r} \\ 0 & \frac{\partial}{\partial z} & (\frac{\partial}{\partial r}+\frac{1}{r}) & 0 \end{bmatrix} \tag{3.50}$$

The stress tensor is written as

$$T = \begin{bmatrix} T_{rr} & T_{zz} & T_{rz} & T_{\theta\theta} \end{bmatrix}^T = CS + H\dot{S} \tag{3.51}$$

For an isotropic medium

$$C = \begin{bmatrix} \lambda+2\mu & \lambda & 0 & \lambda \\ \lambda & \lambda+2\mu & 0 & \lambda \\ 0 & 0 & \mu & 0 \\ \lambda & \lambda & 0 & \lambda+2\mu \end{bmatrix} \quad H = \begin{bmatrix} H_{11} & H_{12} & 0 & H_{12} \\ H_{12} & H_{11} & 0 & H_{12} \\ 0 & 0 & H_{44} & 0 \\ H_{12} & H_{12} & 0 & H_{11} \end{bmatrix} \tag{3.52}$$

where $H_{44} = \frac{1}{2}(H_{11} - H_{12})$. For a transversely isotropic medium where the isotropic planes are normal to the z axis

$$C = \begin{bmatrix} C_{11} & C_{13} & 0 & C_{12} \\ C_{13} & C_{33} & 0 & C_{13} \\ 0 & 0 & C_{44} & 0 \\ C_{12} & C_{13} & 0 & C_{11} \end{bmatrix} \quad H = \begin{bmatrix} H_{11} & H_{13} & 0 & H_{12} \\ H_{13} & H_{33} & 0 & H_{13} \\ 0 & 0 & H_{44} & 0 \\ H_{12} & H_{13} & 0 & H_{11} \end{bmatrix} \tag{3.53}$$

Notice that for a fully anisotropic medium, the axisymmetric condition is not satisfied since there is always a θ dependence no matter what direction the z axis is.

The strain tensor is written as

$$S = \begin{bmatrix} S_{rr} & S_{zz} & 2S_{rz} & S_{\theta\theta} \end{bmatrix} = A\mathbf{u} \tag{3.54}$$

where

$$A = \begin{bmatrix} \frac{\partial}{\partial r} & 0 & \frac{\partial}{\partial z} & \frac{1}{r} \\ 0 & \frac{\partial}{\partial z} & \frac{\partial}{\partial r} & 0 \end{bmatrix}^T, \quad \mathbf{u} = \begin{bmatrix} u_r \\ u_z \end{bmatrix} \tag{3.55}$$

Upon discretization, the interpolation of the displacements in each element in terms of the nodal values is written as

$$\mathbf{u} = NU \tag{3.56}$$

and therefore

$$S = ANU = BU \tag{3.57}$$

where

$$B = AN \tag{3.58}$$

The elemental matrices are in a similar form as Eq. (3.42)

$$M^e = 2\pi \int\int \rho N^T N r dr dz \tag{3.59a}$$

$$K^e = 2\pi \int\int B^T C B r dr dz \tag{3.59b}$$

$$D^e = 2\pi \int\int B^T H B r dr dz \tag{3.59c}$$

$$R^e = \int_{S_t^e} N^T \underline{t} ds \tag{3.59d}$$

Eqs. (3.44-48) are also valid for the axisymmetric formulation with the xy coordinate replaced by the rz coordinate.

Modal Superposition Method

The global matrix equation derived in the above section is shown as follows with initial conditions

$$M\ddot{U} + D\dot{U} + KU = R \tag{3.60}$$

$$U(t_0) = U_0, \quad \dot{U}(t_0) = V_0 \tag{3.61}$$

While the traction boundary conditions are built in to the the equations through the forcing vector R, the displacement boundary conditions have to be enforced explicitly. The time domain solutions for the displacements and possibly their derivatives can be obtained with two general categories of approach, i.e., direct time integration and modal superposition. The direct integration methods are the most general methods and they can be used both for linear and nonlinear problems, whereas the modal superposition methods are linear methods and thus work only for linear problems. The two approaches are dealt with in this and the next sections, respectively.

In the modal superposition method, the semi-discretized system equations are transformed into a system of uncoupled equations. The nature of the method is to express the solutions for the displacements as the superposition of the free vibrational modes of the structural system. Let us start with the free vibration problem without damping

$$M\ddot{U} + KU = 0 \tag{3.62}$$

A harmonic solution $U = \bar{U}e^{j\omega t}$ leads to the following eigenvalue problem

$$(K - \lambda M)\bar{U} = 0 \tag{3.63}$$

where $\lambda = \omega^2$.

We denote λ_i and $\mathbf{v}_i$ as the eigenvalue and eigenvector pairs. It can be shown that the eigenvectors are orthogonal to M and K, i.e.,

$$\mathbf{v}_i^T M \mathbf{v}_j = 0, \quad \mathbf{v}_i^T K \mathbf{v}_j = 0 \tag{3.64}$$

for $i \neq j$. Suppose the eigenvectors $\mathbf{v}_i$ are normalized with M such that

$$\mathbf{v}_i^T M \mathbf{v}_i = 1 \tag{3.65}$$

The following relations can be obtained

$$\mathbf{v}_i^T M \mathbf{v}_i = \delta_{ij}, \quad \mathbf{v}_i^T K \mathbf{v}_j = \lambda_i \delta_{ij} \tag{3.66}$$

Suppose the eigenvalues in increasing order form the diagonal elements of a matrix, denoted by Λ, whose nondiagonal elements are zeros, and the corresponding eigenvectors represent the columns of another matrix denoted by V. The above relations become

$$V^T M V = I, \quad V^T K V = \Lambda \tag{3.67}$$

Multiplying the system equations by V^T we have

$$V^T M \ddot{U} + V^T D \dot{U} + V^T K U = V^T R \tag{3.68}$$

By introducing a new variable W so that $U = VW$, it follows that

$$V^T M V \ddot{W} + V^T D V \dot{W} + V^T K V W = V^T R \tag{3.69}$$

Utilizing Eq. (3.67) gives

$$\ddot{W} + V^T D V \dot{W} + \Lambda W = V^T R \tag{3.70}$$

Neglecting the viscous damping, we have

$$\ddot{W} + \Lambda W = V^T R \tag{3.71}$$

Eq. (3.71) represents a system of decoupled equations with the initial conditions transformed as

$$W(0) = V^T M U(0) \tag{3.72}$$

$$\dot{W}(0) = V^T M \dot{U}(0) \tag{3.73}$$

The decoupled equations (3.71) can be written on the component level as

$$\ddot{w}_i + \omega_i^2 w_i = \mathbf{v}_i^T R \tag{3.74}$$

The solution is given by the Duhamel integral

$$w_i(t) = \frac{1}{\omega_i} \int_0^t \mathbf{v}_i^T R sin\omega_i(t-\tau) d\tau + A_i sin\omega_i t + B_i cos\omega_i t \tag{3.75}$$

where the coefficients A_i and B_i are determined by the initial conditions (3.72) and (3.73). The decoupled equations can also be solved by available numerical integration schemes. Even Eq. (3.75) has to be evaluated through numerical methods. By substituting W back into U we obtain the solutions

$$U(t) = V^T W = \sum_{i=1}^{N} \mathbf{v}_i w_i(t) \tag{3.76}$$

If we take account of the damping effect, measures have to be taken on D to make (3.70) decoupled. One way is to assume that D satisfies

$$\mathbf{v}_i^T D \mathbf{v}_j = 2\omega_i \xi_j \delta_{ij} \tag{3.77}$$

where ξ_j is the modal damping coefficient. It should be noted that no indicial summing convention is used in this section. It follows that we have on the component level

$$\ddot{w}_i + 2\omega_i\xi_i\dot{w}_i + \omega_i^2 w_i = \mathbf{v}_i^T R \tag{3.78}$$

The solutions are given by

$$\begin{aligned} w_i(t) &= \frac{1}{\omega_i}\int_0^t \mathbf{v}_i^T R e^{-\xi_i\omega_i(t-\tau)} sin\bar{\omega}_i(t-\tau)d\tau \\ &\quad + e^{-\xi_i\omega_i t}(A_i sin\bar{\omega}_i t + B_i cos\bar{\omega}_i t \end{aligned} \tag{3.79}$$

where $\bar{\omega}_i = \omega_i\sqrt{1-\xi_i^2}$.

It is further noted that the damping matrix D was derived using the damping coefficient η or H. But since the modal damping can be measured much more conveniently, it is useful to construct D using the modal damping assumption. A general form that satisfies Eq. (3.77) is as follows

$$D = M\sum_k \alpha_k (M^{-1}K)^k \tag{3.80}$$

which reduces to the special case of Rayleigh damping if only two terms are chosen.

In summary, the preliminary work for modal analysis is the determination of the eigenvalues and eigenvectors. If the size of the matrices is large, it could take enormous computer time. But the effectiveness of the method is that in some problems it will result in sufficient accuracy by considering only a number of the lowest modes. Then only this number of eigenvalue-eigenvector pairs need to be determined and the same number of equations need to be solved. The choice of the number of modes depends on the specific problem such as the spatial distribution and frequency content.

Direct Integration Methods

Direct integration means that Eq. (3.60) is directly integrated through a numerical step-by-step procedure without transforming the equations to other forms. Suppose the solutions over the time range from $t = t_0 = 0$ to $t = T$ are to be sought. Then this region is divided into a certain number (N) of subintervals. Though the integration methods which follow work equally well for nonuniform intervals, we assume that the intervals are uniform and equal to Δt. The algorithms are to determine the solutions at $\Delta t, 2\Delta t, \cdots, t-\Delta t, t, t+\Delta t, \cdots, N\Delta t$. The solutions at $t+\Delta t = (i+1)\Delta t$ are based on those obtained for previous steps up to $t = i\Delta t$.

The Newmark method

To derive the algorithm in the Newmark method, we start with the Taylor series expansion of the displacement and its time derivative keeping terms up to the third-order derivative

$$U_{t+\Delta t} = U_t + \dot{U}_t \Delta t + \frac{1}{2}\ddot{U}_t \Delta t^2 + \frac{1}{6}(\ddot{U}_{t+\Delta t} - \ddot{U}_t)\Delta t^2 \tag{3.81}$$

$$\dot{U}_{t+\Delta t} = \dot{U}_t + \ddot{U}_t \Delta t + \frac{1}{2}(\ddot{U}_{t+\Delta t} - \ddot{U}_t)\Delta t \tag{3.82}$$

where the third time derivative has been replaced with the difference of the second time derivatives under the assumption of linear acceleration. The Newmark integration scheme extends the above equations by changing the numerical coefficients 1/6 in Eq. (3.81) and 1/2 in Eq. (3.82), to somewhat arbitrary parameters β and γ, respectively

$$U_{t+\Delta t} = U_t + \dot{U}_t \Delta t + \left[\left(\frac{1}{2} - \beta\right)\ddot{U}_t + \beta \ddot{U}_{t+\Delta t}\right]\Delta t^2 \tag{3.83}$$

$$\dot{U}_{t+\Delta t} = \dot{U}_t + \ddot{U}_t \Delta t + \left[(1-\gamma)\ddot{U}_t + \gamma \ddot{U}_{t+\Delta t}\right]\Delta t \tag{3.84}$$

where β and γ are chosen from experience. From Eq. (3.83) we have

$$\ddot{U}_{t+\Delta t} = \frac{1}{\beta \Delta t^2}(U_{t+\Delta t} - U_t) - \frac{1}{\beta \Delta t}\dot{U}_t + \left(1 - \frac{1}{2\beta}\right)\ddot{U}_t \tag{3.85}$$

Substituting Eq. (3.85) into (3.84) yields

$$\dot{U}_{t+\Delta t} = \frac{\gamma}{\beta \Delta t}(U_{t+\Delta t} - U_t) + \left(1 - \frac{\gamma}{\beta}\right)\dot{U}_t + \left(1 - \frac{1}{2\beta}\right)\ddot{U}_t \Delta t \tag{3.86}$$

At $t + \Delta t$ the system equations have the following form

$$M\ddot{U}_{t+\Delta t} + D\dot{U}_{t+\Delta t} + KU_{t+\Delta t} = R_{t+\Delta t} \tag{3.87}$$

Substituting Eqs. (3.85) and (3.86) into Eq. (3.87), we obtain

$$\left(\frac{1}{\beta \Delta t^2}M + \frac{\gamma}{\beta \Delta t}D + K\right)U_{t+\Delta t} = R_{t+\Delta t} + \left(\frac{1}{\beta \Delta t^2}M + \frac{\gamma}{\beta \Delta t}D\right)U_t$$
$$+ \left[\frac{1}{\beta \Delta t}M + \left(1 - \frac{\gamma}{\beta}\right)D\right]\dot{U}_t + \left[\left(\frac{1}{2\beta} - 1\right)M - \left(1 - \frac{\gamma}{2\beta}\right)D\Delta t\right]\ddot{U}_t \tag{3.88}$$

It is seen that the Newmark integration scheme is a single step implicit method. No starting procedure is needed for the time stepping. It can be shown that this method is unconditionally stable for suitably chosen β and γ This means that a larger time step can be used if desired. Appearance of the term involving K on the left side of Eq. (3.88) requires the computationally intensive matrix inversion procedure. Additional implicit integration schemes include the Houbolt method and the Wilson-θ method. They are three-step and one-step methods, respectively, and unconditionally stable with θ suitably chosen for the latter.

The central difference method

We adopt the following central difference approximations for the derivatives of displacements

$$\dot{U}_t = \frac{1}{2\Delta t}(U_{t+\Delta t} - U_{t-\Delta t}) \tag{3.89}$$

$$\ddot{U}_t = \frac{1}{\Delta t^2}(U_{t+\Delta t} - 2U_t + U_{t-\Delta t}) \tag{3.90}$$

which are derived from the Taylor series and the truncation error is in the order of Δt^2. Substituting Eqs. (3.89) and (3.90) into (3.60), we obtain

$$\left(\frac{1}{\Delta t^2}M + \frac{1}{2\Delta t}D\right)U_{t+\Delta t} = R_t - (K - \frac{2}{\Delta t^2}M)U_t - (\frac{2}{\Delta t^2}M - \frac{1}{2\Delta t}D)U_{t-\Delta t} \tag{3.91}$$

It is observed that the solutions at $t+\Delta t$ are determined on the basis of those at t and $t-\Delta t$. So this is a two step explicit integration scheme. Therefore a starting procedure is needed. In other words, the initial conditions at $-\Delta t$ are needed in addition to those given at $t = 0$ to evaluate the displacements at Δt. They can be obtained from the Taylor series expansion

$$U_{-\Delta t} = U_0 - \Delta t\dot{U}_0 + \frac{\Delta t^2}{2}\ddot{U}_0 \tag{3.92}$$

where $\ddot{U}_0$ can be evaluated from the system equations Eq. (3.60) at t=0.

As an alternative approach, we still use the central difference approximation for the second derivative but the backward difference approximation for the first derivative, i.e.,

$$\dot{U}_t = \frac{1}{\Delta t}(U_t - U_{t-\Delta t}) \tag{3.93}$$

which leads to

$$\frac{1}{\Delta t^2}MU_{t+\Delta t} = R_t - (K + \frac{1}{\Delta t}D - \frac{2}{\Delta t^2}M)U_t + (\frac{1}{\Delta t}D - \frac{1}{\Delta t^2}M)U_{t-\Delta t} \tag{3.94}$$

where only the positive definite mass matrix appears on the right hand side. This means that a mass lumping technique can be used to simplify the solution. By the following approximation

$$M_{ij}^{Diag} = \begin{cases} \alpha M_{ij} & \text{if } i = j \\ 0 & \text{if } i \neq j \end{cases} \tag{3.95}$$

where $\alpha = \sum_i \sum_j M_{ij} / \sum_i M_{ii}$ to keep to the total mass unchanged, we have from Eq. (3.94) that

$$\begin{aligned} U_{t+\Delta t} &= \Delta t^2 (M^{Diag})^{-1} R_t - (K + \frac{1}{\Delta t} D) \Delta t^2 (M^{Diag})^{-1} U_t + \\ &\quad + 2U_t + \Delta t (M^{Diag})^{-1} D U_{t-\Delta t} - U_{t-\Delta t} \end{aligned} \tag{3.96}$$

Therefore this is a two-step explicit method. With given initial conditions at $t = t_0$ for the displacements and their first time derivatives, the initial values for the displacements at $-\Delta t$ are determined form Eq. (3.92). The method is computationally efficient since no matrix inversion is needed. Also the assembly of elemental matrices is not necessary, that is , all the computations can be performed on the element level. However, as is shown in the following section, this method is conditionally stable which means that the integration time step is restricted for numerical stability.

As a numerical example, Fig. 3.1 shows the wave profile (Z-displacement) in an axisymmetric aluminum block based on the bilinear (four node quadrilateral) and quadratic (eight-node quadrilateral) element respectively. The excitation point force has a center frequency of 1 MHz. The modeled area 4×4 cm^2 is discretized into 200×200 elements. The total number of nodes is 40401 for the linear elements and is 120801 for the quadratic elements. The execution time is significantly longer for the latter because of the smaller time step required for numerical stability. Even so, there is not significant difference in the results. While quadratic elements should be advantageous for curved boundaries, the same order of accuracy can be achieved in wave propagation problems by using linear elements of little smaller size. The major results from now on are based on four-node quadrilateral elements with axisymmetric geometries.

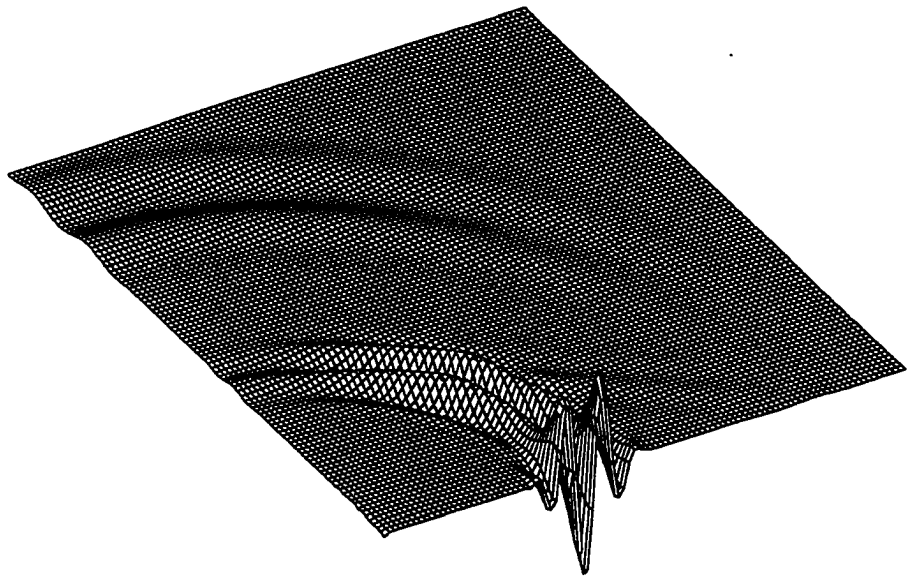

(a)

(b)

Figure 3.1: Wave profiles at $t = 7\mu s$ based on (a) bilinear elements (b) quadratic elements.

Stability analysis

It can be shown that the single-step Newmark algorithm in Eq. (3.88) is equivalent to the following two-step scheme

$$(M+\gamma\Delta tD+\beta\Delta t^2K)U_{t+\Delta t} \tag{3.97}$$

$$+(-2M+(1-2\gamma)\Delta tD+(1/2-2\beta+\gamma)\Delta t^2K)U_t \tag{3.98}$$

$$+(M-(1-\gamma)D+(1/2-\beta-\gamma)\Delta t^2K)U_{t-\Delta t}+\bar{R}_t=0 \tag{3.99}$$

where

$$\bar{R}_t=\beta R_{t+\Delta t}+(1/2-2\beta+\gamma)R_t+(1/2+\beta-\gamma)R_{t-\Delta t} \tag{3.100}$$

Because of the fact that positive damping is beneficial to the stability, we assume that $D=0$ and it follows that

$$(M+\beta\Delta t^2K)U_{t+\Delta t}+(-2M+(1/2-2\beta+\gamma)\Delta t^2K)U_t \tag{3.101}$$

$$+(M+(1/2-\beta-\gamma)\Delta t^2K)U_{t-\Delta t}+\bar{R}_t=0 \tag{3.102}$$

Using the transformation definitions defined in the modal analysis section, the above equation reduces to the following decoupled equations

$$(w_i)_{t+\Delta t}-(2-\phi)(w_i)_t+(1+\psi)(w_i)_{t+\Delta t}=0 \tag{3.103}$$

where $\phi=(\frac{1}{2}+\gamma)\sigma/(1+\beta\gamma)$, $\psi=(\frac{1}{2}-\gamma)\sigma/(1+\beta\gamma)$, $\sigma=(\omega_i\Delta t)^2$, and $\bar{r}_t=0$ due to the fact that the stability problem is for arbitrary initial conditions. By assuming that $(w_i)_{t+\Delta t}=\lambda(w_i)_t$, $(w_i)_t=\lambda(w_i)_{t-\Delta t}$ we obtain the following characteristic equation about λ

$$\lambda^2-(2-\phi)\lambda+1+\psi=0 \tag{3.104}$$

Stability requires that

$$| \lambda_i | \leq 1 \tag{3.105}$$

In order for the solutions to be stable for any Δt, it can be shown by solving Eq. (3.104) that the following conditions must to true

$$\gamma \geq \frac{1}{2}, \quad \beta \geq \frac{1}{4}(\frac{1}{2} + \gamma)^2 \tag{3.106}$$

which are the unconditional stability conditions for the Newmark integration scheme. If these conditions are not satisfied, conditional stability exists for $\Delta t \leq \Delta t_{cr}$ where

$$\Delta t_{cr} = \frac{2}{\omega_{max}\sqrt{(1/2 + \gamma) - 4\beta}} \tag{3.107}$$

in which ω_{max} is the highest natural frequency in the system.

For the central difference method, which is a special case of the Newmark method with $\beta = 0$ and $\gamma = 1/2$, only conditional stability can be achieved. From Eq. (3.107)

$$\Delta t_{cr} = \frac{2}{\omega_{max}} \tag{3.108}$$

For the bilinear quadrilateral elements or hexahedral elements, the maximum natural frequency is [49,50]

$$\omega_{max} \leq V_l g^{1/2} \tag{3.109}$$

and the corresponding stability condition is

$$\Delta t \leq \frac{2}{V_l g^{1/2}} \tag{3.110}$$

where V_l is the longitudinal wave velocity and g is a geometric parameter. For the four-node quadrilateral element, g is in the following form

$$g = \frac{4}{A^2} \sum_{i=1}^{2} \sum_{I=1}^{4} B_{iI}^2 \tag{3.111}$$

where

$$[B_{iI}] = \frac{1}{2}\begin{bmatrix} (y_2 - y_4) & (y_3 - y_1) & (y_4 - y_2) & (y_1 - y_3) \\ (x_4 - x_2) & (x_1 - x_3) & (x_2 - x_4) & (x_3 - x_1) \end{bmatrix} \tag{3.112}$$

where $(x_I,\ y_I)$ are the coordinates of node I and A is the element area. For a rectangular element with sides h_1 and h_2, the above relation reduces to

$$\Delta t \leq \frac{1}{V_l(1/h_1^2 + 1/h_2^2)^{1/2}} \tag{3.113}$$

The two methods give similar accuracy for the same time step. It is shown from experience that the accuracy can be improved by using a consistent mass matrix with the implicit scheme while using a lumped diagonal mass matrix with the explicit scheme. For the central difference method, it can be shown that the lumped matrix not only simplifies the solution process but also enlarges the critical time step. As far as the spatial discretization is concerned, numerical study shows that eight or more nodes per shortest wavelength is necessary to predict the correct waveforms. It is a common practice that the time step should be as close as possible to the critical time step.

Mixed methods, notably the partitioning methods and the operator splitting methods, combine the positive features of the implicit and the explicit methods, i.e., keep the stability of the implicit schemes and achieve the computational efficiency of the explicit schemes. The partitioning methods treat different regions with different schemes. This is attractive to problems consisting of multi parts with distinguishing characteristics but requiring simultaneous solutions. An alternative approach is the operator splitting methods in which the effective stiffness matrix is split to avoid the solution of the whole system of equations.

Absorbing Boundary Conditions

In realistic NDE applications there are always materials which are so large that a full finite element solution is beyond the availability of the computer resources. Artificial boundaries are then naturally introduced for the numerical implementation and this necessarily creates reflections that do not exist in reality. The so called absorbing boundary conditions are used to eliminate or minimize the undesired reflections. A detailed review of various absorbing boundary conditions for wave propagation problems is given by Kausel et al. [51]. For time-dependent problems, a scheme based on the paraxial approximation is developed by Clayton and Engquist [52]. Here the viscous boundary conditions based on Lysmer et al. [53] and the non-reflective boundary conditions based on Smith [54] are adopted for the finite element formulation of NDE problems.

Viscous boundaries

The viscous boundary conditions for 2D or axisymmetric geometries are

$$t_n = a\rho V_l \dot{u}_n, \quad t_t = b\rho V_s \dot{u}_t \tag{3.114}$$

where $\dot{u}_n$, and $\dot{u}_t$ are the normal and tangential particle velocities on the surface; t_n, and t_t are the normal and tangential surface tractions; V_l, V_s are the longitudinal and shear wave velocities; ρ is the material density; and a, b are constants to be determined. For a plane L wave with incident angle θ, letting the reflection coefficients for both the reflected L wave and mode converted SV wave be zeros yields

$$a = \frac{1 - 2S^2 \sin^2\theta}{\cos\theta}, \quad b = \frac{S^2 \sin 2\theta}{\sin\nu} \tag{3.115}$$

where ν is the reflected angle of the mode converted SV wave and $S = V_s/V_l$. For an incident SV-wave with incident angle ν not greater than the critical angle, a similar procedure yields

$$a = \frac{\sin 2\nu}{\sin \theta}, \quad b = \frac{\cos 2\nu}{\cos \nu} \tag{3.116}$$

where θ is the reflected angle of the mode-converted L-wave.

It can be seen that a and b are independent of frequency and this implies that the corresponding boundary conditions can be implemented in the time domain. However the constants do depend on the angle of incidence which is generally not available. So approximate values for a and b have to be adopted. One such approximation is the standard viscous boundary which assumes unity value for both a and b. This condition does not result in a perfect absorber unless $S = 1/2$ and the incident wave is normal to the surface. Another approximation is based on a unified boundary condition [55] which assumes

$$a = \frac{8}{15\pi}(5 + 2S - 2S^2), \quad b = \frac{8}{15\pi}(3 + 2S) \tag{3.117}$$

It can be shown that the constant coefficients are dependent on frequency for surface waves, so there is no perfect surface wave absorber based on the viscous boundary conditions. Numerical study indicates that the unified boundary condition is a better surface wave absorber than the standard boundary condition. Both conditions yield better absorbing for L waves than for Shear and surface waves. For a 3-D geometry there is one more constant coefficient corresponding to the additional shear stress component.

Non-reflecting boundaries

Consider a plane L wave incident on a boundary perpendicular to the y axis. It can be shown that the unwanted reflections are completely canceled by the addition of the finite element solutions corresponding to the following two sets of boundary conditions

$$\text{BVP 1}: \quad u_y = 0, \quad \frac{\partial u_x}{\partial y} = 0 \tag{3.118a}$$

$$\text{BVP 2}: \quad u_x = 0, \quad \frac{\partial u_y}{\partial y} = 0 \tag{3.118b}$$

which is also valid for incident shear and surface waves. In general, for a corner with n adjoining boundaries, 2^n solutions are needed to cancel all the reflections. For instance, four and eight solutions are needed for a 2D and 3D corner, respectively. For a 2D corner of adjoining boundaries 1 (parallel to the y axis) and 2 (perpendicular to the y axis), the required four sets of boundary conditions are

$$\text{BVP 1}: \quad u_x^1 = 0, \quad \frac{\partial u_y^1}{\partial x} = 0, \quad u_y^2 = 0, \quad \frac{\partial u_x^2}{\partial y} = 0 \tag{3.119a}$$

$$\text{BVP 2}: \quad u_y^1 = 0, \quad \frac{\partial u_x^1}{\partial x} = 0, \quad u_x^2 = 0, \quad \frac{\partial u_y^2}{\partial y} = 0 \tag{3.119b}$$

$$\text{BVP 3}: \quad u_y^1 = 0, \quad \frac{\partial u_x^1}{\partial x} = 0, \quad u_y^2 = 0, \quad \frac{\partial u_x^2}{\partial y} = 0 \tag{3.119c}$$

$$\text{BVP 4}: \quad u_x^1 = 0, \quad \frac{\partial u_y^1}{\partial x} = 0, \quad u_x^2 = 0, \quad \frac{\partial u_y^2}{\partial y} = 0 \tag{3.120}$$

where the superscripts 1 and 2 distinguish the two non-reflection boundaries.

Numerical study shows perfect absorbing except for the high-order reflections which are significantly time-delayed and hardly affect the final solution. Comparisons of the viscous and non-reflection boundary conditions indicate the former is computationally efficient but does not absorb surface waves effectively whereas the

latter is just the opposite. In addition, a unique property of the latter approach is that it can also handle anisotropic media. A combination of the two types of boundary conditions can also be implemented. In this approach, the viscous boundary conditions are used for absorbing bulk waves and the non-reflection boundary is usually adopted only for the surface wave reflection boundary to minimize the number of necessary solutions.

CHAPTER 4. TRANSIENT FIELDS OF PULSED TRANSDUCERS IN SOLIDS

In ultrasonic NDE, an incident wave is generated by the transducer and interacts with the media involved in the test and any material defects. In order to interpret correctly the measurement signals which result from reflections or scattering, it is important to understand the radiated fields of the transducer in the media. A large amount of work done on scattering assumes a uniform plane incident wave. For realistic NDE applications, however, experimental wave signals must be interpreted on the basis of more complete models for the radiated fields. Both fluid and solid media are involved in ultrasonic NDE. The acoustic radiation in a fluid medium was originally formulated as the Rayleigh integral [56]. Solutions to the Rayleigh integral for ultrasonic radiation problems are reviewed by Harris [57] and Hutchins et al. [58]. Seki et al. [59] have calculated the pressure and phase profiles for the monochromatic radiation into an isotropic medium from a circular piston source. The extension to the case of anisotropic media with 2D and circular piston sources was performed by Papadakis [60,61]. Zemanek [62] has presented detailed beam profiles for the nearfield of a piston. The fields of broadband transducers are even more important because of their dominant applications in ultrasonic NDE. Papadakis and Fowler [63] have computed the pressure and phase profiles for the broadband transducer using

the approach of weighted superposition of single frequency sources. The impulse response approach to the radiation of a planar piston was developed by Stephanishen [64]. The nearfields of a pulsed piston radiator were calculated by Beaver [65] in the time domain on the basis of different excitation waveforms and rings of maximum and minimum pressure were observed in planes close to the piston surface. Mansour [66] reports the C-scan/ball target technique for transducer characterization in the space domain and also observes the rings in the nearfield pattern. Additional methods for various plots in the space domain have been reviewed by Papadakis [67]. Similar to Zemanek's work on continuous wave (CW) excitation [62], Weyns [68] has reported detailed beam behavior for planar as well as curved radiators with pulsed excitation.

All the above work has been based on a fluid model of the medium, i.e., only longitudinal velocities were assumed. The radiation and propagation of elastic waves in solids are more complicated in that the governing equation for a solid is not a simple wave equation as in the liquid case where only one single variable, i.e., the pressure, can describe the whole problem. Rose and Meyer [25] have presented a theoretical model for evaluating transducer-generated longitudinal waves in solids and compared it with finite difference results. Based on the Cagniard-de Hoop method [22], Aulenbacher and Langenberg [69] have obtained the impulse response and the directivity pattern of a point or line source radiating into a solid half-space. The radiation of a ribbon source has been evaluated by suitable numerical integration. Chang and Sachse [70] have also obtained the fields of extended sources by the numerical integration of point sources. A similar approach has also been adopted by Zhang et al. [71] for the radiated fields of a circular transducer. Kawashima [72] has evaluated the motion of an elastic half-space due to a uniform normal surface traction

by determining the single frequency transient waveform through direct numerical integration and then using superposition of harmonics. Weight [73] has presented a model for the axisymmetric transducer by extending the impulse response approach used extensively for fluids. The model shows the plane and edge waves in the solid and is in agreement with Kawashima's prediction. The shear edge wave has been considered to originate from the partial mode conversion from the longitudinal edge wave. Bresse and Hutchins [74] have solved the governing equations using a double Laplace-Hankel transform approach and obtain the impulse response of the source. The axial and radial components of the displacements generated by an axisymmetric normal force source have been formulated. The approach has been claimed to be superior to the superposition of point sources in terms of computational efficiency. Schmerr and Sedov [75] have presented a dynamic model for compressional and shear wave transducers. Analytical expressions for the displacement and stress fields are obtained based on the extension form fluid models. Finite difference modeling of pulsed radiation in solids has been performed by Harumi et al. [76] for a ribbon source and by Ilan and Weight [77] for an axisymmetric source. Fellinger and Langenberg [78] have adopted the so-called elastodynamic finite integration technique (EFIT), which is based on an approach originally developed for solving electromagnetic problems, to predict the wave fields of a two dimensional source.

In this chapter, a numerical model is developed for the transient field of a pulsed transducer in a solid medium with or without flaws. The problem involves solving the governing equations for elastic wave radiation and propagation in solids. Both analytical and numerical methods are available for the solution. Analytical methods are applicable only to simple geometries and are more difficult to apply to general

problems. The major numerical methods include the finite difference method (FDM), the finite element method (FEM) and the boundary element method (BEM), each of which has its advantages and drawbacks. A general review of numerical techniques for elastic wave propagation and scattering was given by Bond [79]. A majority of the work related to the numerical modeling of elastic waves has been done using the finite difference method. The modeling of radiation from a planar finite aperture has also been carried out using the finite element method [41,80]. This chapter also employs the finite element method and wave profiles are presented at different time moments along with A-scan plots at arbitrary spatial points. Both near and far field regions are covered. Axial fields using FEM with cosine excitation are compared with those of analytical solutions with continuous wave excitation. The scattering of simple smooth obstacles has been studied by different techniques [81-84]. However, a majority of the published results are based on incident plane waves, either continuous or pulsed. As part of this paper, the scattered transducer wave fields from spherical voids are also presented.

Numerical Modeling

Model assumptions

Fig. 4.1 shows the axisymmetric geometry for the pulsed transducer coupled with an isotropic solid medium to be modeled numerically. Aluminum is chosen as the medium (V_l=6300 m/s, V_s=3100 m/s, ρ=2700 kg/m^3). The piezoelectric transducer is modeled as a vibrating piston which generates a traction pulse. The pulse is applied normally and uniformly over the solid surface in contact with the transducer. The finite element method is used to predict the wave pattern with or

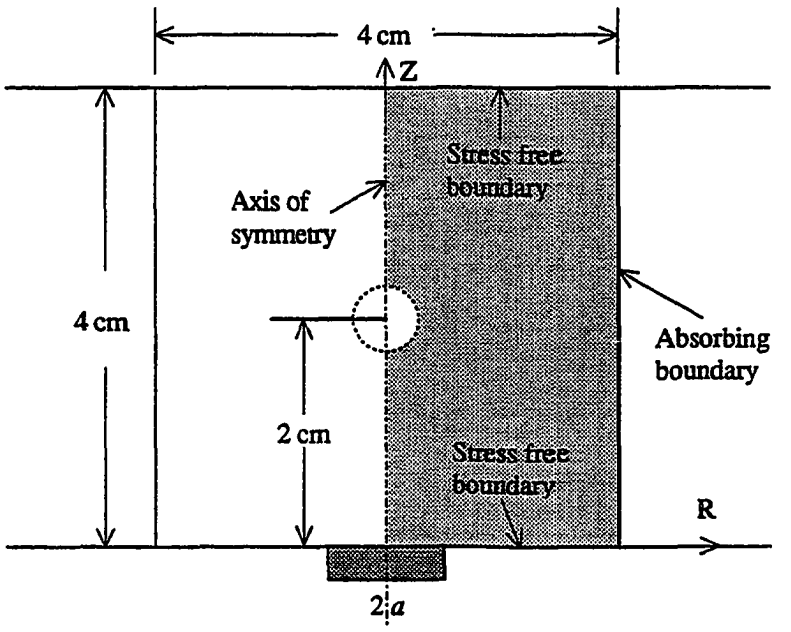

Figure 4.1: Axisymmetric geometry for modeling the pulsed transducer with or without defects in the solid.

without the spherical void. The displacement vector is the primary variable to be displayed. Axisymmetry assumes that the displacement along the rotation direction vanishes and therefore the degree of freedom per node is reduced to two representing the vertical (axial or Z) and horizontal (radial or R) displacements. Results are displayed for both components.

Form of the forcing function

The adopted driving signal is a traction force which is uniform within the transducer surface and normally applied to the solid surface. It is in the form of a raised cosine function of time,

$$f(t) = \left[u(t) - u(t - \frac{2n\pi}{\omega_o}\right] \left(1 - \cos\frac{\omega_o t}{n}\right) \cos\omega_o t \tag{4.1}$$

where $u(t)$ is the unit step function and

$$\omega_o = 2\pi f_o \tag{4.2}$$

in which $f_o = 5 \times 10^6$ Hz.

The integer n controls the pulse length and therefore the bandwidth. In this paper, excitation pulses 1, 2 and 3 correspond to n=3, 5, and 7 respectively, which is in the order of decreasing bandwidth, as shown in Fig. 4.2. Unless specified otherwise, the results are based on excitation pulse 1. For the finite element implementation, the uniform surface force is lumped into concentrated surface nodal forces. Using linear interpolation within each element, the nodal values (falling in the transducer

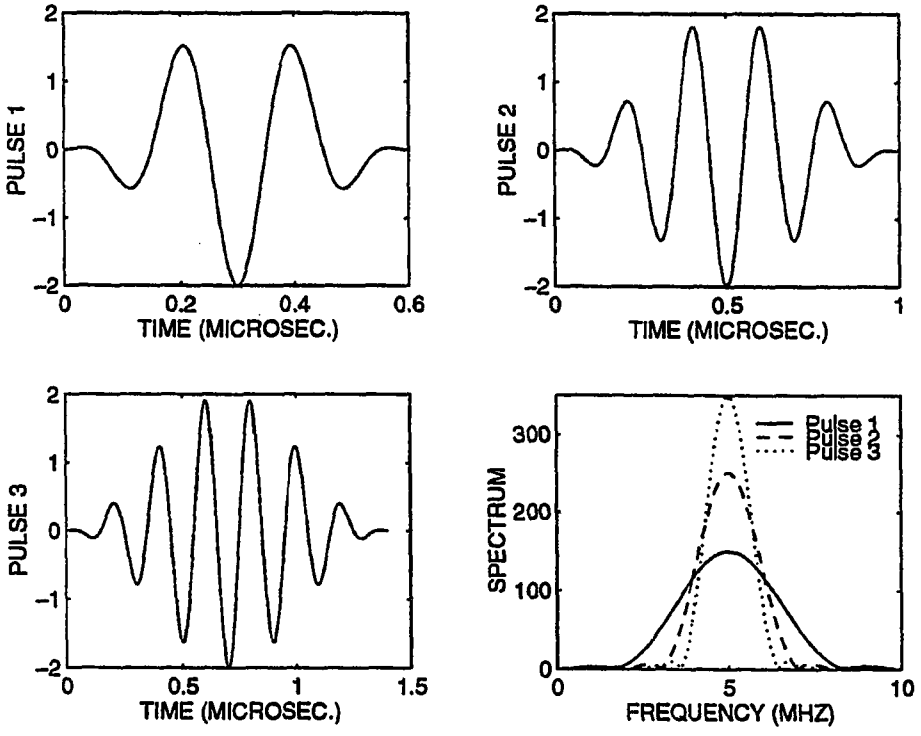

Figure 4.2: Excitation pulses of different bandwidth.

surface) are of the following form,

$$F(i) = \begin{cases} 1 & i = 1 \\ 6(i-1) & 1 < i < N \\ 3i - 4 & i = N \end{cases} \tag{4.3}$$

where i=1 and N correspond to r=0 and a, respectively, and a has been assumed to be an integer multiple of the element size. On the stress-free boundaries, both the normal and tangential stresses are assumed to be zero.

Artificial boundary conditions

On the axis of symmetry , the radial displacement and the radial derivatives of the axial displacement should vanish due to the nature of axisymmetry, i.e,

$$U_r = 0, \quad \frac{\partial U_z}{\partial r} = 0 \tag{4.4}$$

In the finite element implementation, the first equation in Eq. (4.4) is straightforward while the second is achieved by setting the nodal axial displacements on the axis and adjacent to the axis to be equal. The viscous boundary conditions described in Chapter 3 are adopted for the side boundary parallel to the axis of symmetry.

For the geometry of Fig. 4.1, simulated longitudinal pulses at z=2 cm on the axis are displayed in Fig. 4.3 using excitation pulse 1. Fig. 4.3 indicates the effects of the number of nodes (or more naturally, elements) per shear wavelength (NPSW). Decent accuracy can be reached using ten elements per shear wavelength. Based on this criterion, the half cross-section in Fig. 4.1 without flaws is discretized to three hundred by six hundred elements and the execution going through t=8 μs for Δt=5 ns takes about one hour on a DEC alpha station. For the case with spherical flaws,

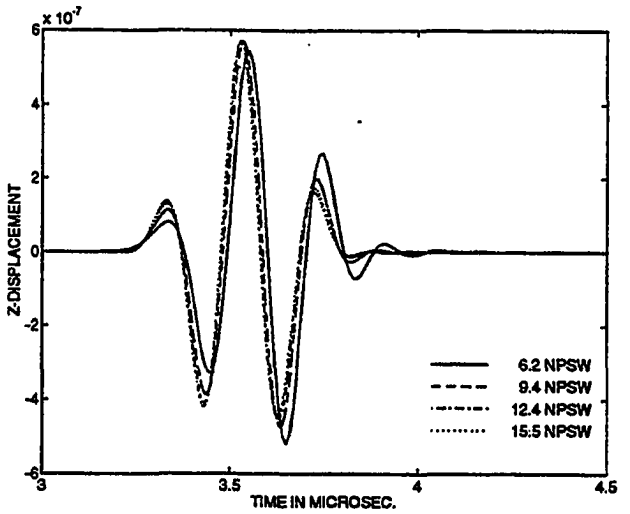

Figure 4.3: Simulated longitudinal pulses showing variation with different number of nodes per shear wavelength.

the more general quadrilateral elements are more expensive in terms of CPU time and memory requirement.

Farfield of a Point-like Source

To examine the farfield pattern, a point-like normal source is modeled. Radius of the source is 1.33×10^{-2} cm , corresponding to ka=0.66. Note that k corresponds to the longitudinal wave unless otherwise specified. The wave profile at t= 3 μs is shown in Fig. 4.4. The longitudinal (L), shear (S), head (H) and Rayleigh (R) surface wave fronts can be easily identified. Fig. 4.5 displays the longitudinal and shear wave field directivities which are computed based on the wave fronts at t=3 and 6 μs respectively. The plots are in good agreement with the finite difference model of Ilan and Weight [77]. It is noted that the polar plots have been normalized to unity.

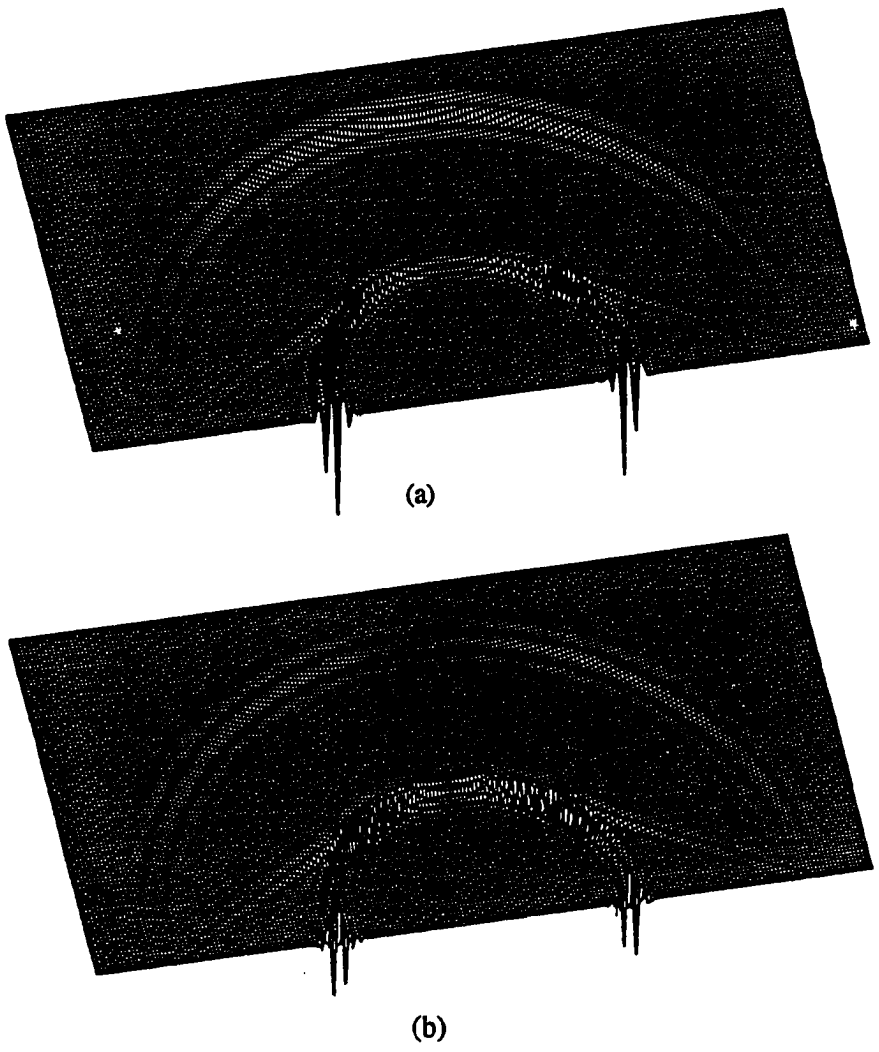

Figure 4.4: Wave profiles for the point-like source at t=3 μs, (a) Z-displacement, (b) R-displacement.

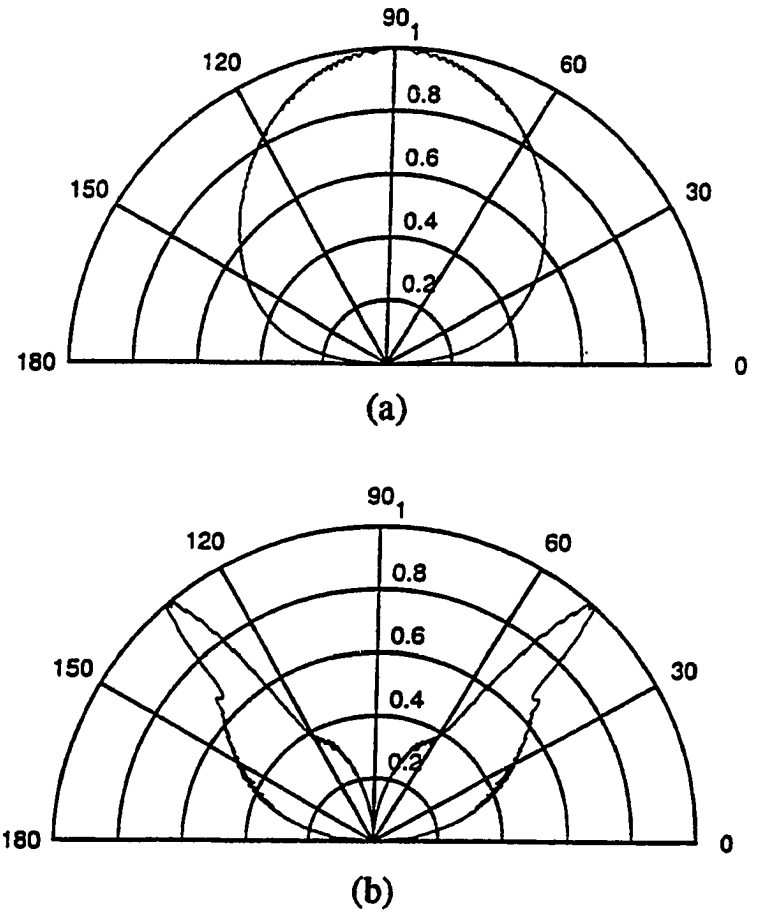

Figure 4.5: Farfield directivity pattern for the point-like source, (a) longitudinal wave, (b) shear wave.

Fields of a Finite Aperture Transducer

Based on the first excitation pulse shape, the computed wave profiles are shown in Fig. 4.6 for the axial displacement component and in Fig. 4.7 for the radial component at consecutive time instants, t=0.5, 1.0, 1.5, 3.0 and 6.0 μs. Five wave fronts can be identified, (1) the direct L wave which is a plane wave propagating from the transducer surface, (2) the longitudinal edge wave which is tangential to the direct wave, (3) the mode-converted shear edge wave, (4) the head wave which originates from the intersection point of the edge longitudinal wave front and the surface and is tangential to the edge shear wave, and (5) the surface wave which extends the shear edge wave and propagates along the surface with slightly lower velocity than the shear wave. It is noted that the transducer edge has a circular shape and hence the surface wave propagating inwards toward the center increases in magnitude because of focusing. On the other hand, the surface wave propagating outwards decays in the form of an outward cylindrical wave. The wave profiles for the planar transducer are in agreement with existing theories and experiments [71,86].

In order to look more closely at the phase relationships of the various wave components, another wave profile is generated with the following excitation signal

$$g(t) = \dot{f}(t) \tag{4.5}$$

where $f(t)$ is in the form of Eq. (18) but with n=1. The wave profile is as shown in Fig. 4.8. It can be seen that the direct longitudinal wave is in phase with the vertical component of the longitudinal edge wave outside the cylinder under the transducer but out of phase with that inside the cylinder. However, horizontal components of the longitudinal wave have a uniform phase inside and outside the cylinder. It should

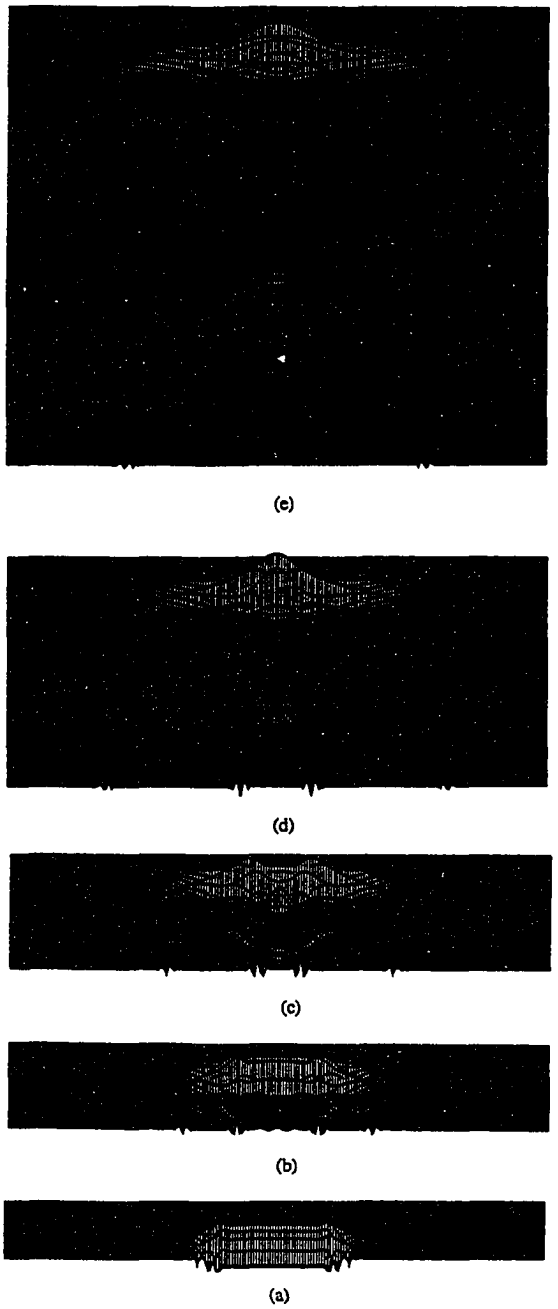

Figure 4.6: Z-displacement profiles for the pulsed transducer at time instants (a) 0.5, (b) 1.0, (c) 1.5, (d) 3.0 and (e) 6.0 μs.

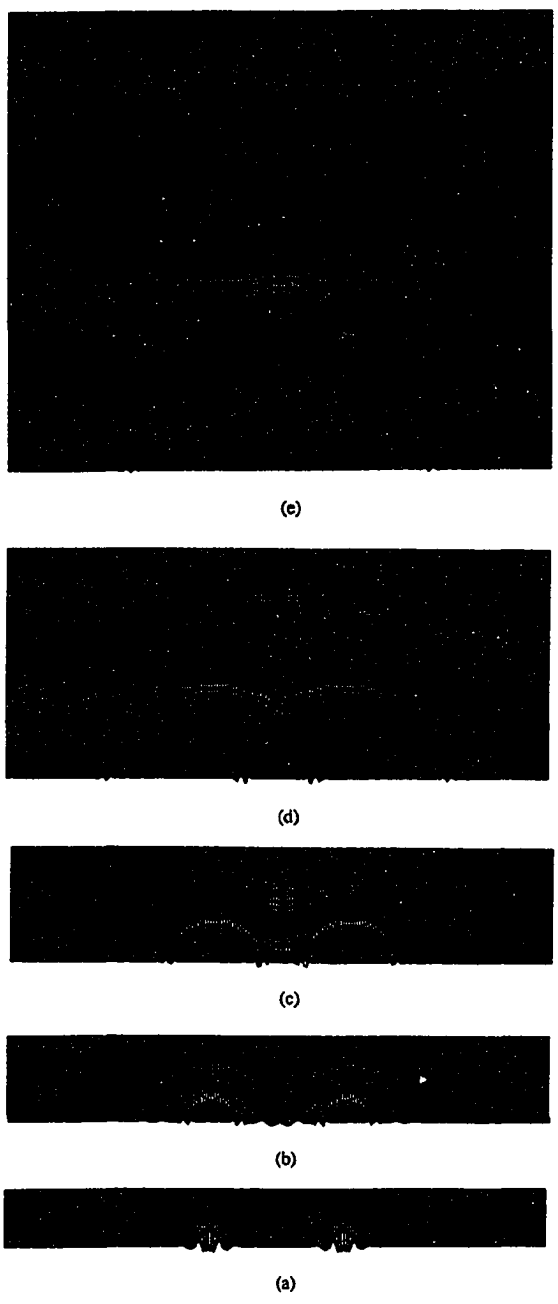

Figure 4.7: R-displacement profiles for the pulsed transducer at time instants (a) 0.5, (b) 1.0, (c) 1.5, (d) 3.0 and (e) 6.0 μs.

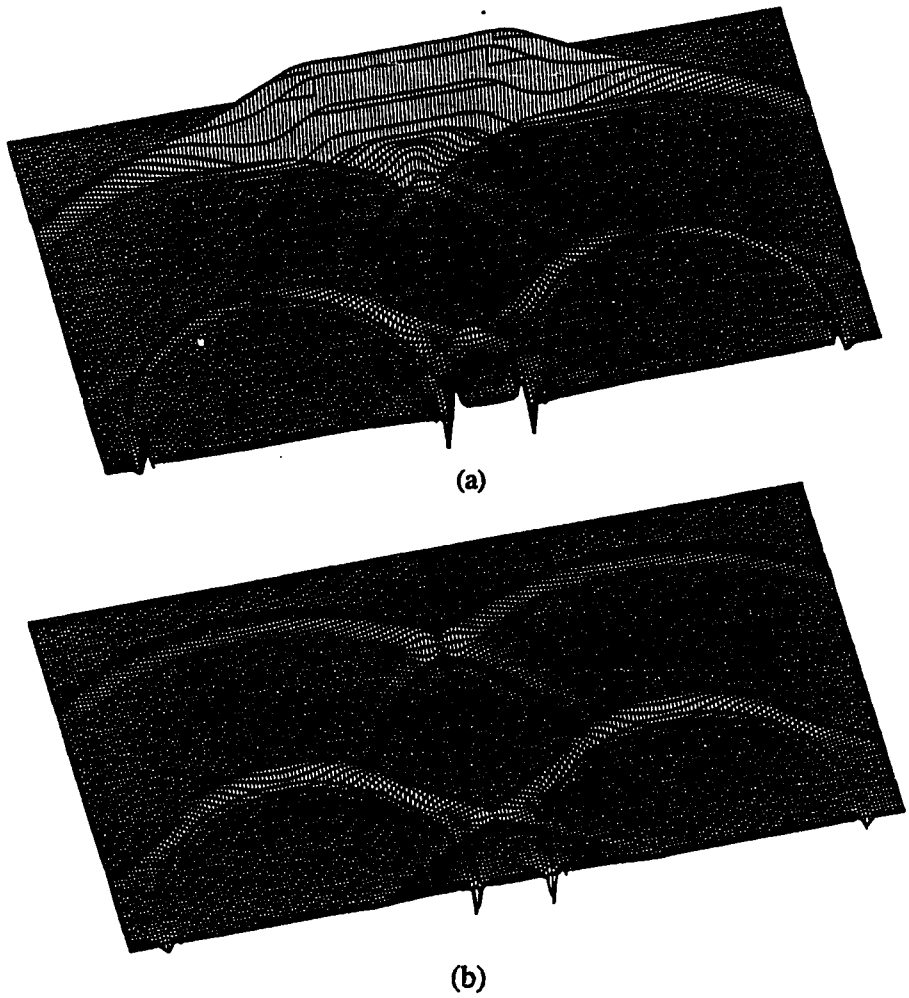

Figure 4.8: Wave profiles for identifying the phase relationship among the wave fronts.

be also noted that the shear edge wave and the longitudinal edge wave are in phase for their vertical components but out of phase for their horizontal components. In addition, the head waves are always of opposite phase to that of the associated shear edge wave. Finally, the reflected horizontal wave fronts at the axis of symmetry change phase due to the corresponding rigid boundary condition. Relevant results have also been reported in [77].

Fig. 4.9 shows the time dependent vertical displacements along the axis of symmetry and on the transducer plane associated with Fig. 4.1. On the axial displacement plot, the major wave front corresponds to the merged longitudinal direct and edge waves which deviate form each other near the transducer and a reflection occurs at the bottom stress free surface. The secondary wave front represents the superimposed shear edge wave along with the head wave which is more obvious close to the transducer. It is seen from Fig. 4.9(b) that the uniform wave front along the transducer surface corresponds to the direct longitudinal wave and the two wave fronts ahead of the direct wave are the longitudinal edge/head waves and converging surface wave respectively. It has been assumed that the transducer is ultrathin. The other two wave fronts represent the outward surface wave and the surface wave reflected from the axis of symmetry. For the present time period, no reflected wave from the bottom surface has been seen on the transducer surface.

Fig. 4.10 shows the numerically computed longitudinal displacement on the axis with the three different excitation pulses compared with the analytical CW case [85]. The plot defines the nearfield and farfield regions separated by the critical distance corresponding to the peak value which is seen to be in agreement with , where l is the longitudinal wavelength associated with the center frequency. The near fields

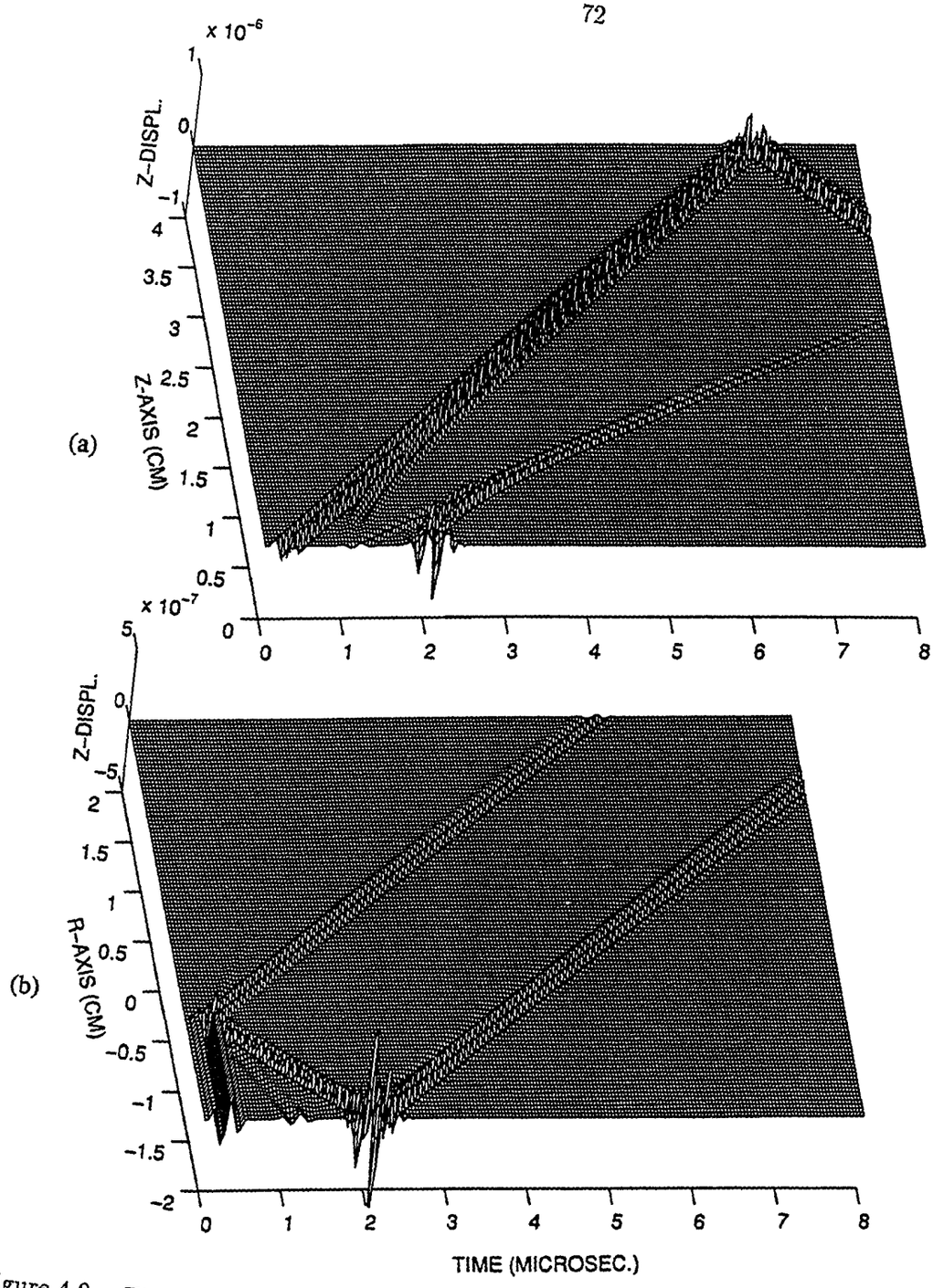

Figure 4.9: Time-dependent Z-displacement on (a) the axis of symmetry, (b) the transducer plane, without flaw in the medium.

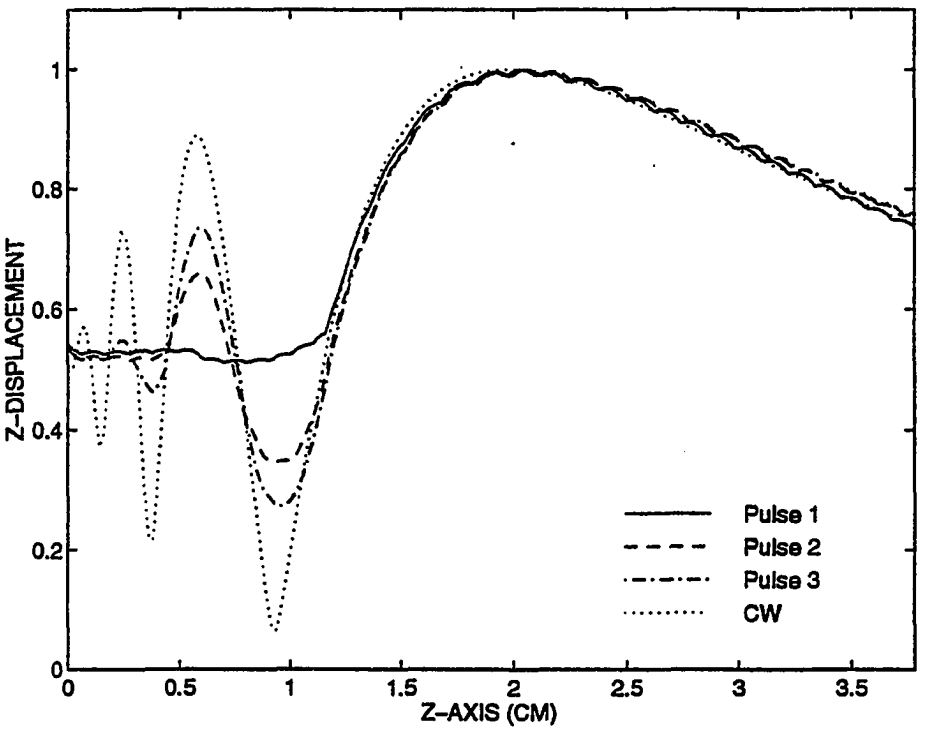

Figure 4.10: Magnitudes of longitudinal displacements on the axis of symmetry for different excitations.

differ significantly but the farfields are almost identical. This is very similar to the pressure fields of the transducer in fluid media. There exists stronger variations for longer excitation pulses in the near field which indicates the increasing interference with longer pulses or narrower bandwidth. Fig. 4.11 shows the vertical displacements associated with longitudinal waves at several horizontal planes. The field patterns at planes close to the transducer show strong variations for different pulses and the differences tend to vanish farther from the transducer. It also can be seen that close to the transducer stronger ripples appear for narrower-bandwidth pulses and the ripples show maximum amplitude at the cylindrical surface under the transducer edge and diminish toward the axis. This confirms the ring effect reported in the literature [65,66]. It is then obvious that the axial resolution associated with the near field can be improved by decreasing the pulse length.

Transducer Field Interaction with a Flaw

This section presents the scattered displacement fields by a spherical void in the solid subject to the incident wave from the transducer. Based on the diagram in Fig. 4.1, a spherical void is assumed at the location of z=2 cm on the axis with radius a=0.2 cm, corresponding to ka=10. Wave profiles at t=4.0, 5.5 and 8 μs are shown in Fig. 4.12 for the vertical displacements and in Fig. 4.13 for the horizontal displacements. At t=4 μs, the incident L wave has just past through and creeped to the shadow side of the void and continuously scattered L wave and mode-converted S wave are clearly displayed. At t=5.5 μs, the propagating longitudinal creeping wave front is seen between the scattered L and S waves and a less obvious shear creeping wave also exists along with the scattered S wave. At t=8 μs, the incident

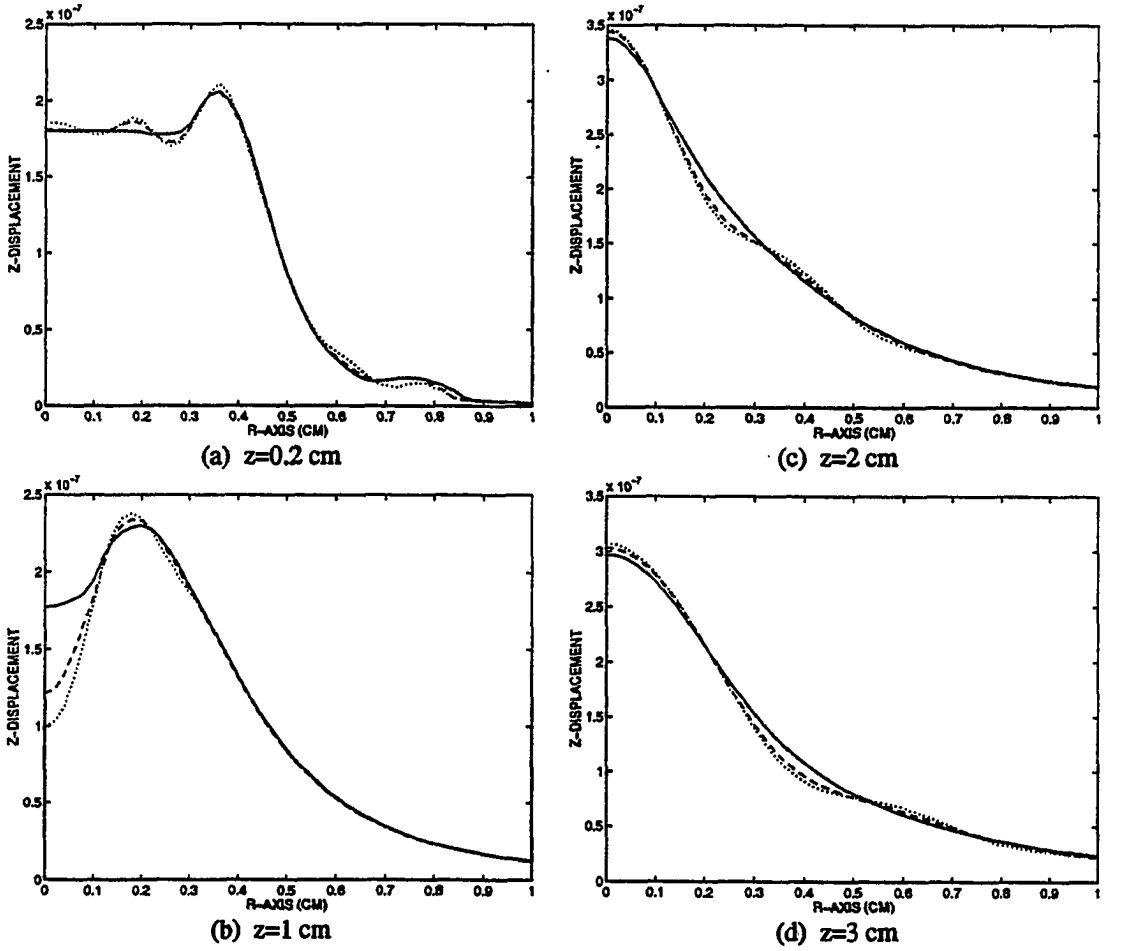

Figure 4.11: Magnitudes of longitudinal Z-displacements on planes parallel to the pulsed transducer, with excitation pulse 1 (solid line), excitation pulse 2 (dashed line), and excitation pulse 3 (dotted line).

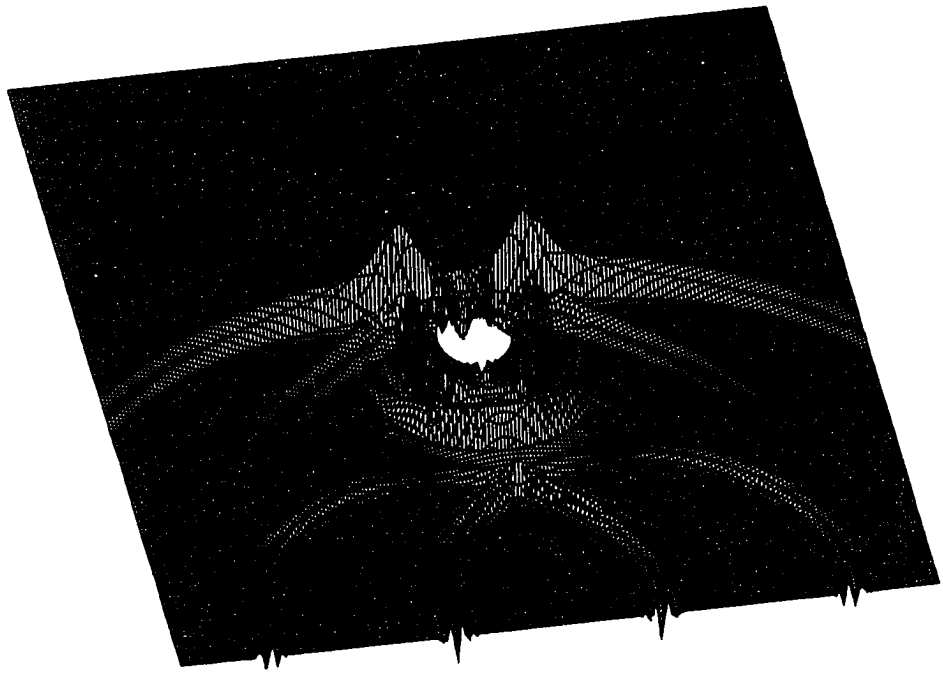

Figure 4.12: Z-displacement profiles for the medium with spherical void ka=10, (a) t=4 μs, (b) t=5.5 μs, and (c) t=8 μs.

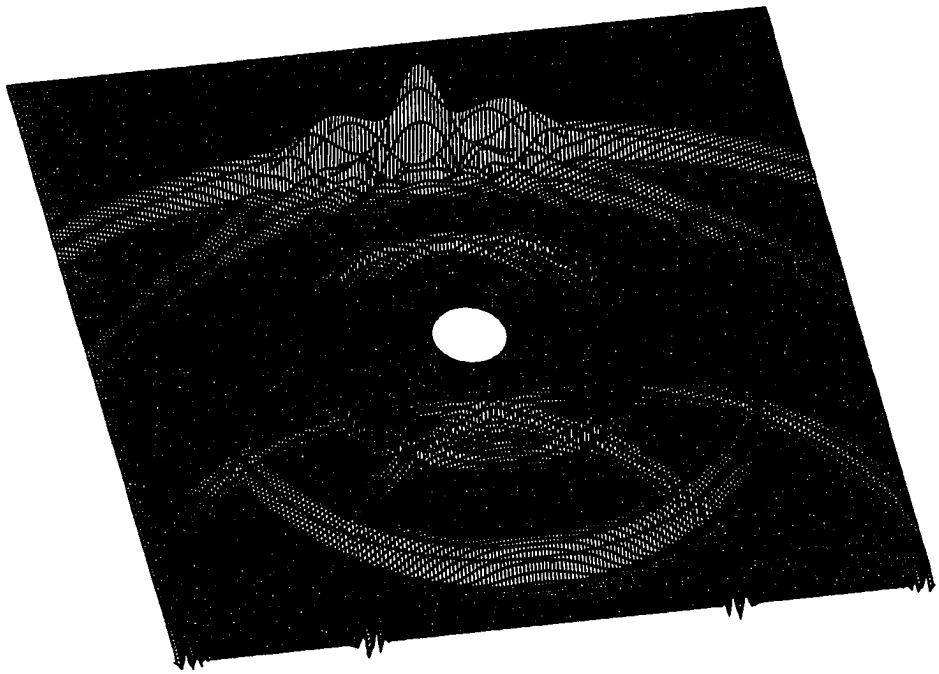

Figure 4.12 (Continued)

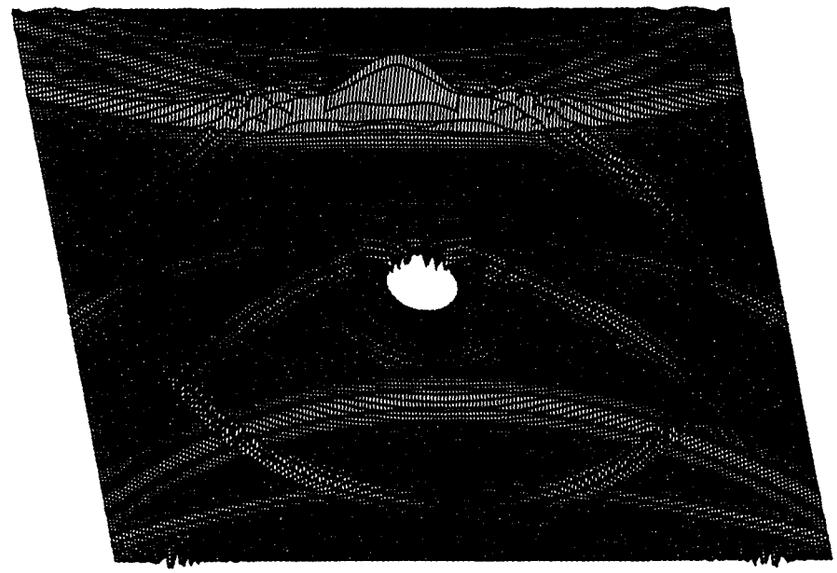

Figure 4.12 (Continued)

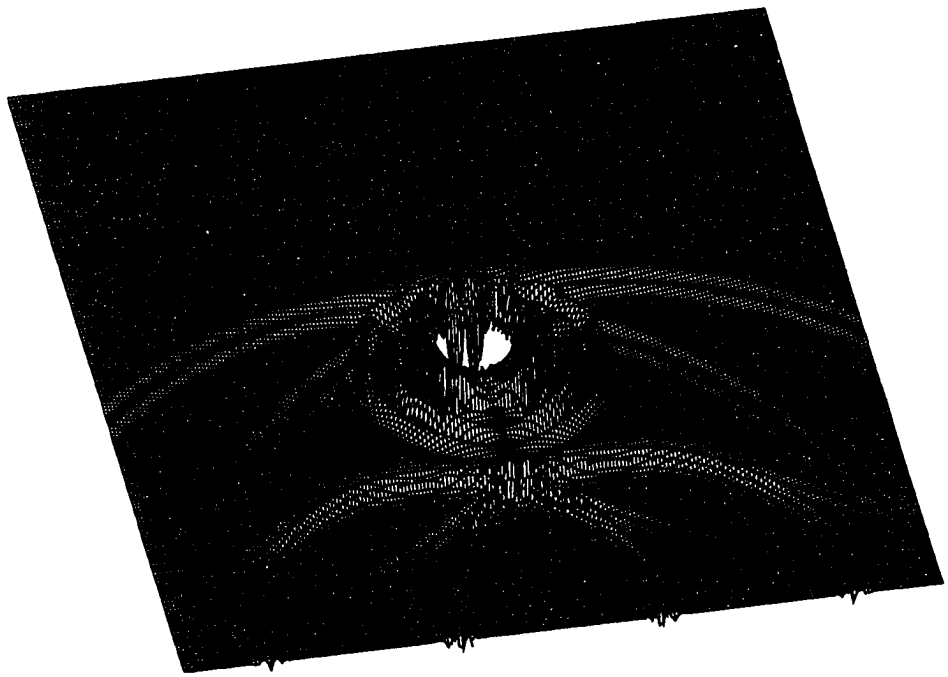

Figure 4.13: R-displacement profiles for the medium with spherical void ka=10, (a) t=4 μs, (b) t=5.5 μs, and (c) t=8 μs.

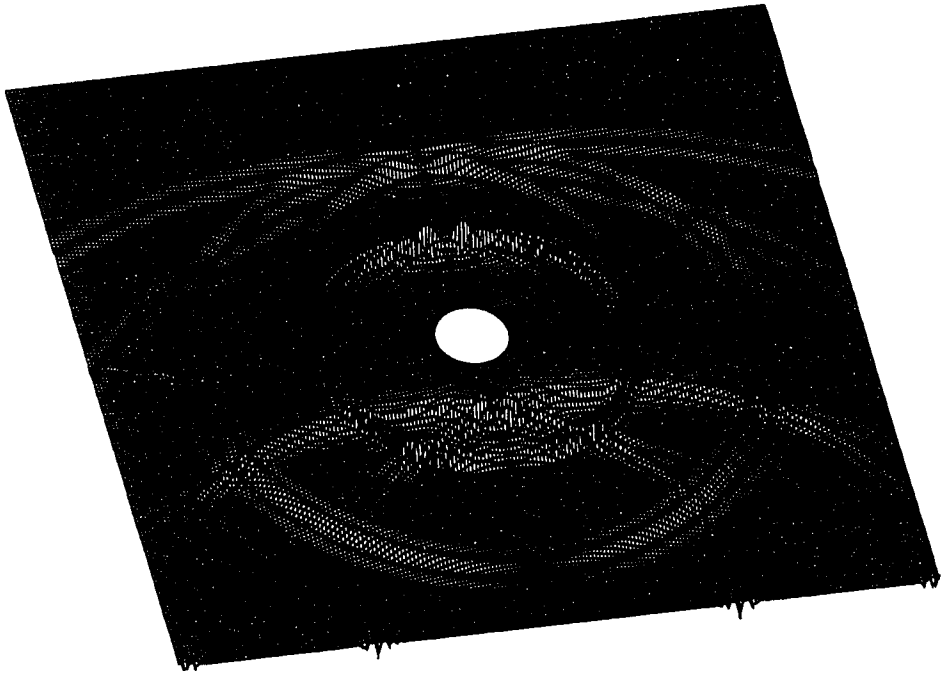

Figure 4.13 (Continued)

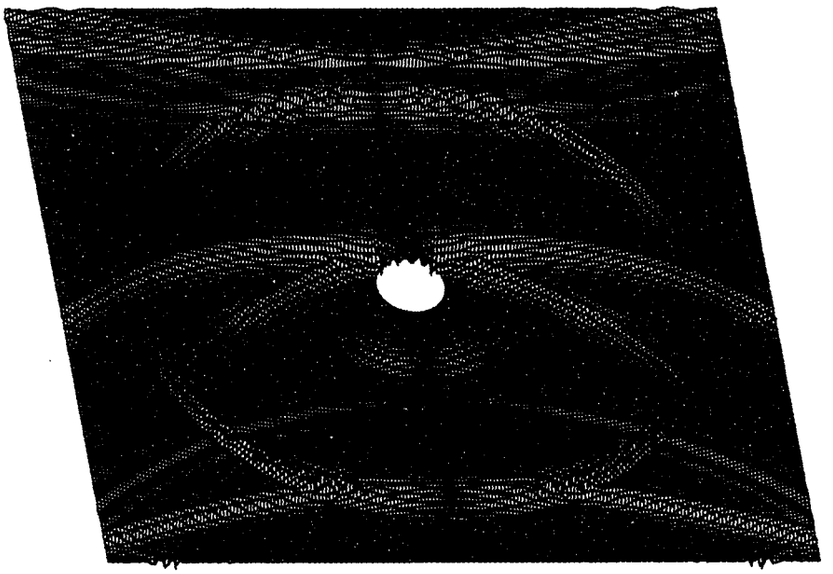

Figure 4.13 (Continued)

L wave and forward diffracted L wave have reflected from the back surface where mode-converted S waves are also generated. At the same time, the backscattered L wave has reached the front surface where both reflection and mode conversion also occur. In addition, the shear edge wave from the transducer has reached the void and creeped to the shadow side. A mode-converted L wave and a scattered S wave are generated from the incident S wave. It is seen from the wave profiles that the scattered L wave generated from the incident L wave has maximum amplitudes on the axis and minima around ninety degrees from the axis. On the other hand, the scattered S wave has minima on the axis and maxima around the ninety degrees from the axis.

As in the case without flaws, the A-scan plots for the points along the axis of symmetry and on the transducer plane are shown in Fig. 4.14(a) and (b) respectively. Fig. 4.14(a) is similar to that for the unflawed case of Fig. 4.9(a) except for the diffracted longitudinal and shear waves and a backscattered L wave. The backscattered wave also appears in Fig. 4.14(b) in contrast to Fig. 4.9(b). In addition, spheres at the same location but with ka= 5 and 20 are also modeled. The major differences lie in the forward diffracted and backward scattered waves as shown in Fig. 4.15. Fig. 4.15 (a) shows the backscattered L wave observed on the axis at the transducer plane. It is seen that the magnitude increases with the void size in a linear relationship in the specified range of ka values. Fig. 4.15(b) shows the longitudinal wave observed on the axis at the back surface. As expected from theories, the incident wave is less disturbed by smaller voids. From the conservation of energy point of view, Fig. 4.14(a) and (b) are consistent in that the total energy always keeps the same. For a incident longitudinal place wave excited with pulse 3, the scat-

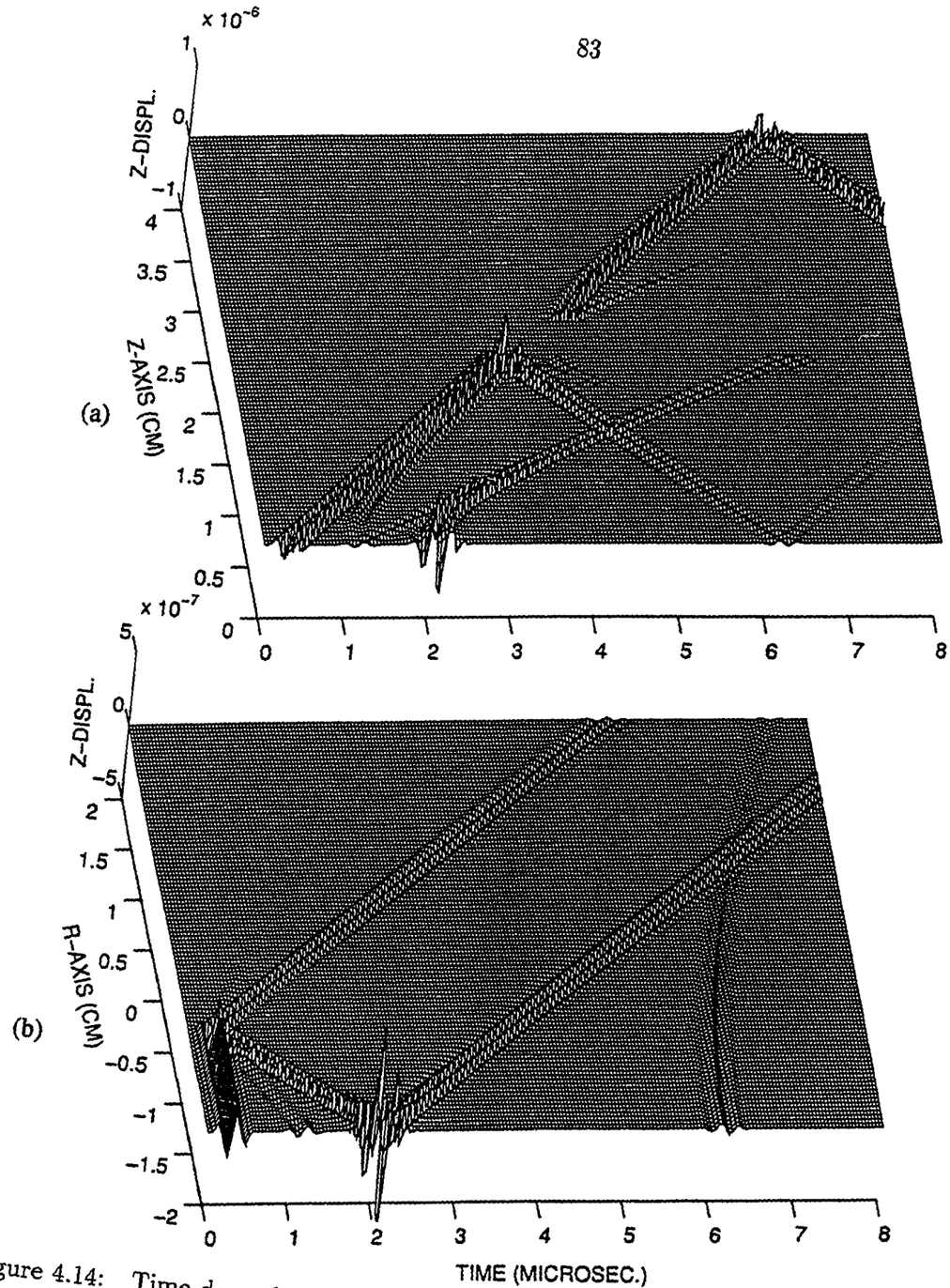

Figure 4.14: Time-dependent Z-displacement on (a) the axis of symmetry, (b) the transducer plane, with flaw in the medium.

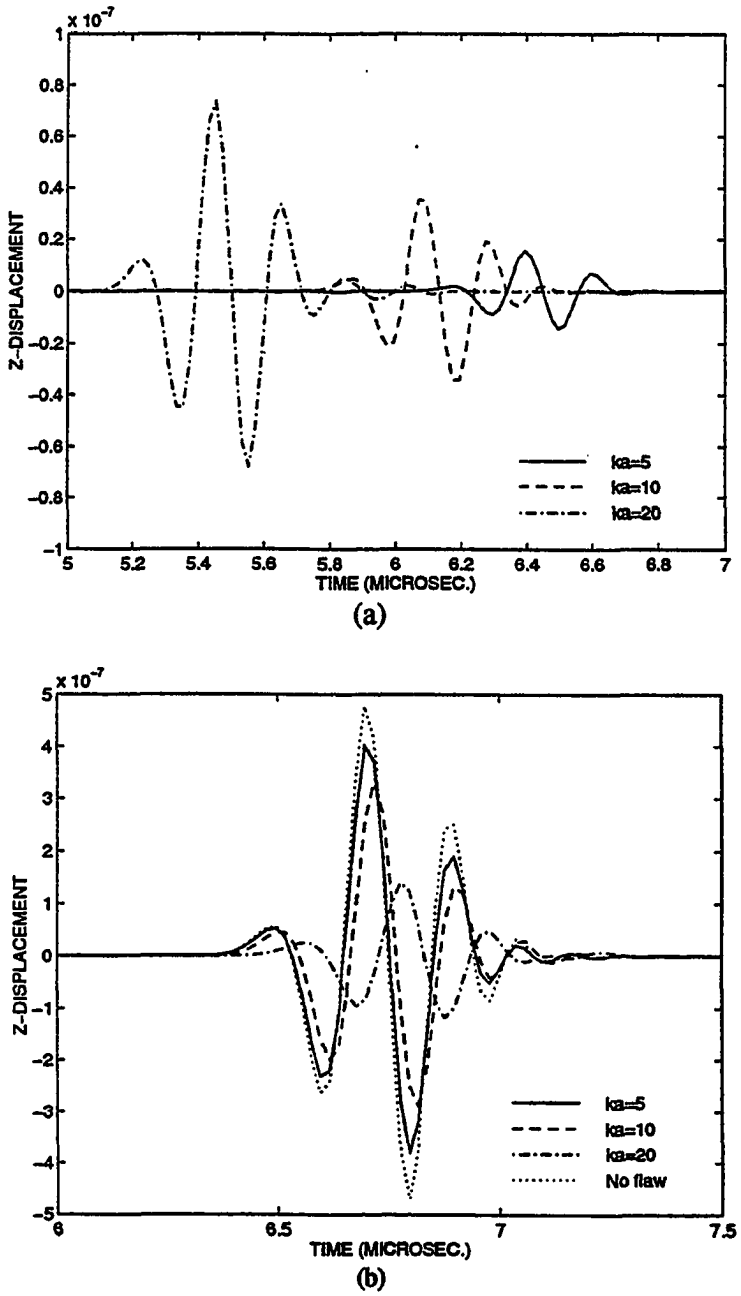

Figure 4.15: (a) The backscattered longitudinal pulses on the axis in the transducer plane, (b) the forward diffracted longitudinal pulses on the axis in the back surface.

tering patterns from spherical voids are shown in Fig. 4.16. The forward scattered longitudinal directivity drops with the decrease of the void size.

Additional Numerical Examples

Finite aperture transducer fields scattered from a penny shaped crack

The waves from a finite aperture transducer propagating in a aluminum plate containing a flat penny-shaped crack are shown in Figs. 4.17 and 4.18. The excitation signal is in the form of Eq. (4.1) with n=3 and f_o = 1 MHz. The thickness of the plate is 12 cm and the transducer with a diameter of 4 cm is centered on the front surface. The crack, which is 0.8 cm in radius and a few percent of a longitudinal wavelength is parallel to the plate surface and 7 cm from the transducer surface. A viscous boundary condition is applied to the boundary at r=8 cm. The modeled area is also discretized into quadrilateral elements. Fig. 4.17(a) (t=12 microseconds) indicates the wave front approaching the crack. In Fig. 4.17(b) (t=18 microseconds), the direct longitudinal wave has been scattered by the crack. The scattered longitudinal and shear waves are obvious. In Fig. 4.17(c) (t=28 microseconds), the forward longitudinal wave has been reflected from the back surface and reaches the crack again. On the other end, the back scattered longitudinal wave is reflected from the front surface. The reflection of a longitudinal wave from a traction-free surface is accompanied by a mode converted shear wave.

Fig. 4.18 shows the simulated A-scan signals on the front surface, (a) r=0 and (b) r= 3 cm. The plots consist of A-scans for the plate associated with Fig. 4.17 with and without crack. The pulses can be easily recognized by examining Fig. 4.17. Based on the time of flight of backscattered signals, the thickness of the plate as well

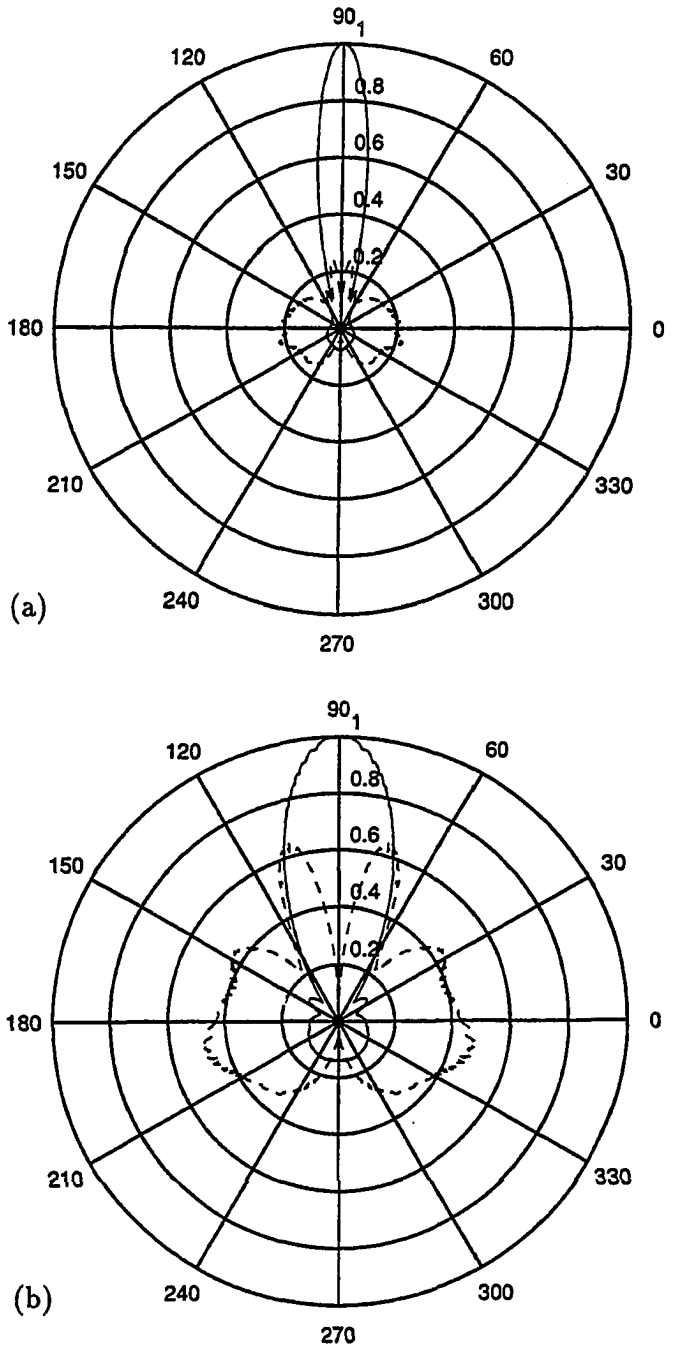

Figure 4.16: Farfield plane wave scattering pattern from a spherical void of radius (a) r=0.2 cm and (b) r=0.1 cm. The solid and dashed lines stand for the scattered L and S waves.

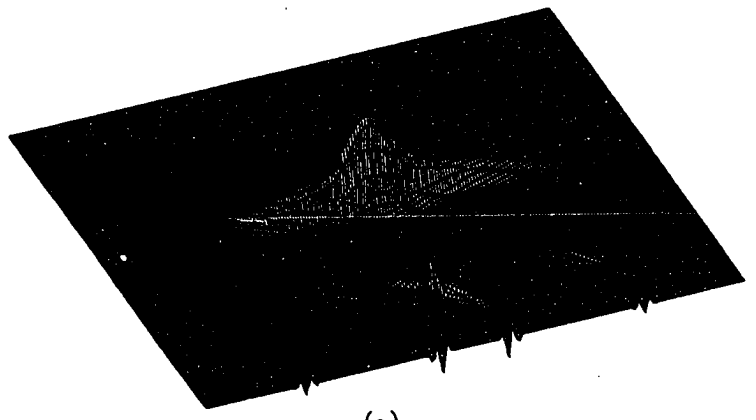

(a)

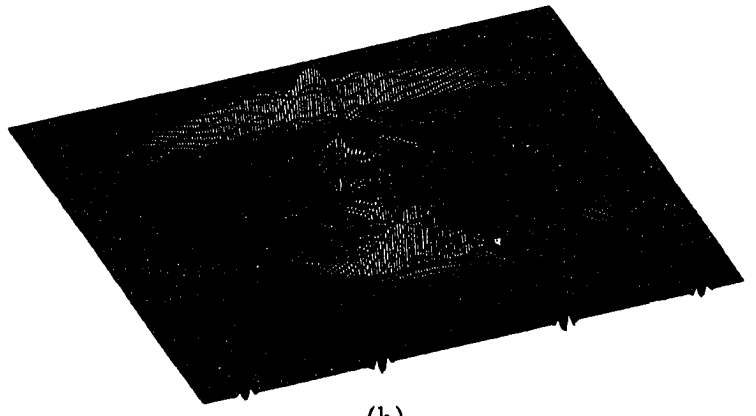

(b)

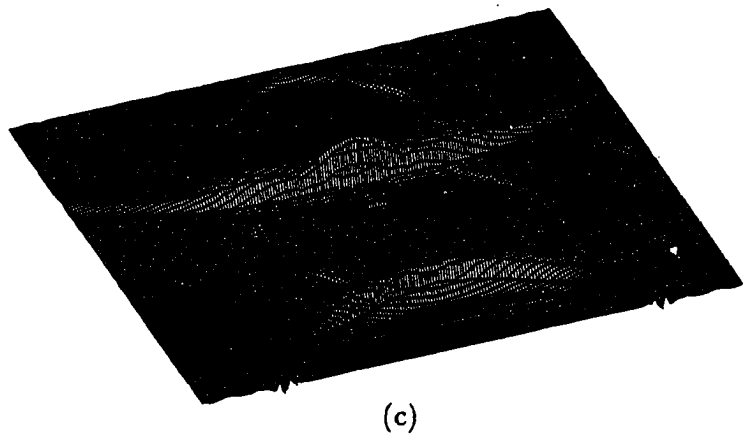

(c)

Figure 4.17: Wave profiles for a plane L wave scattering from a disk shaped crack, (a) t=12, (b) t=18 and (c) t=28 μs.

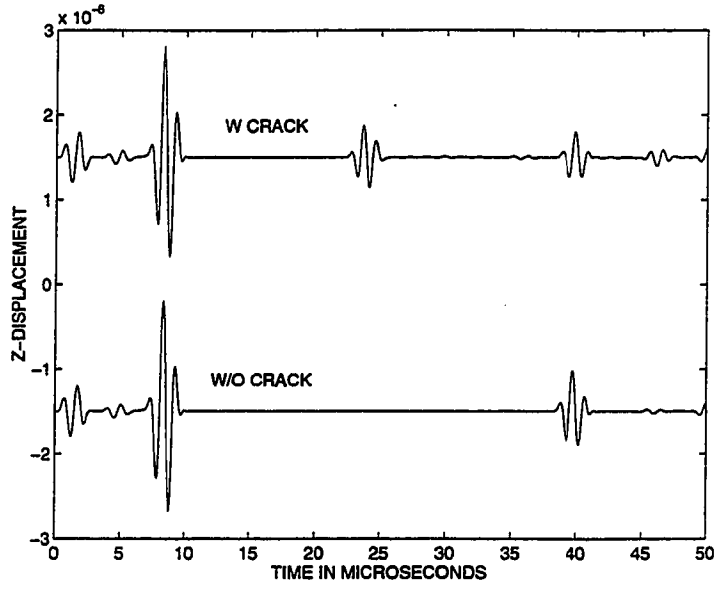

(a)

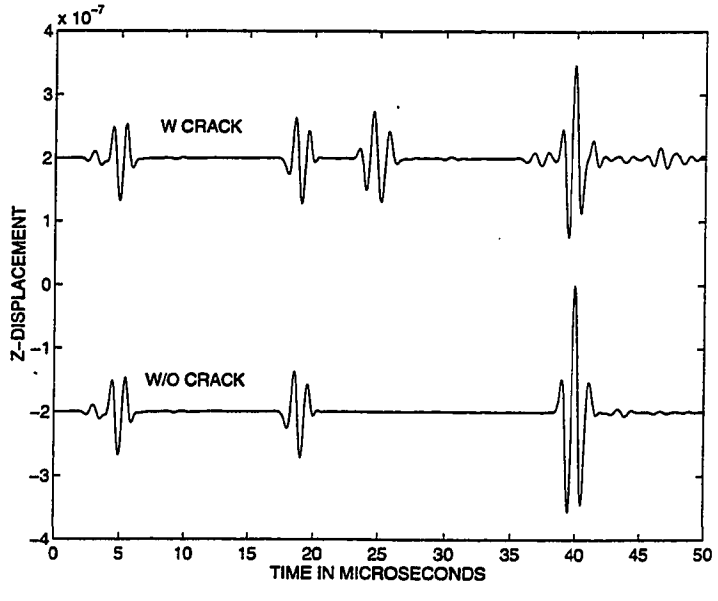

(b)

Figure 4.18: Simulated A-scan signals on the front surface, (a) r=0 and (b) r= 3 cm.

as the location of the crack can be determined. For instance, it can be seen from Fig. 4.18(a) that the round trip time for the longitudinal wave is 38.1 microseconds to and from the back surface and 22.2 microseconds to and from the crack. The thickness of the plate and the location of the crack are indeed confirmed by the products of these time intervals and the longitudinal velocity divided by two.

Plane waves scattering from crack in 2D geometry

The cross-sectional area of the 2D geometry is 6 cm by 6 cm, which is discretized into triangular elements. An incident longitudinal wave is assumed propagating in the x direction while the plane wave front is parallel to the y direction. The driving signal has the form of Eq. 4.5 with n=3 and f_o = 1 MHz. Figs. 4.19 to 4.21 show the displacement wave profiles at t= 9 microseconds after the incident wave is launched. They correspond to the scattering of plane waves by various cracks with their tips at the center of the geometry. The crack is a few percent of the wavelength in thickness and a traction free condition is assumed on both its sides. In Figs. 4.19 to 4.21 the cracks are in the y direction (parallel to the incident wave front), x direction (normal to the incident wave front) and x=y direction (45 degrees with the incident wave front), respectively. In each figure, (a) and (b) represent the x and y displacements respectively. In each case, there are scattered longitudinal, shear and head waves. The magnitudes and phase relationships for the scattered waves can also be seen in each plot. Though only longitudinal incident waves are considered here, shear incident waves yield qualitatively similar scattering patterns.

As a summary, a finite element model is developed for the transient radiation of pulsed transducers in solids. The model is capable of predicting every wave phe-

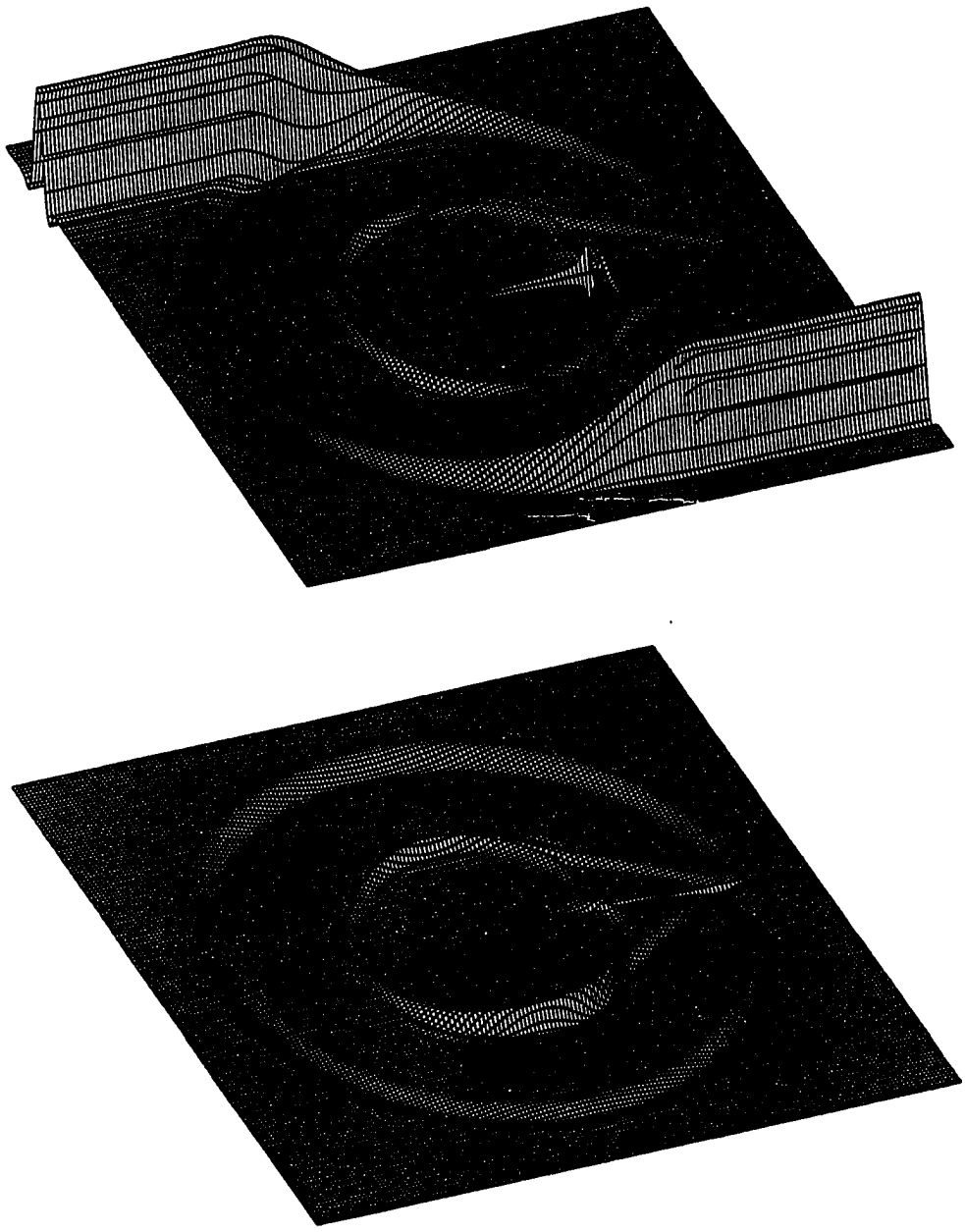

Figure 4.19: Scattering of a plane wave from a horizontal crack.

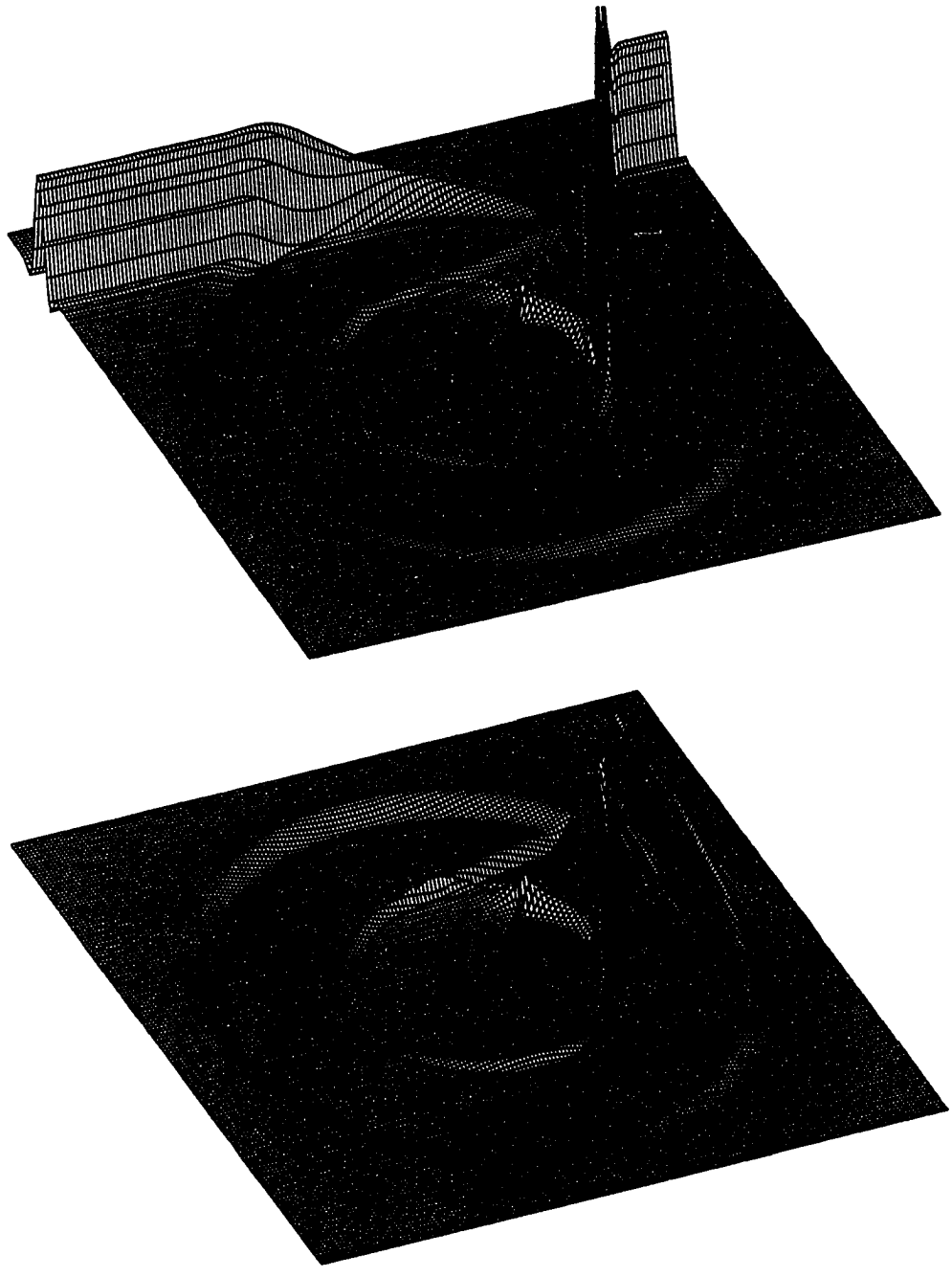

Figure 4.20: Scattering of a plane wave from a oblique crack.

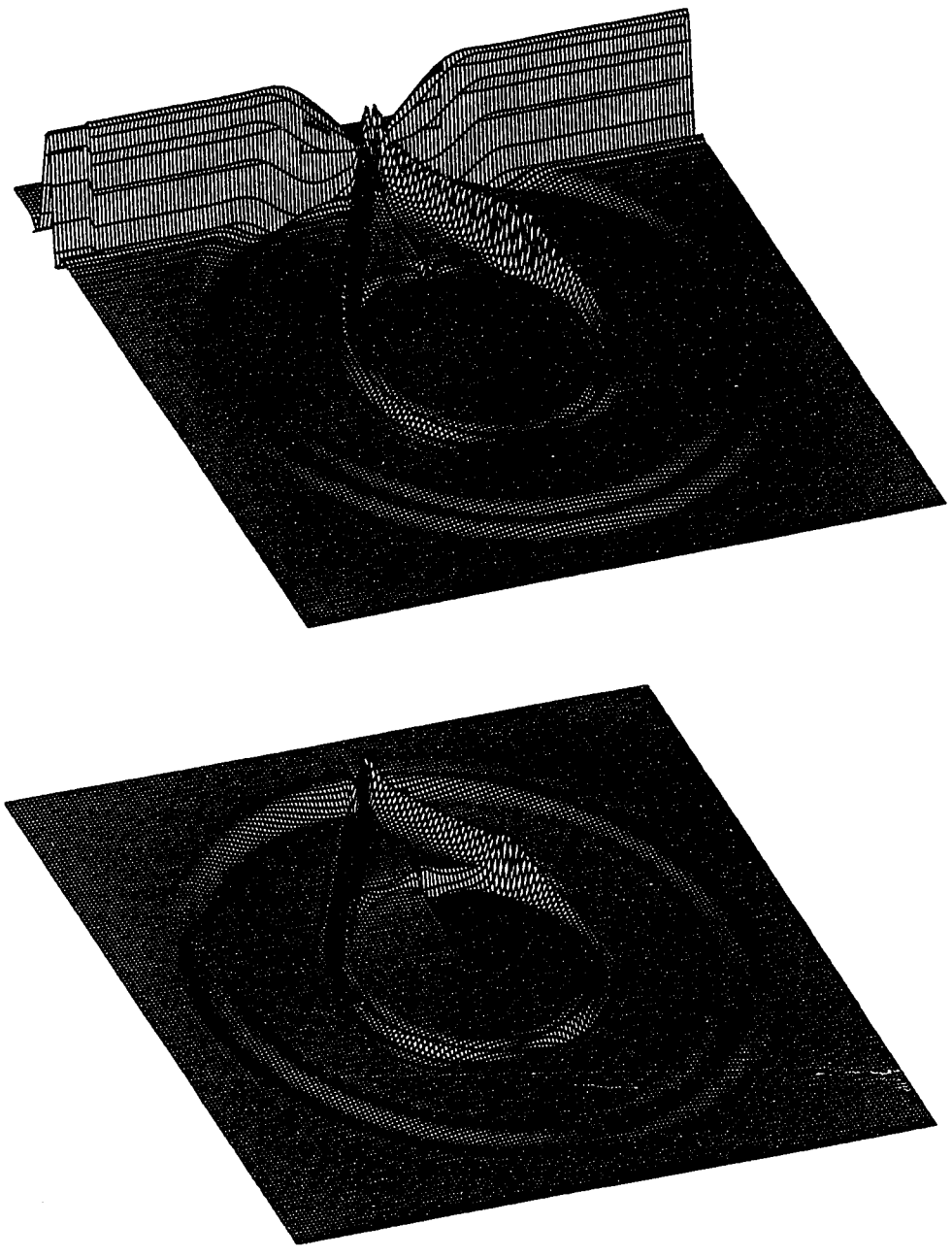

Figure 4.21: Scattering of a plane wave from a vertical crack.

nomenon in ultrasonic NDE including radiation, transmission, reflection, diffraction and scattering, and mode conversion. It is a valuable tool for transducer analysis and design. The results presented demonstrate the versatility of the finite element method for solving problems of arbitrary geometry. With a modification to the constitutive matrix the model can be readily used for general anisotropic media. Alternative forms of excitation forces can also be readily implemented if desired.

CHAPTER 5. TREATMENT FOR ACOUSTIC MEDIA AND FLUID/SOLID INTERFACES

A general ultrasonic NDE system includes not only elastic media but also acoustic media, as well as fluid/solid interfaces. An accurate model for the system must take account of the fluid/solid interface. When dealing with problems containing such an interface, the governing equations for both the solid and fluid media have to be solved simultaneously with the interfacing boundary conditions properly satisfied.

Analytical solutions work only for simple cases but find difficulty in dealing with general wave phenomena at a solid/fluid interface (especially curved interfaces). Therefore, numerical solutions have to be adopted. Among the various numerical approaches, one may be more advantageous over another depending on the specific problem. Based on the finite element approach, the deformation field of the solid medium is most conveniently represented by the displacement vector while the field for the fluid medium can be either represented by the displacement vector or the scalar pressure. A displacement formulation for the fluid through mock fluid elements yields symmetric and banded coefficient matrices but requires a larger number of variables due to the greater degree of freedom (2 for two-dimensional and axisymmetric problems and 3 for three-dimensional problems). The scalar pressure formulation yields unsymmetric coefficient matrices but involves a smaller number of variables which

would save considerable computer resources. For detailed information, see references [87-90].

The governing equations from linear acoustics are presented in the next section, followed by the acoustic finite element formulation and implementation. The emphasis is on the pressure formulation for the fluid media. The coefficient matrices are rendered symmetric by introducing a new potential variable [88]. The final finite element equations are solved by the explicit integration approach. Numerical examples include the prediction of wave profiles in both media and the Rayleigh wave interaction with a solid/fluid interface.

Governing Equations from Linear Acoustics

This treatment is based on the following linear acoustic assumptions [33]: (1) the fluid density varies only a small amount and the acoustic pressure is small compared with the equilibrium pressure; (2) the disturbances are small enough so that the convective effect is neglected; (3) the fluid is compressible and inviscous.

The acoustic pressure and density are related through the following linearized equation of state

$$p = B\left(\frac{\rho - \rho_o}{\rho_o}\right) \tag{5.1}$$

where p is the acoustic pressure which is defined as the difference of the total pressure and the equilibrium pressure; ρ and ρ_o are the acoustic and equilibrium fluid densities, respectively; B is the acoustic modulus and is defined as

$$B = \rho_o \frac{\partial p}{\partial \rho}\Big|_{\rho_o} \tag{5.2}$$

The particle velocity and acoustic density are related by the following continuity

equation via the conservation of mass

$$\nabla \cdot \mathbf{v} = \frac{1}{\rho}\frac{\partial \rho}{\partial t} \tag{5.3}$$

Note that ρ stands for ρ_O from now on. We have from the above equations

$$\nabla \cdot \mathbf{v} = -\frac{1}{B}\frac{\partial p}{\partial t} \tag{5.4}$$

By neglecting any body force, the application of Newton's second law and the Gaussian divergence theorem leads to the dynamic Euler equation,

$$\nabla p = -\rho\frac{\partial \mathbf{v}}{\partial t} \tag{5.5}$$

From Eqs. (5.4) and (5.5) we obtain the governing wave equation for pressure

$$\nabla^2 p = \frac{1}{c^2}\frac{\partial^2 p}{\partial t^2} \tag{5.6}$$

where $c = \sqrt{B/\rho}$ is the acoustic wave velocity. It follows from the equation of state that the acoustic density also satisfies the standard wave equation.

Similarly, the elimination of p from Eq. (5.4) and (5.5) yields the following governing wave equation for the particle velocity

$$\nabla^2 \mathbf{v} = \frac{1}{c^2}\ddot{\mathbf{v}} \tag{5.7}$$

Note that the derivation of the above equation (5.7) has utilized Eq. (2.51) and the following relation

$$\nabla \times \mathbf{v} = \mathbf{0} \tag{5.8}$$

which is a direct result of Eq. (5.5). By integrating Eq. (5.6) with respect to time, it is seen that the particle displacement also satisfies the vector wave equation, i.e.,

$$\nabla^2 \mathbf{u} = \frac{1}{c^2}\ddot{\mathbf{u}} \tag{5.9}$$

The boundary conditions for a fluid region can be specified by either the normal particle velocity or pressure. Without losing generality, assume that $S = S_v \cup S_p$, where $S_v \cap S_p = 0$. The conditions can be stated as follows [48].

$$\mathbf{v} \cdot \mathbf{n} = v_n^s, \quad \text{on } S_v \tag{5.10}$$

$$p = p^s, \quad \text{on } S_p \tag{5.11}$$

Specific boundary conditions can be briefly classified as follows. At a free surface, the pressure vanishes, i.e.,

$$p = 0 \tag{5.12}$$

At a rigid boundary the normal particle velocity is zero,

$$v_n = 0 \tag{5.13}$$

or

$$\frac{\partial p}{\partial n} = 0 \tag{5.14}$$

At the interface with an elastic solid, both normal pressure (or force) and normal velocity (or displacement) are continuous, and the tangential stress vanishes,

$$-p = \tau_n \tag{5.15}$$

$$-\frac{1}{\rho}\frac{\partial p}{\partial n} = \ddot{u}_n \tag{5.16}$$

$$\tau_s = 0 \tag{5.17}$$

where τ and $\mathbf{u}$ stand for the stress and displacement. Note that Eq. (5.16) is derived through taking the normal component of the Euler equation. At a radiation boundary, which resembles the truncation for a physically infinite medium, we assume that there

is only outgoing waves (no reflected waves). Based on D'Lambert's solution for the wave equation, we have

$$\frac{\partial p}{\partial n} = -\frac{1}{c}\dot{p} \tag{5.18}$$

Based on Eq. (5.7), a velocity potential ϕ can be introduced such that

$$\mathbf{v} = \nabla\phi \tag{5.19}$$

Then from Eq. (5.5) we have

$$p = -\rho\dot{\phi} \tag{5.20}$$

Substituting Eqs. (5.20) to Eq. (5.6) yields the wave equation for ϕ

$$\nabla^2\phi = \frac{1}{c^2}\ddot{\phi} \tag{5.21}$$

Substituting Eqs.(5.19-5.20) to (5.10-5.11) yields the following corresponding boundary conditions

$$\frac{\partial\phi}{\partial n} = v_n^s, \quad \text{on } S_v \tag{5.22}$$

$$-\rho\dot{\phi} = p^s, \quad \text{on } S_p \tag{5.23}$$

Acoustic Finite Element Formulation

Direct Galerkin weighted residual approach

The starting point is the acoustic wave equation for pressure in a compressible and inviscous fluid. For each element upon discretization we make the following approximation

$$p \approx \hat{p} = N_e^T P_e \tag{5.24}$$

where

$$N_e = \begin{bmatrix} N_1 & N_2 & \cdots & N_M \end{bmatrix}^T \tag{5.25}$$

$$P_e = \begin{bmatrix} P_1 & P_2 & \cdots & P_M \end{bmatrix}^T \tag{5.26}$$

and M is the number of nodes per element. Substitute the approximated pressure expression into the wave equation, we have the following residual term

$$\epsilon_e = \nabla^2 N_e^T P_e - \frac{1}{c^2} N_e^T \ddot{P}_e \tag{5.27}$$

The Galerkin weighted residual criterion requires that

$$\int_V N_e \left[\nabla^2 N_e^T P_e - \frac{1}{c^2} N_e^T \ddot{P}_e \right] dV = 0 \tag{5.28}$$

By using Green's first identity, i.e.,

$$\int_S \phi \nabla \psi \cdot d\mathbf{S} = \int_V \phi \nabla^2 \psi \, dV + \int_V \nabla \phi \cdot \nabla \psi \, dV \tag{5.29}$$

and noting that

$$\int_S \phi \nabla \psi \cdot d\mathbf{S} = \int_S \phi \nabla \psi \cdot \mathrm{n} \, dS = \int_S \phi \frac{\partial \psi}{\partial n} dS \tag{5.30}$$

the first term on the left hand side of Eq. (5.28) can be written as

$$\int_V N_e \nabla^2 N_e^T P_e \, dV = - \int_V \nabla N_e \cdot \nabla N_e^T P_e \, dV + \int_S N_e \frac{\partial N_e^T}{\partial n} P_e \, dS \tag{5.31}$$

Then Eq. (5.28) becomes

$$\int_V \frac{1}{c^2} N_e N_e^T \ddot{P}_e \, dV + \int_V \nabla N_e \cdot \nabla N_e^T P_e \, dV = \int_S N_e \frac{\partial N_e^T}{\partial n} P_e \, dS \tag{5.32}$$

which can be written in a more convenient form as follows

$$M_f^e \ddot{P}_e + K_f^e P_e = F_f^e \tag{5.33}$$

where the subscript f means fluid in distinction with solid, and

$$M_f^e = \int_V \frac{1}{c^2} N_e N_e^T \, dV \tag{5.34a}$$

$$K_f^e = \int_V \nabla N_e \cdot \nabla N_e^T \, dV \tag{5.34b}$$

$$F_f^e = \int_S N_e \frac{\partial p}{\partial n} \, dS \tag{5.34c}$$

By assembling the elementary matrices, i.e.,

$$M_f = \sum_e M_f^e, \quad K_f = \sum_e K_f^e, \quad F_f = \sum_e F_f^e \tag{5.35}$$

we obtain the global linear system of equations

$$M_f \ddot{P} + K_f P = F_f \tag{5.36}$$

For a fluid medium with viscous damping, the above equation can be extended by including a damping coefficient matrix D_f,

$$M_f \ddot{P} + D_f \dot{P} + K_f P = F_f \tag{5.37}$$

Pressure analog approach

By the pressure analog approach [87], the finite element model for the displacement field of a solid medium can be slightly modified for simulating the pressure field of a fluid medium. As a starting point, let

$$\mu = \rho c^2 \quad \lambda = -\rho c^2 \tag{5.38}$$

Eq. (2.50) reduces to the displacement wave equation Eq. (5.9) which in three dimensional Cartesian coordinates, can be expressed in terms of its components,

$$\nabla^2 u_i = \frac{1}{c^2} \ddot{u}_i \tag{5.39}$$

where $i = x, y, z$. By further assuming that any two components, say u_x and u_y, vanish,

$$u_x = u_y = 0 \tag{5.40}$$

the remaining equation for u_z is the same as the acoustic wave equation for pressure and therefore can be used as a dummy variable for the pressure denoted as U^p. In this approach, the forcing function and related boundary conditions need to be determined explicitly. The forcing forcing function under the pressure analog approach is associated with the z stress component T_z. That is, at a specific surface node a

$$F_f = \int N T_z dS = A T_z \Big|_a \tag{5.41}$$

where N is the shape function and A is the area associated with the node. It follows from Eq. (2.24) that

$$T_z = T_{iz} n_i = T_{xz} n_x + T_{yz} n_y + T_{zz} n_z \tag{5.42}$$

at a position with normal $\mathbf{n} = (n_x, n_y, n_z)$ pointing outward from the fluid surface. Based on Eqs. (2.33), (2.34), (2.46) and (2.48) with the incorporation of conditions Eq. (5.38), we have

$$T_{xz} = T_5 = \rho c^2 S_5 \tag{5.43a}$$

$$T_{yz} = T_4 = \rho c^2 S_4 \tag{5.43b}$$

$$T_{zz} = T_3 = \rho c^2 (S_3 - S_2 - S_1) \tag{5.43c}$$

Based on Eq. (2.15) we have

$$S_1 = \frac{\partial u_x}{\partial x}, \quad S_2 = \frac{\partial u_y}{\partial y}, \quad S_3 = \frac{\partial u_z}{\partial z} \tag{5.44a}$$

$$S_4 = \frac{\partial u_z}{\partial y} + \frac{\partial u_y}{\partial z}, \quad S_5 = \frac{\partial u_z}{\partial x} + \frac{\partial u_x}{\partial z} \tag{5.44b}$$

Incorporating conditions Eq. (5.40) and replacing u_z with U^p gives

$$S_1 = S_2 = 0, \quad S_3 = \frac{\partial U^p}{\partial z}, \quad S_4 = \frac{\partial U^p}{\partial y}, \quad S_5 = \frac{\partial U^p}{\partial x} \tag{5.45}$$

Substituting Eq. (5.45) to (5.43) and (5.43) to (5.42) yields

$$T_z = \rho c^2 \left(\frac{\partial U^p}{\partial x} n_x + \frac{\partial U^p}{\partial y} n_y + \frac{\partial U^p}{\partial z} n_z \right) = \rho c^2 \nabla U^p \cdot \mathbf{n} = \rho c^2 \frac{\partial U^p}{\partial n} \tag{5.46}$$

For an external or interfacing velocity $\mathbf{V} = \dot{\mathbf{U}}$, where $\mathbf{U}$ is the displacement vector, the continuity in the normal particle acceleration indicates that

$$\dot{\mathbf{V}} \cdot \mathbf{n} = \dot{\mathbf{v}} \cdot \mathbf{n} \tag{5.47}$$

where n is defined as before. Using the Euler equation, we have

$$\rho \dot{\mathbf{V}} \cdot \mathbf{n} = -\nabla p \cdot \mathbf{n} = -\frac{\partial p}{\partial n} \tag{5.48}$$

Substituting the above relation into Eq. (5.46) by noting that $p = U^p$ gives

$$T_z = -(\rho c)^2 \dot{\mathbf{V}} \cdot \mathbf{n} \tag{5.49}$$

Now by defining $\mathbf{n}$ as the unit normal pointing towards the fluid from the interface which is the opposite to the former definition, we obtain

$$T_z = (\rho c)^2 \dot{\mathbf{V}} \cdot \mathbf{n} = (\rho c)^2 \dot{V}_n = (\rho c)^2 \ddot{U}_n \tag{5.50}$$

It is seen that the z component of the surface traction becomes the product of the fluid bulk modulus and the normal derivative of pressure, and is further proportional to the time derivative of the normal surface velocity. The corresponding force term is

$$F_f^v = A(\rho c)^2 \dot{V}_n = A(\rho c)^2 \ddot{U}_n \tag{5.51}$$

For a rigid boundary, Eq. (5.51) indicates that

$$F^{rb} = 0 \tag{5.52}$$

For a free boundary, the zero pressure implies that

$$U^p = 0 \tag{5.53}$$

An absorbing boundary condition for the radiation problem is as follows,

$$F^b = A\rho c(-cos\theta)\dot{U}^p \tag{5.54}$$

where θ is the incident angle. Then the system of finite element equations assume the following form,

$$M_f\ddot{U}^p + K_f U^p = F^v + F^b \tag{5.55}$$

or

$$M_f\ddot{U}^p + D_f\dot{U}^p + K_f U^p = F_f \tag{5.56}$$

where $F_f = F^v$, and the damping term corresponds to the absorbing boundary force.

A 2D problem results from a 3D problem when one dimension, say the y direction, is infinite. Under this condition, the above results are still valid with the notation that the y component of each quantity vanishes.

For axisymmetric conditions, Eq. (5.39) is expressed as

$$\nabla^2 u_r - \frac{1}{r^2}u_r = \frac{1}{c^2}\ddot{u}_r \tag{5.57a}$$

$$\nabla^2 u_z = \frac{1}{c^2}\ddot{u}_z \tag{5.57b}$$

With a further constraint that

$$u_r = 0 \tag{5.58}$$

Eq. (5.57) reduces to the standard acoustic wave equation for pressure and u_z becomes the dummy variable for pressure fields denoted as U^p. The forcing function under the axisymmetric condition can be determined in a similar manner as for the case in 3D Cartesian coordinates. The z stress component is

$$T_z = T_{rz} n_r + T_{zz} n_z \tag{5.59}$$

at a position with normal $\mathbf{n} = (n_r, n_z)$ pointing outward from the fluid surface. Based on Eqs. (3.51) and (3.52) with incorporation of conditions Eq. (5.38), we have

$$T_{rz} = 2\rho c^2 S_{rz} \tag{5.60a}$$

$$T_{zz} = \rho c^2(-S_{rr} + S_{zz} - S_{\theta\theta}) \tag{5.60b}$$

Based on Eqs. (3.54) and (3.55) with incorporation of conditions Eq. (5.58), we have

$$S_{rz} = \frac{1}{2}\frac{\partial u_z^p}{\partial r}, \quad S_{zz} = \frac{\partial u_z^p}{\partial z}, \quad S_{rr} = S_{\theta\theta} = 0 \tag{5.61}$$

Substituting Eq. (5.61) to (5.60) and (5.60) to (5.59) yields

$$T_z = \rho c^2 \left(\frac{\partial u_z^p}{\partial r} n_r + \frac{\partial u_z^p}{\partial z} n_z \right) = \rho c^2 \nabla u_z^p \cdot \mathbf{n} = \rho c^2 \frac{\partial u_z^p}{\partial n} \tag{5.62}$$

For an external or interfacing velocity $\mathbf{V} = \dot{\mathbf{U}}$, a similar procedure as for the 3D coordinates yields

$$T_z = (\rho c)^2 \ddot{\mathbf{U}} \cdot \mathbf{n} = (\rho c)^2 \ddot{U}_n \tag{5.63}$$

where $\mathbf{n}$ has been defined as the unit normal pointing towards the fluid from the interface. The forcing function is in the form of Eq. (5.51). For the rigid, free and absorbing boundaries, Eqs. (5.52-5.54) are still applicable. The final system of equations take the same form as Eq. (5.55) or (5.56). On the axis of symmetry, the radial derivative of U^p should vanish due to the axisymmetric condition.

Mock fluid elements

The mock fluid element is virtually the finite element for elastic solids developed in the previous chapters with alteration of material parameters such that the property of the solid reduces to that of the fluid. By assuming

$$\mu = 0, \quad \lambda = \rho c^2 \tag{5.64}$$

Eq. (2.50) reduces to Eq. (5.9) with the following constraint

$$\nabla \times \mathbf{u} = 0 \tag{5.65}$$

With this approach, the pressure and the displacement are related as follows,

$$p = -\lambda \nabla \cdot \mathbf{u} \tag{5.66}$$

As an alternative approach for converting the solid displacement equation to the fluid counterpart, we can assume that

$$\mu = \rho c^2 \quad \lambda = -\rho c^2 \tag{5.67}$$

The boundary condition at the interface with a solid material requires continuity for the normal displacement component and discontinuity for the tangential component. The normal approach to achieve this boundary condition is to use a double set of nodes across the interface. Every pair of nodes occupies the same physical location on the interface but represents the fluid and solid respectively. If only one set of nodes is used on the interface, i.e., both the normal and tangential displacement components are assumed to be continuous, the resulting solution does not have significant variation, as reported by Kalinowski [89].

As a simple numerical example, the wave fields of a line source over a fluid region of 1.6×0.8 cm^2 are computed. The excitation pulse is a raised cosine function f_o=2 MHz. The discretization size is 20 μm and the time step is 7.5 ns. Fig. 5.1 shows the transient pressure field obtained by the pressure analog method, and Fig. 5.2 displays the displacement fields (y and x components) based on the displacement formulation. Both the figures are recorded at t=4.5 μs. Shown in Fig. 5.3 are the field patterns for the displacement fields, where the inner circle is for the y-displacement and the two half-circles are for the x-displacement. The outer half-circle indicates the total displacement which is constant over the angle range similar to the pressure field.

Fluid/Solid Coupling

This section is based on the pressure analog approach described in the last section. At the solid/fluid interface, the force applied to the fluid is $-pA$ while the force exerted on the fluid from the solid is $A(\rho c)^2\ddot{U}_n$, the coupled equation is as follows

$$\begin{bmatrix} M & 0 \\ -(\rho c)^2 A^T & M_f \end{bmatrix} \begin{Bmatrix} \ddot{U} \\ \ddot{p} \end{Bmatrix} + \begin{bmatrix} D & 0 \\ 0 & D_f \end{bmatrix} \begin{Bmatrix} \dot{U} \\ \dot{p} \end{Bmatrix} + \begin{bmatrix} K & A \\ 0 & K_f \end{bmatrix} \begin{Bmatrix} U \\ p \end{Bmatrix} = \begin{Bmatrix} F \\ F_f \end{Bmatrix} \tag{5.68}$$

where $F_f = A\rho c^2 \frac{\partial p}{\partial n}$. It is seen that the coefficient matrices are unsymmetric and cause inconvenience for the solution. This problem, which is the major disadvantage of the pressure formulation for the fluid medium, can be removed by replacing the

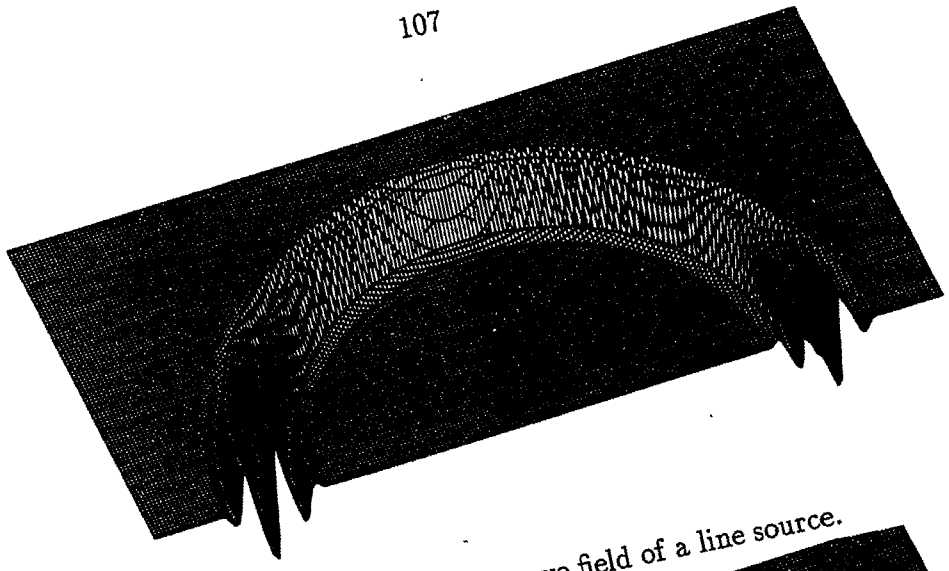

Figure 5.1: Pressure wave field of a line source.

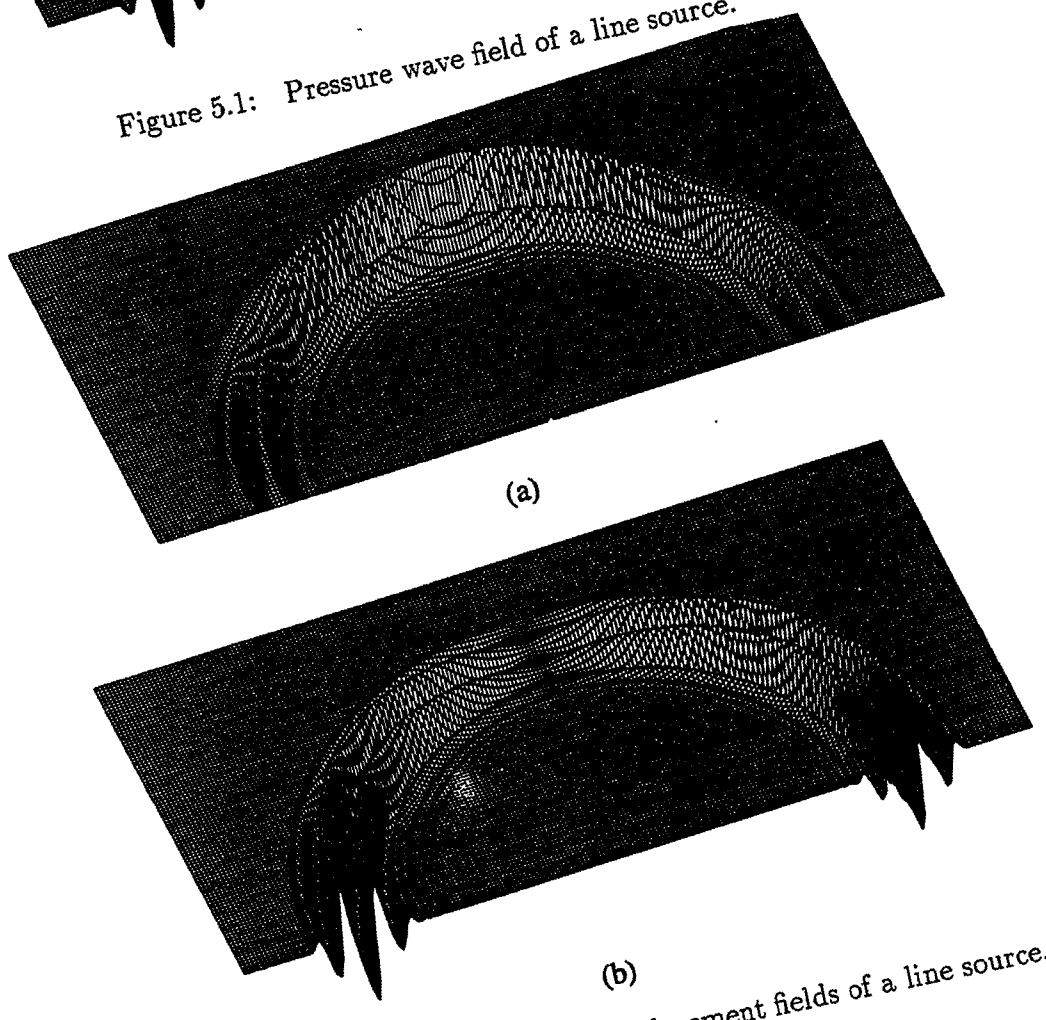

Figure 5.2: (a) Y- and (b) X-displacement fields of a line source.

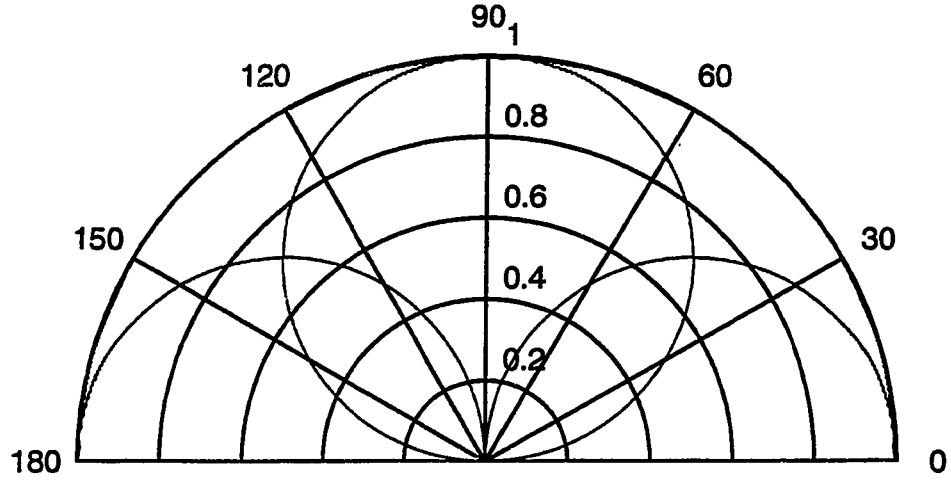

Figure 5.3: Displacement field patterns for a line source.

pressure by a potential variable through the following procedure. Let

$$p = -\dot{q} \tag{5.69}$$

it follows that

$$\begin{bmatrix} M & 0 \\ 0 & M_f \end{bmatrix} \begin{Bmatrix} \ddot{U} \\ \ddot{q} \end{Bmatrix} + \begin{bmatrix} D & -A \\ (\rho c)^2 A^T & D_f \end{bmatrix} \begin{Bmatrix} \dot{U} \\ \dot{q} \end{Bmatrix} + \begin{bmatrix} K & 0 \\ 0 & K_f \end{bmatrix} \begin{Bmatrix} U \\ q \end{Bmatrix} = \begin{Bmatrix} F \\ G \end{Bmatrix} \tag{5.70}$$

where

$$G = -\int_0^t F_f dt \tag{5.71}$$

Neglecting viscous damping in both the fluid and solid media, we obtain

$$\begin{bmatrix} M & 0 \\ 0 & M_f \end{bmatrix} \begin{Bmatrix} \ddot{U} \\ \ddot{q} \end{Bmatrix} + \begin{bmatrix} 0 & -A \\ (\rho c)^2 A^T & 0 \end{bmatrix} \begin{Bmatrix} \dot{U} \\ \dot{q} \end{Bmatrix}$$

$$+\begin{bmatrix} K & 0 \\ 0 & K_f \end{bmatrix}\begin{Bmatrix} U \\ q \end{Bmatrix} = \begin{Bmatrix} F \\ G \end{Bmatrix} \tag{5.72}$$

In a more compact form, we can write

$$M\ddot{U}^q + D\dot{U}^q + KU^q = F^q \tag{5.73}$$

The set of linear equations derived above is solved by the explicit central difference scheme. The stability condition is such that the the fastest wave should propagate less than one spatial element in one time step.

Numerical Examples of Transient Wave Phenomena at Solid/Fluid Interfaces with Axisymmetric Geometries

The basic axisymmetric geometry shown in Fig. 5.4 is modeled using the finite element procedure presented above. The fluid and solid media are taken as water and aluminum respectively and their mechanical properties are indicated in the figure. A raised cosine function with a center frequency of 5 MHz is used as the driving signal, while the source location and structure are varied for a few cases. In each case the source is also symmetric about the z-axis.

As the first case, we assume a point source inside the solid medium 0.2 cm from the interface. The driving force of the source is along the axial direction. The wave profiles at different time instants are shown in Fig. 5.5. Note from now on that in each profile plot the solid side is represented by the z-displacement while the fluid side is represented by the potential which is normalized such that the magnitude is on the same order as the z-displacement in the solid. Fig. 5.5(a) indicates that the reflection and refraction of the longitudinal wave front have occurred at the interface

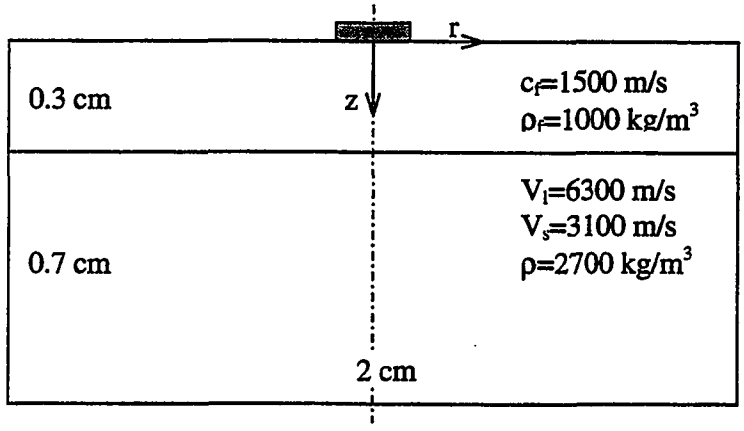

Figure 5.4: Axisymmetric geometry with a fluid/solid interface.

and the shear wave front from the source has reached the interface. In Fig. 5.5(b) the reflection and refraction of the shear wave as well as the reflection of the longitudinal wave from the back surface are shown. Each reflection associated with the solid medium is accompanied by a mode conversion. Fig. 5.5(c) records the various wave fronts at a later time. As a second case, we consider a point-like source, i.e., a small finite aperture, on the front surface of the fluid medium. The aperture diameter is 2a=0.01 cm, which corresponds to ka=$\pi/3$. The wave profiles at three different time instants are shown in Fig. 5.6. It can been seen that after the longitudinal wave front reaches the interface, both reflection and refraction occur. Among the refracted waves, we can identify the longitudinal, shear, head and interface Rayleigh waves. A further point to note is that as the interface Rayleigh wave propagates, it radiates (or leaks) waves (at the Rayleigh angle) back to the fluid medium. By examining the time dependent signals at points along the interface, the interface Rayleigh velocity

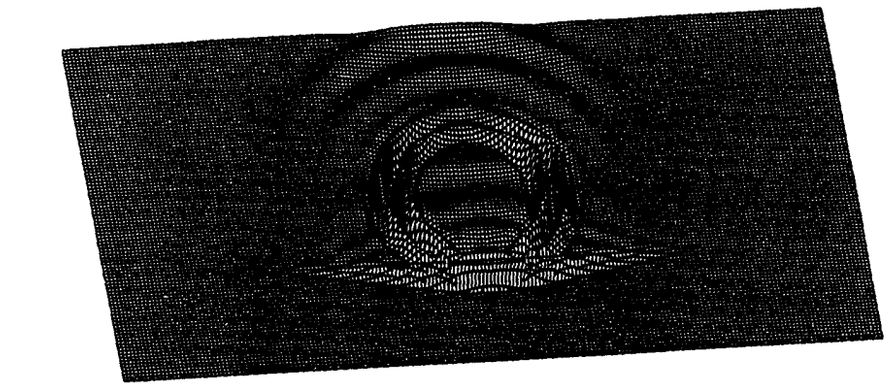

(a)

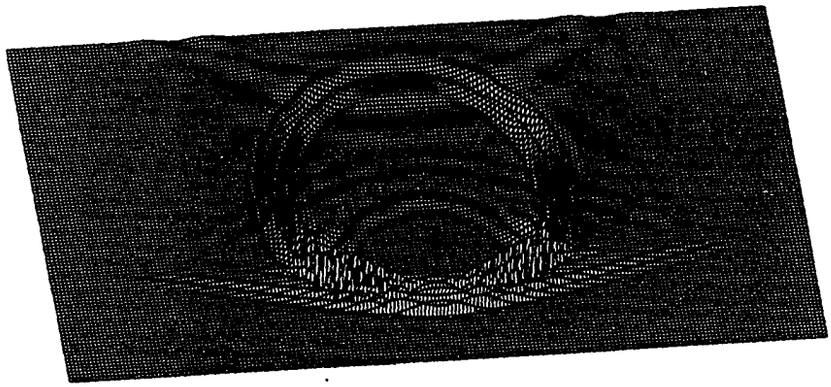

(b)

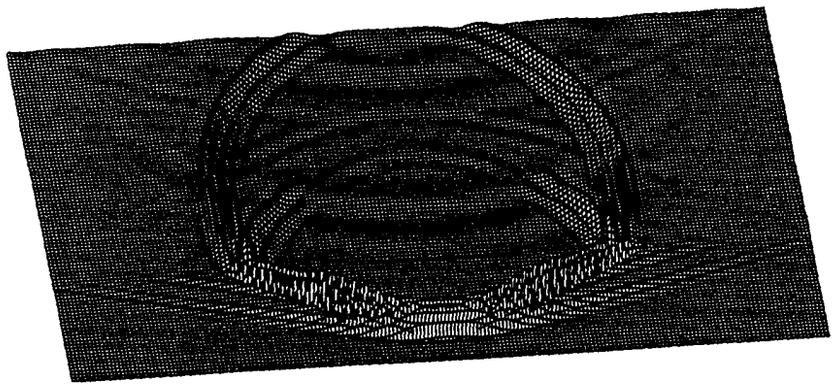

(c)

Figure 5.5: Wave profiles for a point source inside the solid medium, (a) t=1 μs, (b) t=1.5 μs, and (c)t=2 μs.

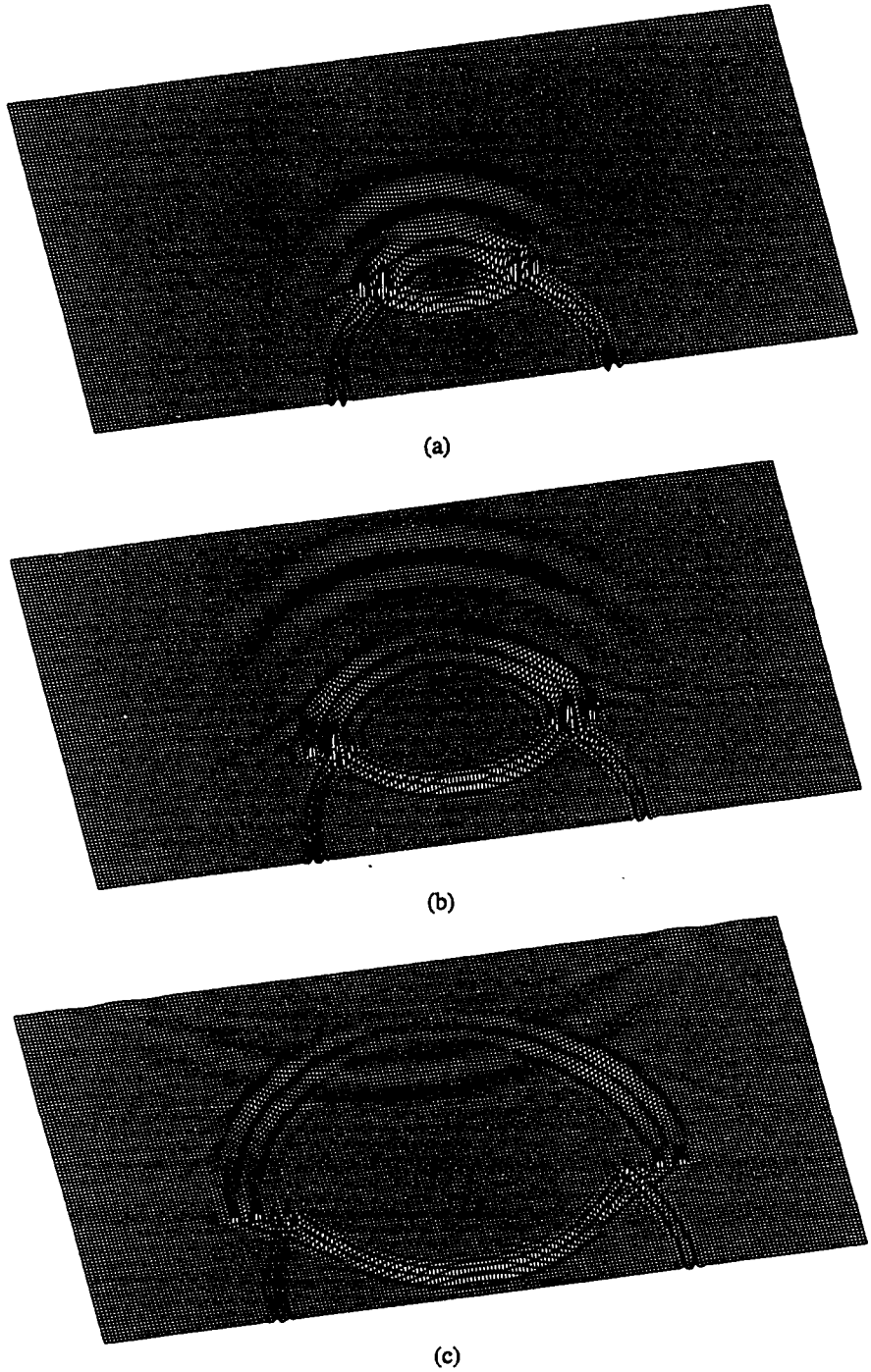

Figure 5.6: Wave profiles for a point-like source on the fluid surface, (a) t=2.75 μs, (b) t=3.25 μs, and (c)t=4 μs.

is estimated to be V_R=2940 m/s, which is slightly greater than the corresponding Rayleigh wave velocity on a traction free surface.

As a third case, assume a spherically focused wave from an aperture with diameter of 1.5 cm and focal length of 2 cm. The wave profiles are shown in Fig. 5.7. From Fig. 5.7(a) we see the reflected longitudinal wave and the refracted shear wave. At that time instant a longitudinal wave has not been refracted into the solid medium. This is expected as the maximum angle of incidence is between the critical angles for longitudinal and shear waves ($\theta_{\max}$=20.56, θ_l=13.77, θ_s=28.94 degs). An interface Rayleigh wave does not exist as the incident angle is always smaller than the critical Rayleigh angle which is estimated to be θ_R=30.66 deg. As the incident wave proceeds as shown in Figs. 5.7(b) and (c), the incident angle becomes smaller and then a focused longitudinal wave is transmitted into the solid medium. It is defocused after passing the focal point. As a final case, consider a spherically focused wave similar to the previous wave except that the focal length is 1 cm. The corresponding wave profiles are shown in Fig. 5.8. An essential difference is that the maximum angle of incidence ($\theta_{\max}$=36.87 deg) is greater than all the three critical angles. As the incident wave proceeds, the interface Rayleigh wave, shear wave, longitudinal wave and head wave gradually appear. The head wave on the fluid side radiated from the interface Rayleigh wave is clearly indicated especially when the interface wave passes through the axis of symmetry.

In summary, the results indicate that an interface Rayleigh wave is generated when an incident wave from the fluid medium matches the critical Rayleigh angle, and a propagating interface Rayleigh wave radiates waves back into the fluid medium. Although only planar interfaces are considered here, the extension to arbitrarily curved

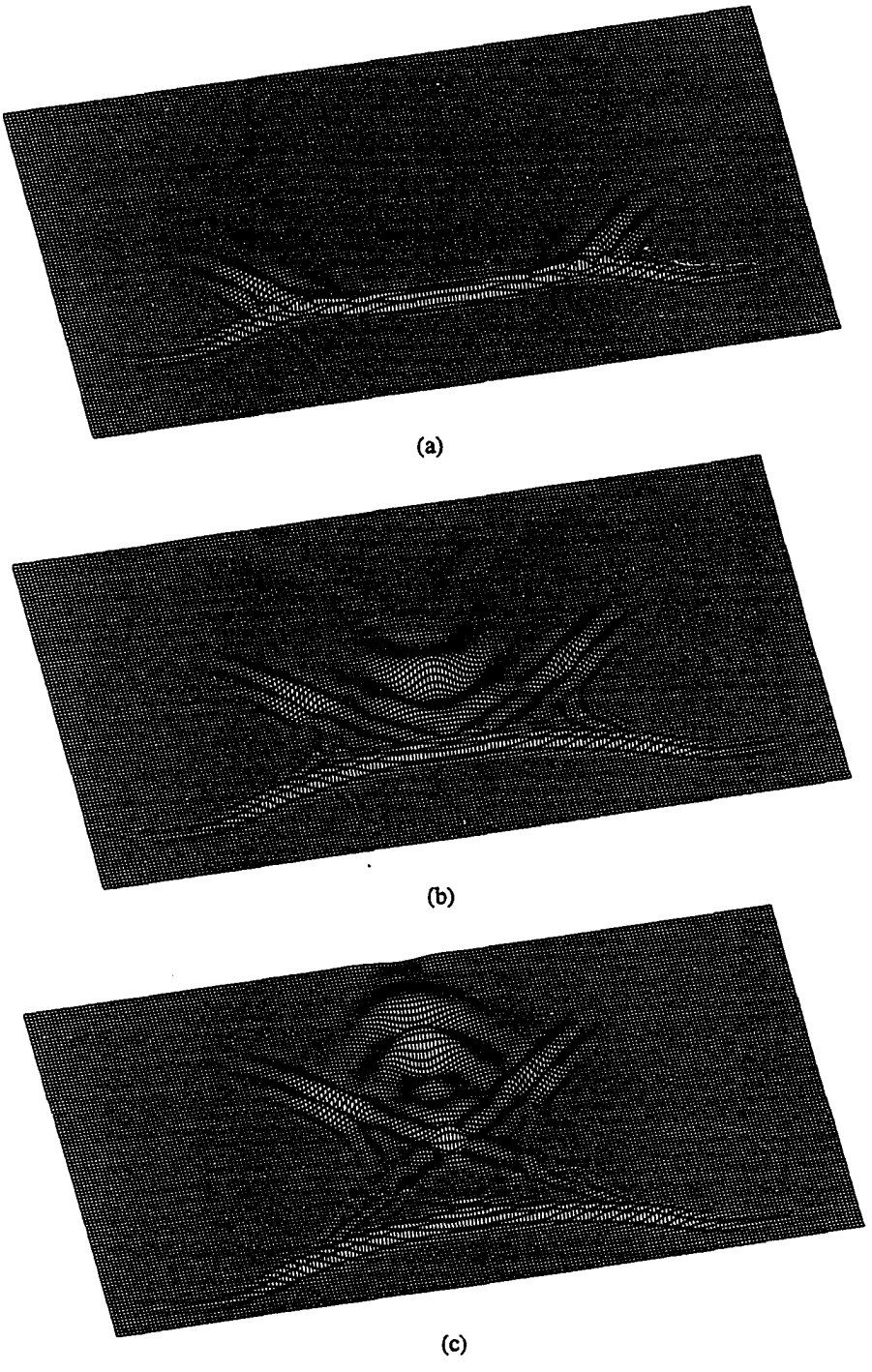

Figure 5.7: Wave profiles for a spherically focused wave from the fluid medium to the solid medium, $\theta_{\max} < \theta_{\mathrm{R}}$, (a) t=3 μs, (b) t=3.5 μs, and (c)t=4 μs.

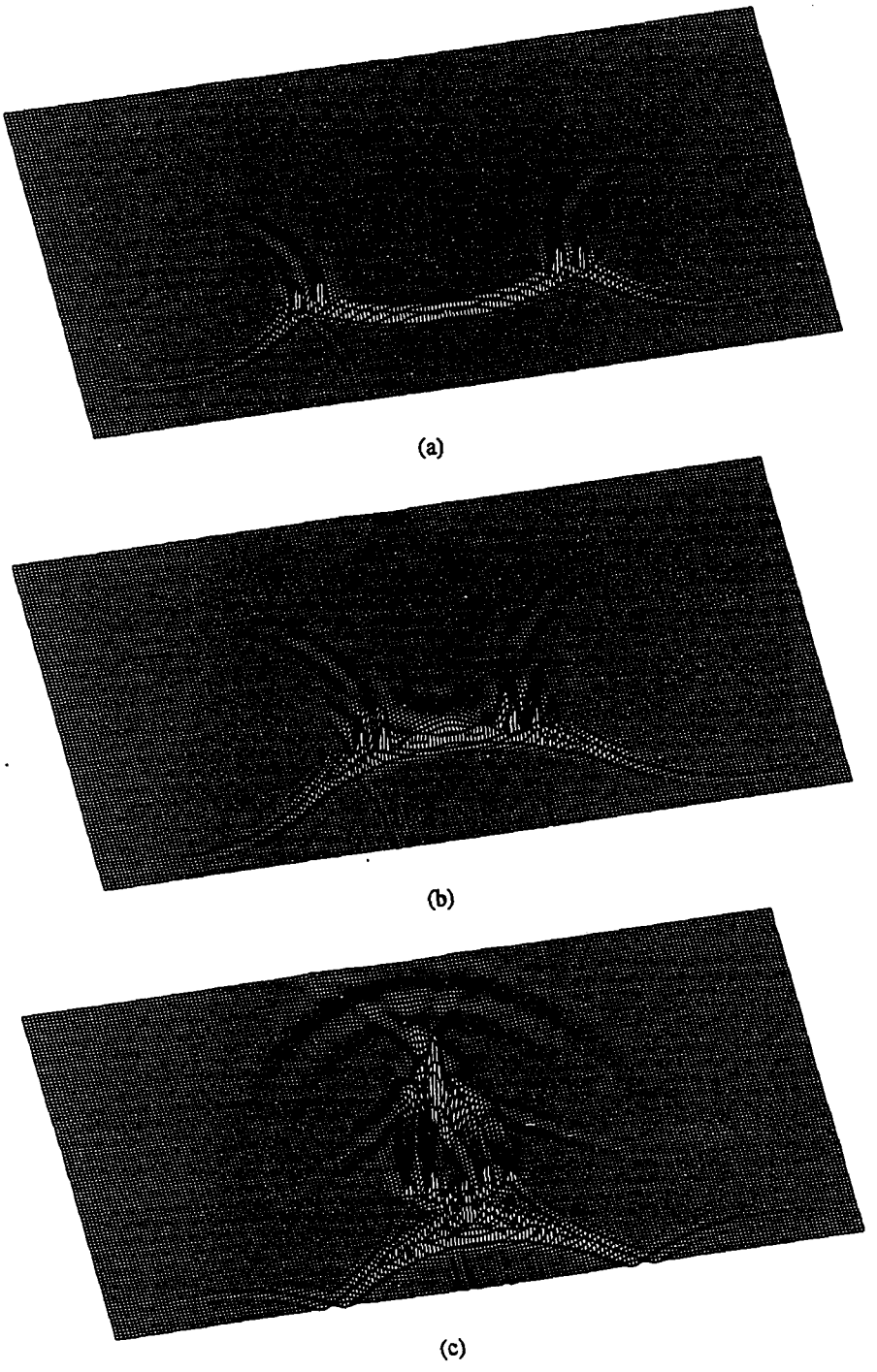

Figure 5.8: Wave profiles for a spherically focused wave from the fluid medium to the solid medium, $\theta_{\max} > \theta_{\mathrm{R}}$, (a) t=3.5 μs, (b) t=4 μs, and (c)t=5 μs.

interfaces is trivial for the finite element method with the expense of some extra computer resources.

Simulation of Leaky Rayleigh Waves with 2D Geometries

The Rayleigh and leaky Rayleigh waves have been an effective means for surface and subsurface defect detection and characterization. The propagation of Rayleigh waves is largely confined at the free surface and decays dramatically from the surface deeper into the bulk medium. At a fluid/solid interface, the Rayleigh wave is known as the leaky Rayleigh wave because of the attenuation of its amplitude during propagation as a result of continuous radiation (leaking) back into the fluid medium. A theoretical account of the leaky wave phenomenon has been given by Bertoni and Tamir [91]. Comparison of experimental and theoretical results based on a Gaussian beam incident at the Rayleigh angle are given by Breazeale et al. [92]. Application of the leaky Rayleigh wave for NDE is described by Adler and Scott [93]. Based on the ray-optical approach, Parmon and Bertoni [94] have interpreted the acoustic material signature (AMS) using the Leaky Rayleigh wave as a coherent wave component. Time domain measurements of leaky Rayleigh wave velocity and attenuation have been reported by Yamanaka [95].

In this section, the finite element approach is used for modeling the combination of a fluid medium and an isotropic solid medium in contact. The leaky Rayleigh wave and its scattering from subsurface cracks are predicted. This investigation is based on the two-dimensional approximation to model a reasonable size under limited computer resources. The validation and comparison of the finite element method with analytical and other numerical approaches for acoustic and elastic media have been

reported in previous papers [37,39,41].

The basic two-dimensional geometries are shown in Fig. 5.9. The fluid and solid media are taken as water (c=1500 m/s, ρ=1000 kg/m^3) and aluminum (V_l=6300 m/s, V_S=3100 m/s, ρ=2700 kg/m^3) respectively. A raised cosine function with a center frequency of 5 MHz and bandwidth of 6 MHz is used as the driving signal, while the source location and structure are varied for the different configurations in Fig. 5.9(a), (b) and (c). The region (or the half of the whole region for symmetric cases) of 1 cm^2 is discretized into 500×500 square elements. A typical run takes one to three hours depending on the number of time steps involved on a DEC alpha workstation.

Case 1

As the first case we refer to Fig. 5.9(a). The left vertical boundary is a symmetric boundary and a line source is applied on the solid surface in the plane of symmetry. The driving force of the source is along the vertical (Y) direction. A non-reflective boundary condition [15] is applied at the bottom boundary. That is, two boundary value problems (BVP) are solved with different boundary conditions at that boundary. BVP1: $u_y = 0$, $\frac{\partial u_x}{\partial y} = 0$; BVP2: $u_x = 0$, $\frac{\partial u_y}{\partial y} = 0$. The average of the two sets of solutions cancels the reflections from that boundary. In order to cancel the multi-reflections at a 2D corner, four boundary value problems would have to be solved. The wave profiles at different time instants are shown in Fig. 5.10. Note from now on that in each profile plot the solid side is represented by the y-displacement while the fluid side by the potential which is normalized such that the magnitude is of the same order as the y-displacement in the solid. The line source excites a longitudinal

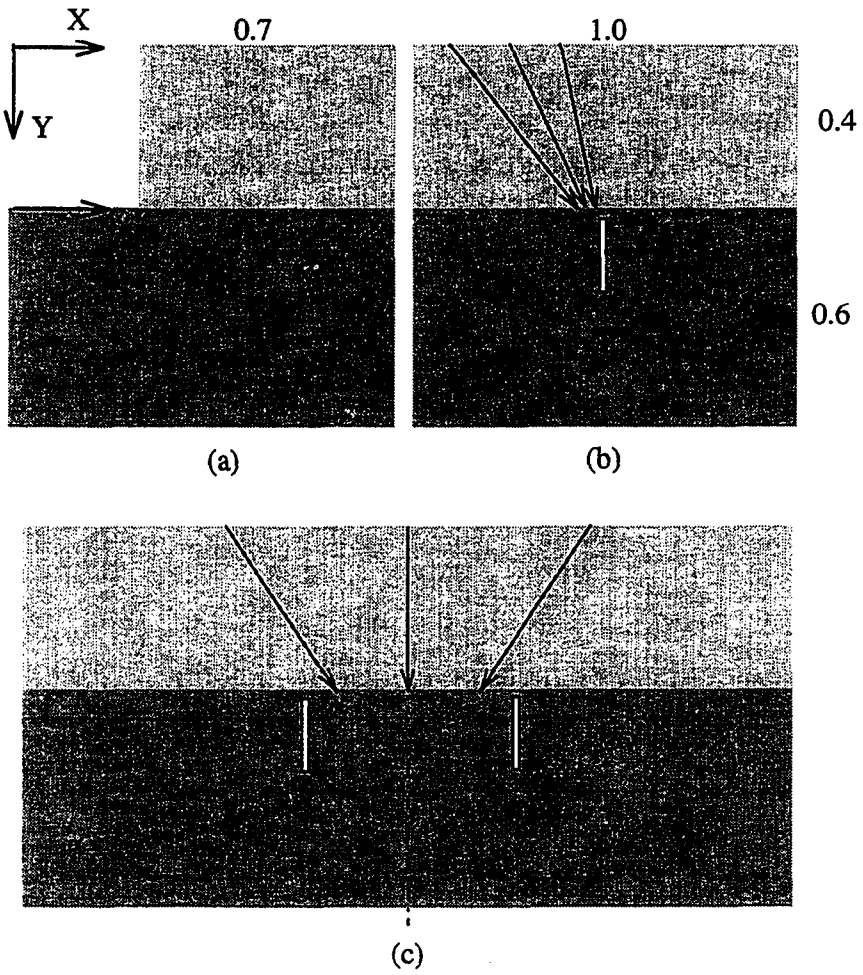

Figure 5.9: Two dimensional geometries involving fluid/solid interfaces where leaky Rayleigh waves can be excited. The dimensions are in centimeters.

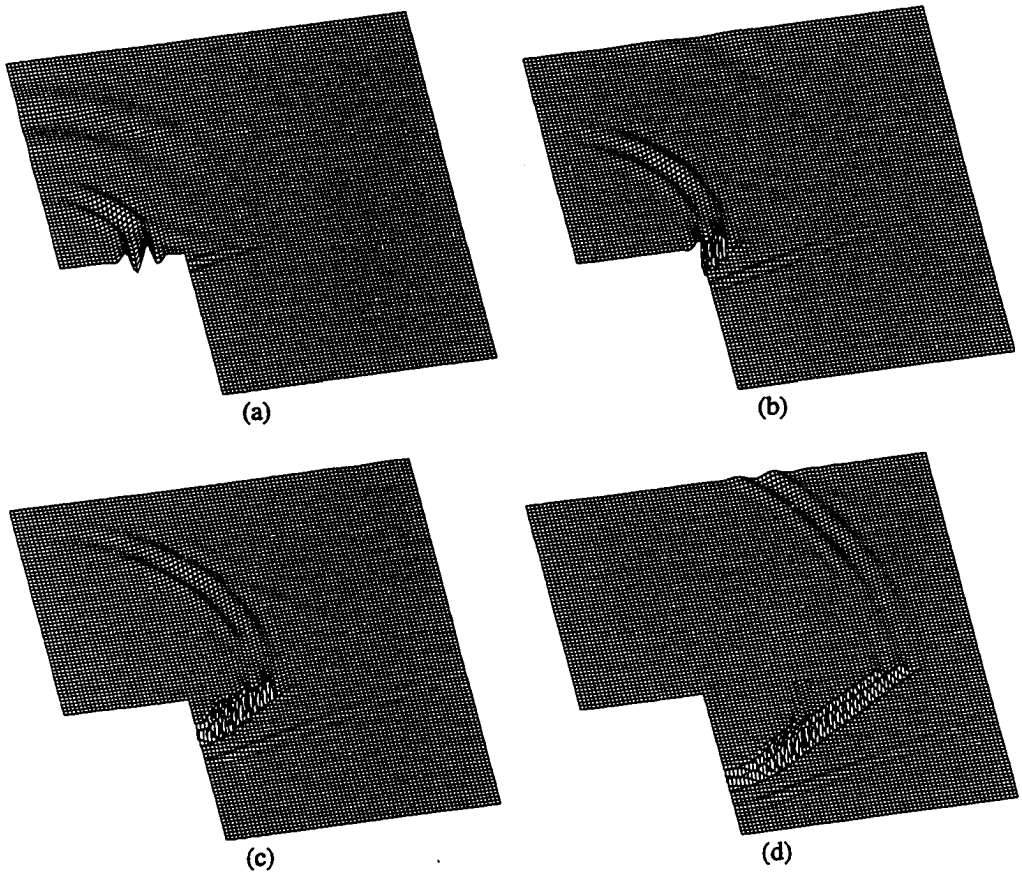

Figure 5.10: Wave profiles corresponding to geometry Fig. 5.9(a), (a) t=1 (b) 1.5 (c) 2 and (d) 3 microseconds.

wave, a head wave and a shear wave in the bulk solid medium and a Rayleigh wave along the surface. As the Rayleigh wave reaches the interface, a leaky Rayleigh wave is excited along the interface and an associated wave front propagates into the fluid region at the Rayleigh angle. A secondary fact is that the head/longitudinal wave close to the interface also excites a wave component propagating into the fluid at the longitudinal critical angle. The time dependent y-displacement components of the Rayleigh/leaky Rayleigh wave along the solid surface/interface are shown in Fig. 5.11 from which the Rayleigh wave velocity is determined to be V_R=2950 m/s. The corresponding maximum amplitude is shown in Fig. 5.12 where the attenuation of the leaky Rayleigh wave is demonstrated.

Case 2

This case corresponds to Fig. 5.9(b). A strip source with width w=0.3 cm centered at x=0.2 cm, focuses the incident beam to the interface at location x=0.437 cm . With this configuration, the center ray is at the calculated Rayleigh angle (30.6 deg.). The focusing effect is achieved by appropriate time delays at different source lines. The forcing function is assumed uniform over the source. In addition to a non-reflective boundary condition on the bottom boundary, similar conditions are also put on the two side boundaries. Though only two BVPs are solved, no multi-reflections at the corners are observed for the time period of interest. Wave fronts at different time instants are shown in Fig. 5.13. The figures refer to the defect free case unless otherwise indicated. Figs. 5.14 (a) and (b) show the maximum amplitude profiles within the fluid region without and with the subsurface crack respectively. The crack is 1.2×10^{-2}cm in thickness and 0.2 cm in depth and located at x=0.5 cm

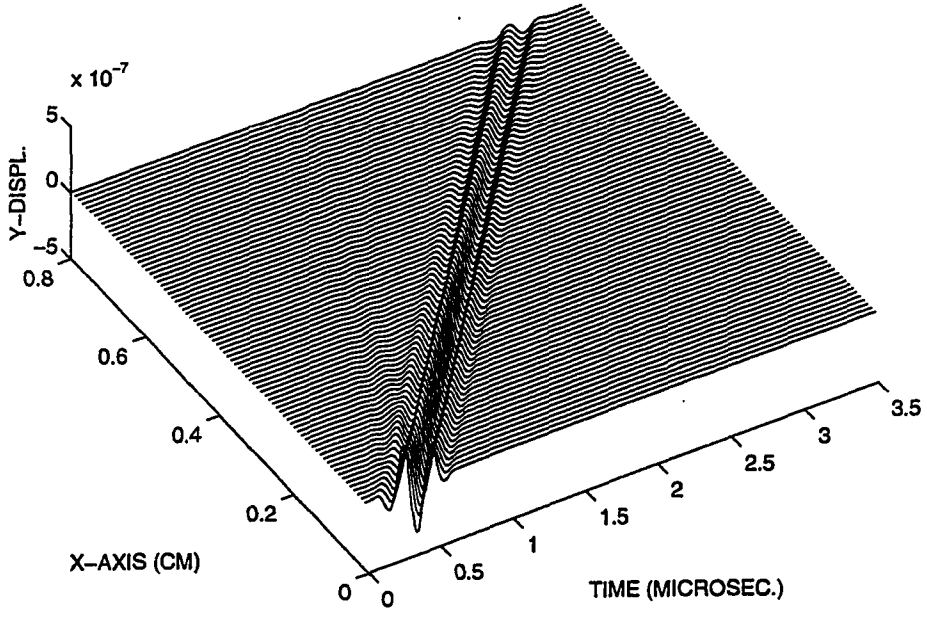

Figure 5.11: Transient vertical (Y) displacement waveforms at points along the interface.

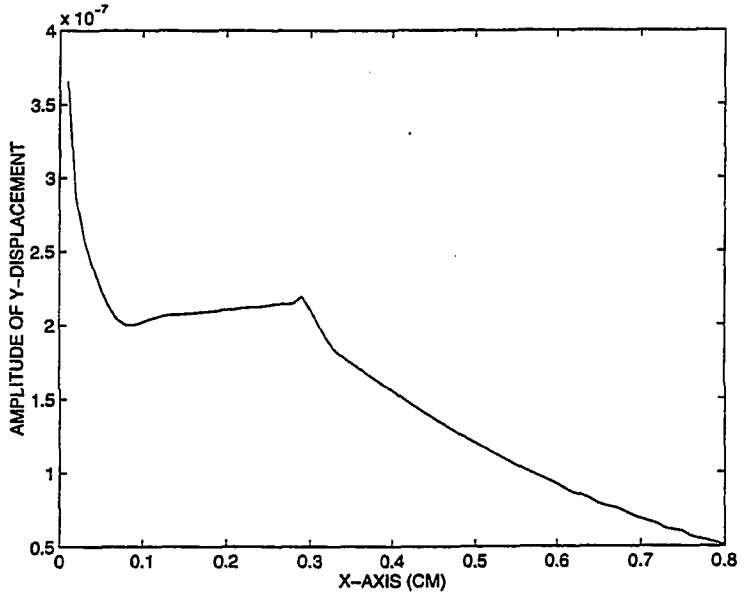

Figure 5.12: Maximum amplitude based on Fig. 5.11.

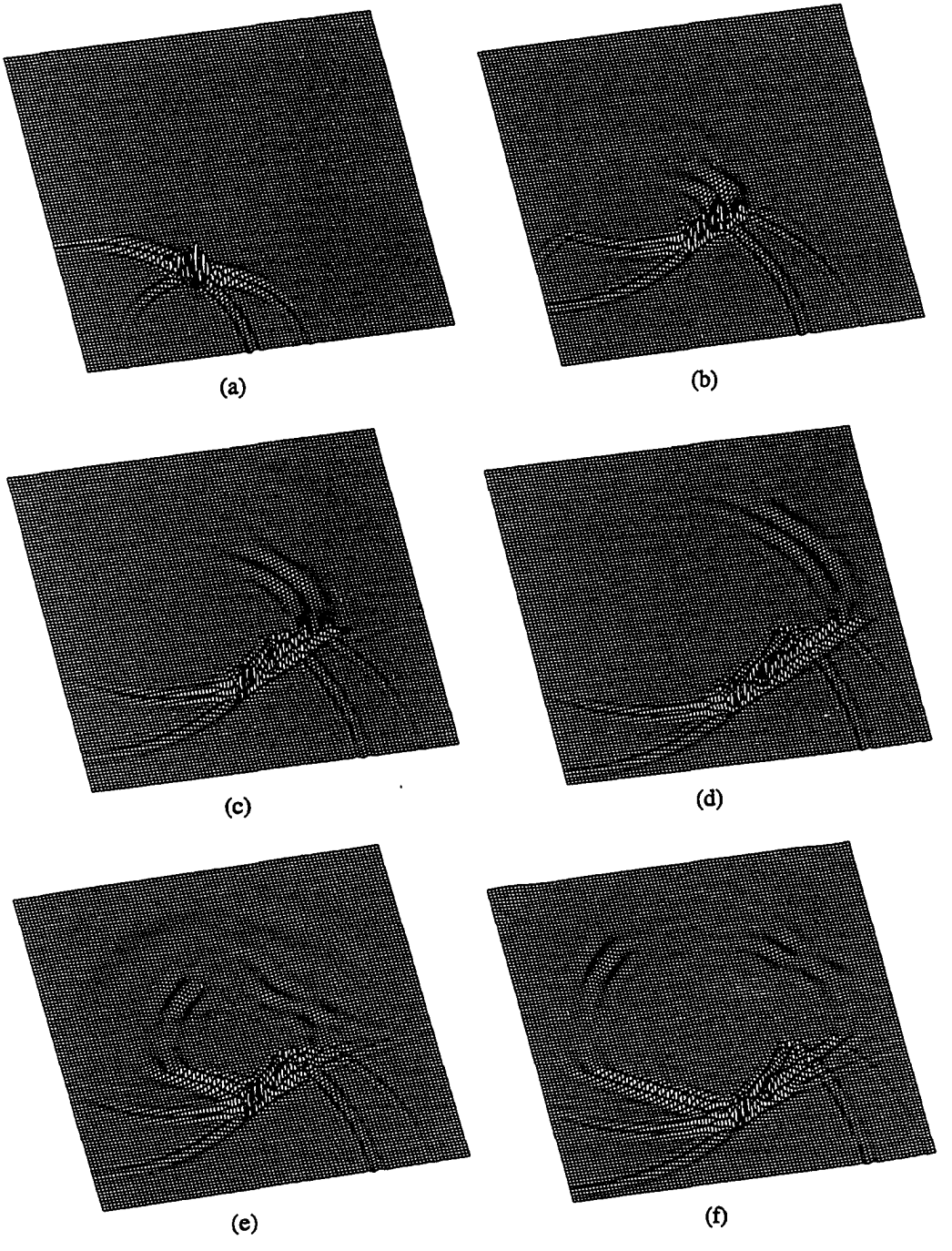

Figure 5.13: Wave profiles corresponding to geometry Fig. 5.9(b), (a) t=3 (b) 4.5 (c) 5 (d) 5.5 microseconds (without crack) and (e) 5, (f) 5.5 microseconds (with crack).

and 1.2×10^{-2}cm from the solid surface. In order to study the bandwidth influence on the reflected beams, two additional pulses with bandwidth of 3.6 and 2.6 MHz but of the same center frequency as the original pulse are examined. The amplitude profiles in the fluid medium are shown in Figs. 14 (c) and (d). The amplitude profiles in Fig. 5.14 along y=0.2 cm in the fluid are shown in Fig. 5.15. It is seen that the interaction of the incident beam with the interface generates a specularly reflected beam, a spatially displaced beam and a trailing plane wave. The latter is due to a leaky Rayleigh wave propagating along the interface. The shift between the two reflected beams is observed to be about 0.1 cm on the interface which is independent of the excitation bandwidth. Note that for a narrow bandwidth pulse there exists a reflected secondary beam (sidelobe) besides the two major beams. The results are consistent with the theoretical predictions in the literature [90-92]. The effect of a subsurface crack is the partial reflection of the leaky Rayleigh wave. The forward leaky Rayleigh wave is significantly attenuated and the reflected one also leaks energy back to the fluid medium as displayed clearly in Fig. 5.13(e) and (f). In addition, it can be seen that the displaced beam forms an angle with the specularly reflected beam. This is due to the focused incident beam. While the specularly reflected beam stays the same, the spatially displaced beam increases its amplitude with the decrease of bandwidth. The appearance of the subsurface crack decreases the amplitude of the displaced beam. For each situation (bandwidth), while the displaced beam is relatively constant, the specularly reflected beam decreases in magnitude farther away from the interface.

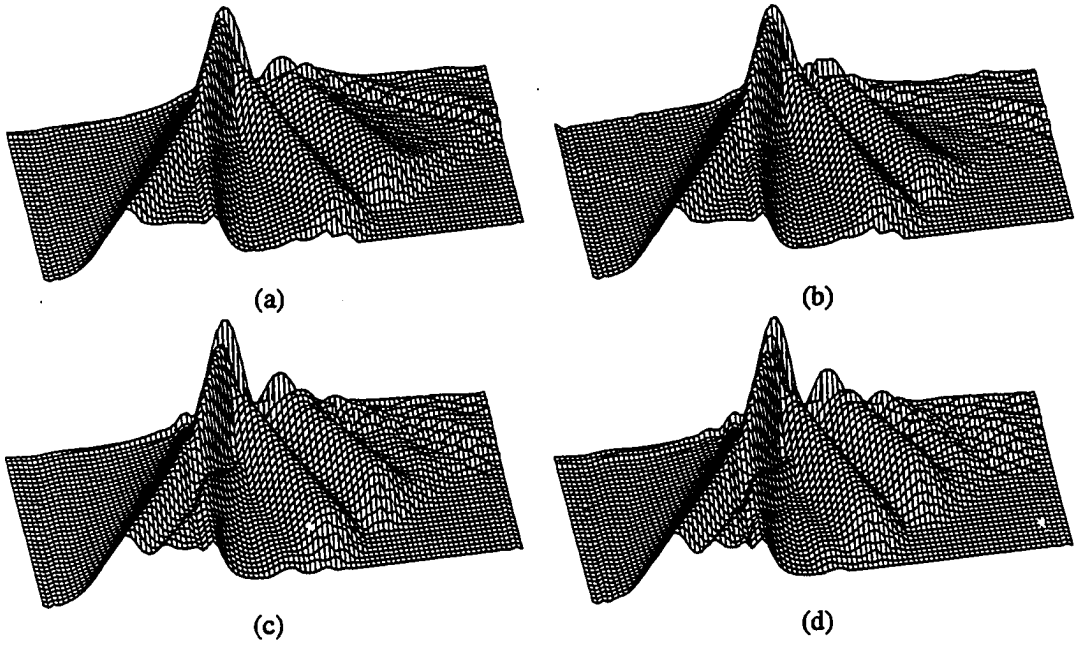

Figure 5.14: Maximum amplitude profiles based on pulses of different bandwidth, (a) 6 MHz, (b) 6 MHz (with crack), (c) 3.6 MHz, (d) 2.6 MHz.

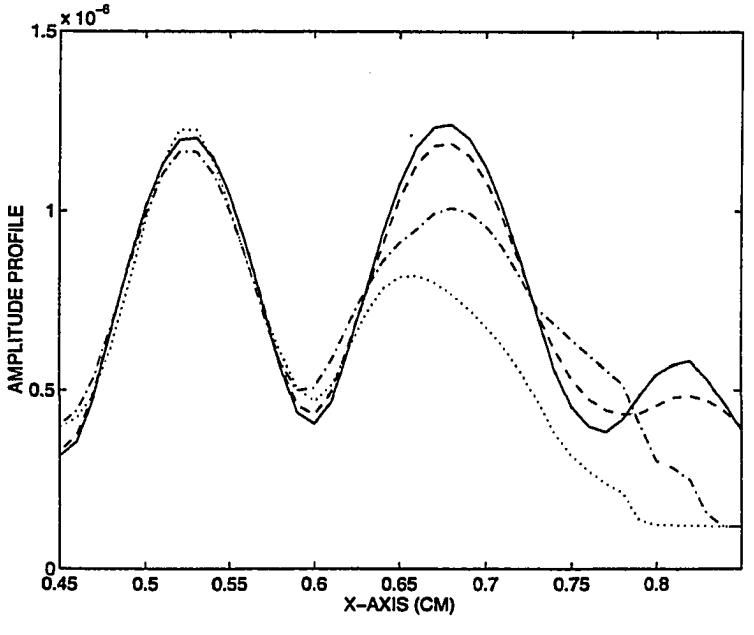

Figure 5.15: Profile from Fig. 5.14 with y=0.20 cm, with bandwidth of 2.6 MHz(solid line), 3.6 MHz (dashes), 6 MHz (dash-dots) and 6 MHz with crack (dots).

Case 3

As a third case, assume a cylindrically focused wave from a 2D strip aperture with width of 1 cm and focal length of 0.6 cm. The geometry in this case, as shown in Fig. 5.9(c) is symmetrical (about x=0 plane) and only half is discretized. Like case 1, a non-reflective boundary condition is put on the bottom surface. The wave profiles are shown in Fig. 5.16. Fig. 5.16(a) shows the incident wave front where the maximum incident angle is 39.8 degrees as well as the excitation of the leaky Rayleigh wave as the incident wave strikes the interface. At that instant, no longitudinal waves are observed since the incident waves are above the longitudinal critical angle. At a later time as shown in Fig. 5.16(b), a transmitted longitudinal wave is excited by the near-axis part of the incident wave. Fig. 5.16(c) shows specularly reflected and focused wave fronts and a plane wave front from the leaky Rayleigh wave. Fig. 5.16(d) indicates the effect of a subsurface crack of similar features as in case 2 but located at x=0.3 cm. The reflected leaky Rayleigh wave from the crack and its radiation back to the fluid medium are observed.

In summary, by considering three cases of fluid/solid interfaces with different source configurations, the transient wave profiles are predicted by the finite element method. The properties associated with the generation and propagation of the leaky Rayleigh waves are described. The results indicates that the leaky Rayleigh wave is excited when a wave front strikes an interface at the Rayleigh angle. An ordinary Rayleigh wave is converted to a leaky Rayleigh wave upon the loading of a fluid layer on the solid medium. The leaky Rayleigh wave propagates with exponential attenuation due to the continuous radiation to the fluid medium. A subsurface crack or void partially reflects and scatters the leaky Rayleigh wave and the reflected leaky

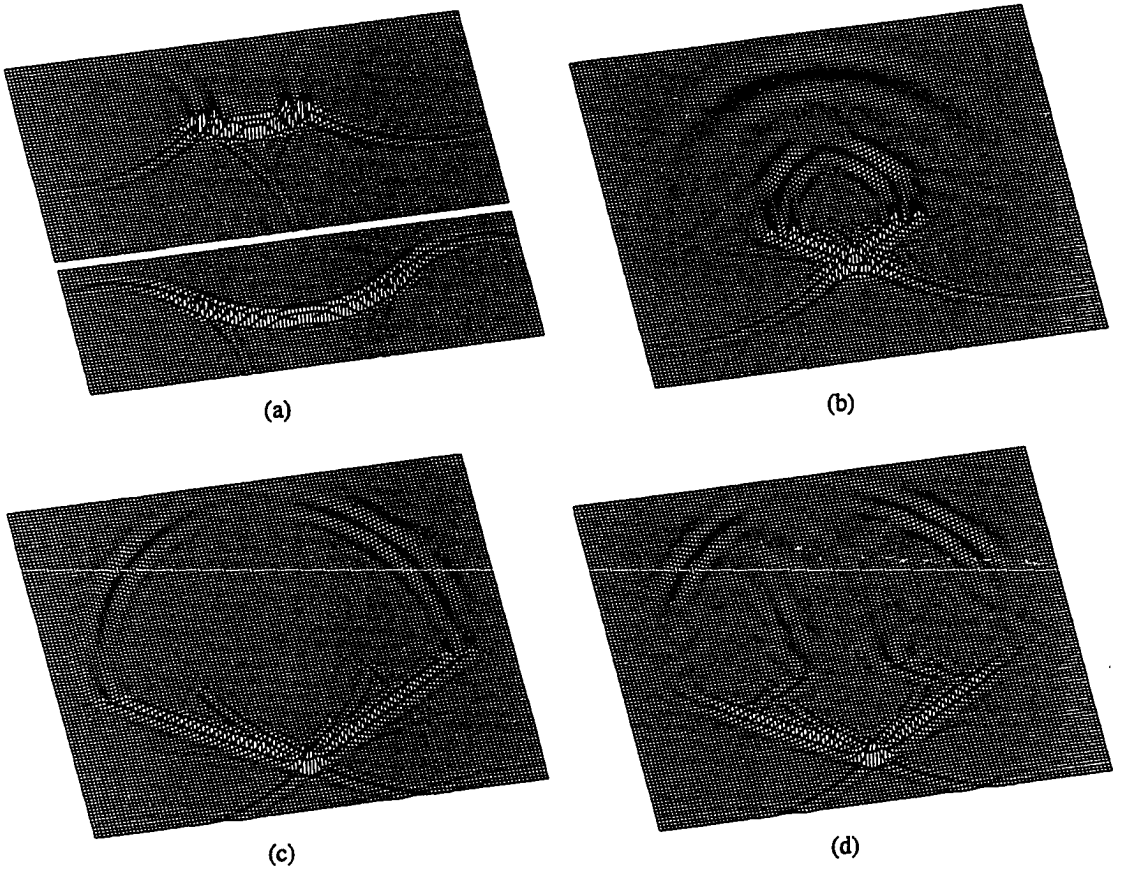

Figure 5.16: Wave profiles corresponding to geometry Fig. 5.9(c), (a) t=2.5, 4, (b) 5 (c) 6 (without crack) and (d) t=6 (with crack) microseconds.

Rayleigh wave again possesses the properties of a forward Rayleigh wave. The finite element approach is effective in producing the full fields of the spatial region of interest and for adopting various kinds of boundary conditions. With this method, the study can be extended readily in the following aspects: more complex shapes of the interface and defects; anisotropic solid medium with fluid loads; and multi-layer solid media with fluid loads.

CHAPTER 6. FIELDS OF ULTRASONIC TRANSDUCERS AND TIME-DELAY ARRAYS

In modern ultrasonic NDE, a focused acoustic beam is used to provide good transverse definition and high intensity at a particular point of interest [84]. Traditionally an ultrasonic lens or a geometrically focused transducer serves this purpose. But field depth is reduced for this configuration. An alternative choice is to use time-delay spherically focused arrays so that curved structures are avoided. Therefore, a knowledge of the transient fields of such arrays is of fundamental importance and also the major subject of this chapter. The fields of other focusing devices are treated in the next chapter.

The traditional approach for obtaining the radiated fields of arrays has been by the paraxial and farfield approximations [96,97] based on optical diffraction theory. But these techniques yield results valid only for the farfield or a small zone around the focus. One way to overcome this problem is by adding the partial effects of the array elements [98,99]. Based on the Cagniard-de Hoop technique, Aulenbacher and Langenberg [100] have reported analytical results for rectangular transducers and arrays. In addition to the application to single piston radiators, the impulse response method has also been used for various transducer arrays [101-105].

In this chapter, the radiated fields of a circular transducer and a time-delay

spherically focused transducer array are analyzed and compared using the classical impulse response method and finite element analysis. In the first approach, the velocity potential at an observation point is expressed as the convolution of the excitation velocity and the impulse response, while the pressure is obtained by the differentiation of the velocity potential. The impulse response for an array is expressed as the superposition of those of a series of circular pistons and is dependent on the observation point and piston/array structure. The finite element method starts with the formulation for elastic waves and the pressure fields are obtained through the pressure analog method. The essentials of the two approaches are presented in the next section and the resulting pressure field distributions predicted by both methods follow.

Numerical Approaches

The impulse response approach

For a uniform velocity v applied normally to the piston shown in Fig. 6.1 (a) the velocity potential generated is expressed in terms of the Rayleigh surface integral [56]

$$\phi(\mathbf{r},t) = \int_s \frac{v(t-R/c)}{2\pi R} dS \tag{6.1}$$

where $R = |\mathbf{r} - \mathbf{r_o}|$ is the distance of the observation point positioned at $\mathbf{r}$ and the differential radiation element positioned at $\mathbf{r_o}$. The impulse response is obtained by replacing v with a unit impulse, i.e.,

$$h(\mathbf{r},t) = \int_s \frac{\delta(t-R/c)}{2\pi R} dS \tag{6.2}$$

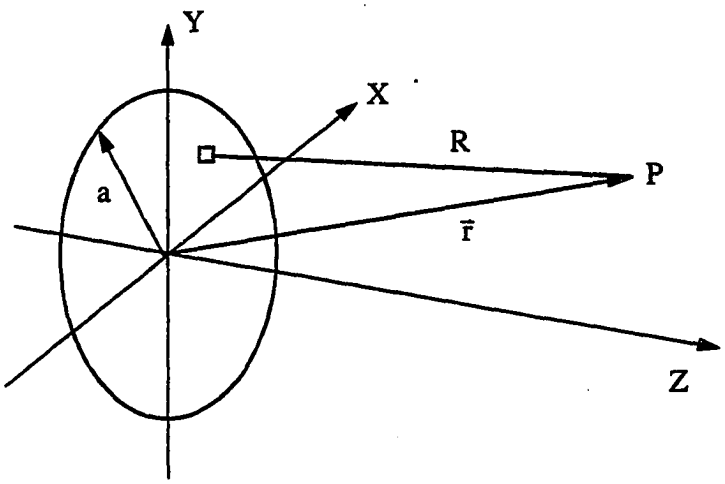

(a)

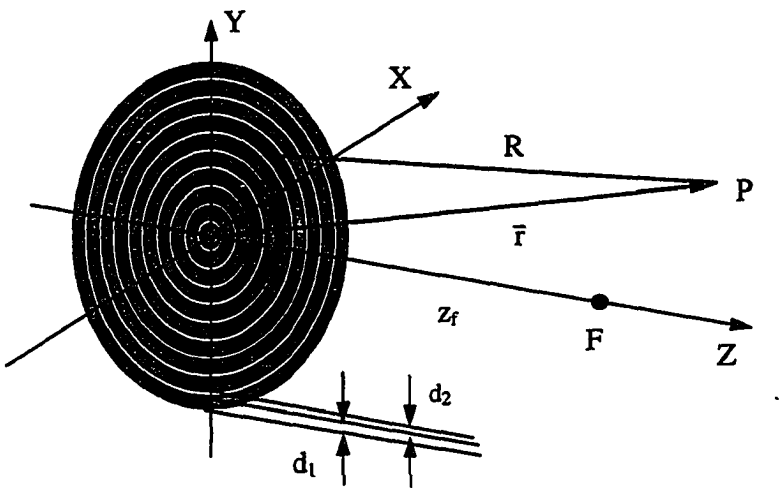

(b)

Figure 6.1: Axisymmetric geometries, (a) a circular piston, (b) a circular array.

Then ϕ can be represented in terms of h as a convolution integral

$$\phi(\mathbf{r},t) = v(t) * h(\mathbf{r},t) \tag{6.3}$$

The pressure at position $\mathbf{r}$ is expressed as

$$p(\mathbf{r},t) = \rho\frac{\partial\phi(\mathbf{r},t)}{\partial t} = \rho\frac{\partial(v(t) * h(\mathbf{r},t))}{\partial t} \tag{6.4}$$

where ρ is the mass density of the medium at equilibrium, or alternatively

$$p(\mathbf{r},t) = \rho v(t) * \frac{\partial h(\mathbf{r},t)}{\partial t} = \rho\frac{\partial v(t)}{\partial t} * h(\mathbf{r},t) \tag{6.5}$$

It is seen that the key point of the problem is the determination of the impulse response h. Evaluation of Eq. (6.2) yields [63]

$$h(\mathbf{r},t) = \frac{c}{2\pi}\Omega(\mathbf{r},t) \tag{6.6}$$

where c is the longitudinal wave velocity in the medium and Ω is the arc angle (in radians) of the intersecting arc of the sphere centered at the observation point with radius ct and the transducer plane. Therefor h is time limited, i.e., it has nonzero values for t such that ct is between the minimum and maximum distance of the observation point and the transducer surface.

For a circular piston of radius a, the impulse response can be expressed in closed form. Assume r and z are the radial and axial coordinates of the observation point,

then

$$h(\mathbf{r},t) = \begin{cases} h(r<a,t) = \begin{cases} 0, & ct < z \\ c, & z \le ct \le R_1 \\ \theta(ct), & R_1 < ct < R_2 \\ 0, & ct \ge R_2 \end{cases} \\ h(r=a,t) = \begin{cases} 0, & ct < z \\ c/2, & ct = R_1 \\ \theta(ct), & R_1 < ct < R_2 \\ 0, & ct \ge R_2 \end{cases} \\ h(r>a,t) = \begin{cases} 0, & ct < R_1 \\ \theta(ct), & R_1 < ct < R_2 \\ 0, & ct \ge R_2 \end{cases} \end{cases} \tag{6.7}$$

where

$$R_1 = \sqrt{(r-a)^2 + z^2}$$

$$R_2 = \sqrt{(r+a)^2 + z^2}$$

and

$$\theta(ct) = \frac{c}{\pi}\cos^{-1}\left[\frac{(ct)^2 - z^2 + r^2 - a^2}{2r((ct)^2 - z^2)^{1/2}}\right] \tag{6.8}$$

An axisymmetric time-delay array with N elements is shown in Fig. 6.1(b). Assume the i^{th} elemental impulse response is denoted as h_i^e, then the pressure at an observation point due to the array is

$$p(\mathbf{r},t) = \sum_i \rho v(t - T_i) * \frac{\partial h_i^e(\mathbf{r},t)}{\partial t}$$

$$= \sum_i \rho \frac{\partial v(t)}{\partial t} * h_i^e(\mathbf{r}, t - T_i)$$
$$= \sum_i \rho \frac{\partial v(t)}{\partial t} * h_A(\mathbf{r}, t) \tag{6.9}$$

where

$$h_A(\mathbf{r}, t) = \sum_i h_i^e((\mathbf{r}, t - T_i) \tag{6.10}$$

while

$$h_i^e(\mathbf{r}, t - T_i) = h_{2i-1}(\mathbf{r}, t - T_i) - h_{2i-2}(\mathbf{r}, t - T_i) \tag{6.11}$$

with notation $h_o = 0$. Substituting (6.11) into (6.10) yields a compact form

$$h_A(\mathbf{r}, t) = \sum_{i=1}^{N} h_{2i-1}(\mathbf{r}, t - T_i) - \sum_{i=2}^{N} h_{2i-2}(\mathbf{r}, t - T_i)$$
$$= \sum_{j=1}^{2N-1} (-1)^{j-1} h_j(\mathbf{r}, t - T_i) \tag{6.12}$$

where $k = (2j + (-1)^j + 3)/4 = \text{int}(j/2) + 1$ and h_j are as determined from Eq. (6.7) with

$$a_j = \frac{j}{2}(d_1 + d_2) + \frac{(-1)^{j-1} + 1}{4}(d_1 - d_2) \tag{6.13}$$

where d_1 is the width of each element and and d_2 is the space between two neighboring elements. Notice that the diameter of the innermost element is $2d_1$. The elemental time- delay for spherical focusing is determined as follows. The center radius for the i^{th} element is

$$r_i = (i - 1)(d_1 + d_2) + \frac{1}{2}d_1 \tag{6.14}$$

Notice that the center radius for the innermost element is represented by $d_1/2$ rather than zero. If the focal length is chosen to be z_f, the distance from the center of each element to the focal point is

$$r_i = (r_i^2 + z_f^2)^{1/2} \tag{6.15}$$

Assume that the time delay at r_N is zero. Then

$$T_i = \frac{1}{c}\left[(r_N^2 + z_f^2)^{1/2} - (r_i^2 + z_f^2)^{1/2}\right] \tag{6.16}$$

The finite element approach

It is seen from the last chapter that in the pressure analogy, the z component of surface traction becomes the product of the fluid bulk modulus and the normal derivative of the pressure, and is further proportional to the time derivative of the normal surface velocity. The corresponding force term is

$$F_v = A\rho^2 c^2 \ddot{u}_n = A\rho^2 c^2 \dot{v} \tag{6.17}$$

where u_n and v are the normal surface displacement and velocity, respectively. An absorbing boundary condition for the radiation problem is as follows,

$$F_b = A\rho c(-\cos\theta)\dot{U}^p \tag{6.18}$$

where θ is the incident angle and A is the area associated with the node. The finite element equations assume the following form

$$M\ddot{U}^p + KU^p = F^v + F^b \tag{6.19}$$

or

$$M\ddot{U}^p + D\dot{U}^p + KU^p = F^v \tag{6.20}$$

where D is a diagonal matrix whose nonzero elements correspond to the coefficients in Eq. (6.18) (i.e., $A\rho c(-\cos\theta)$) for the absorbing boundary nodes. On the axis of symmetry, the radial derivative of U^p should vanish under the axisymmetric condition.

Based on the explicit integration scheme and mass lumping technique in Chapter 3, the solution to Eq. (6.20) is as follows,

$$\begin{aligned} U^p_{t+\Delta t} &= \Delta t^2 (M^{Diag})^{-1} F^v_t - (K + \frac{1}{\Delta t} D)\Delta t^2 (M^{Diag})^{-1} U^p_t + \\ &\quad + 2U^p_t + \Delta t (M^{Diag})^{-1} D U^p_{t-\Delta t} - U^p_{t-\Delta t} \end{aligned} \tag{6.21}$$

where the parameters are the same as in Chapter 3 except that the solid medium is replaced by an ideal fluid.

Nearfields of the Planar Transducer

Fig. 6.1(a) shows the geometry for the planar transducer, where $2a$=0.60 cm. The medium properties throughout this study are c=1500 m/s and ρ=1000 kg/m^3 The transducer is simply modeled as a piston with the excitation pulse uniformly applied. The three excitation pulses are in the same form as that in Chapter 4 with the center frequency reduced by one half, i.e.,

$$f(t) = \left[u(t) - u\left(t - \frac{2n\pi}{\omega_o}\right)\right]\left(1 - \cos\frac{\omega_o t}{n}\right)\cos\omega_o t \tag{6.22}$$

where u(t) is the unit step function, w_o=$2\pi f_o$, f_o=2.5 MHz, and n=3, 5 and 7 for the three pulses respectively. Pulses 1, 2 and 3 are in the order of increasing pulse length and decreasing bandwidth. If no indication is made, pulse 1 is assumed to be the excitation signal. All the results that follow are obtained by using a DEC alpha station. Square elements are used for the finite element approach. Unless otherwise stated, the number of elements per wavelength (EPW) is 20, and the time step is below the critical value.

Fig. 6.2 shows the impulse response function of the circular piston in the plane at z=0.9 cm with radial values from zero to 0.6 cm. The time-limitedness is clearly

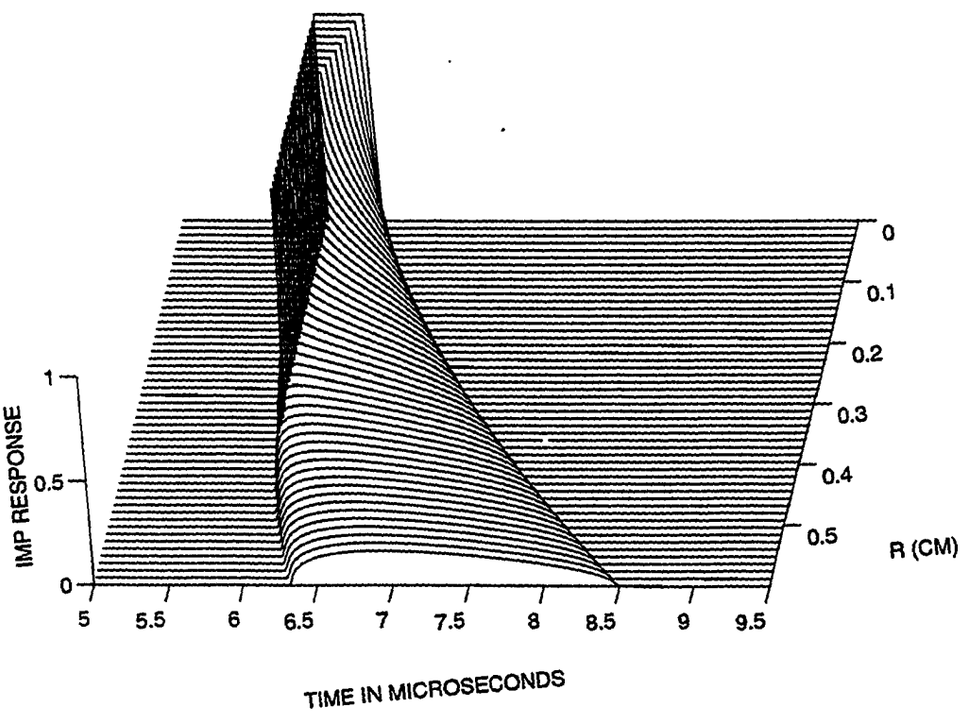

Figure 6.2: Normalized impulse response for the piston in the plane at z=0.9 cm.

indicated. The maximum magnitude begins to drop for r greater than a. The pressure response in the same plane for excitation pulse 1 using the impulse response method is shown in Fig. 6.3 while the corresponding pressure by the finite element approach is shown in Fig. 6.4. The major pulse is a combination of the direct wave and the edge wave while the secondary pulse is an edge wave. It can be seen that excellent agreement is achieved for the two methods. Shown in Fig. 6.5 are the A-scan plots for excitation pulse 1 at a few points along the z-axis. At the neighborhood of the piston, two separate pulses, i.e., the direct wave and the edge wave which are of equal magnitude but opposite phase exist. This is expected since the propagation time difference is significantly larger than the pulse width. For observation points on the z-axis further from the piston, the time difference between the direct wave and the edge wave decreases. When this difference reaches the pulse width, the two pulses begin to overlap. Still further on the axis the time difference approaches zero and the two pulses tend to cancel each other because of their opposite phases and thus make the axial pressure amplitude decrease from the maximum. It is noted that with the increase of distance from the piston, deviation between the two methods appears. This is caused by the spatial discretization of the finite element method. As shown in Fig. 6.6, smaller mesh size yields more accurate results.

Fig. 6.7 displays the overall nearfield for the three excitation pulses by the two different approaches. The transverse ripples near the transducer edge, more obvious for the narrower-band pulse, confirm the ring effect observed by Beaver [65]. Fig. 6.8 shows the normalized axial pressure amplitudes. It can be seen that the nearfields differ significantly for different excitation bandwidths with more abrupt variations for the narrow-band pulse.

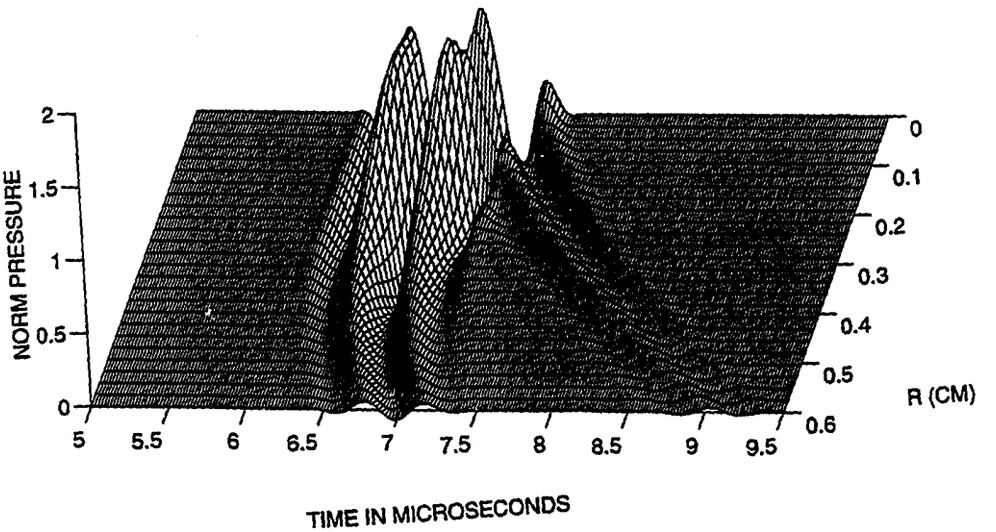

Figure 6.3: Transient fields for the piston in the plane at z=0.9 cm using the impulse response approach.

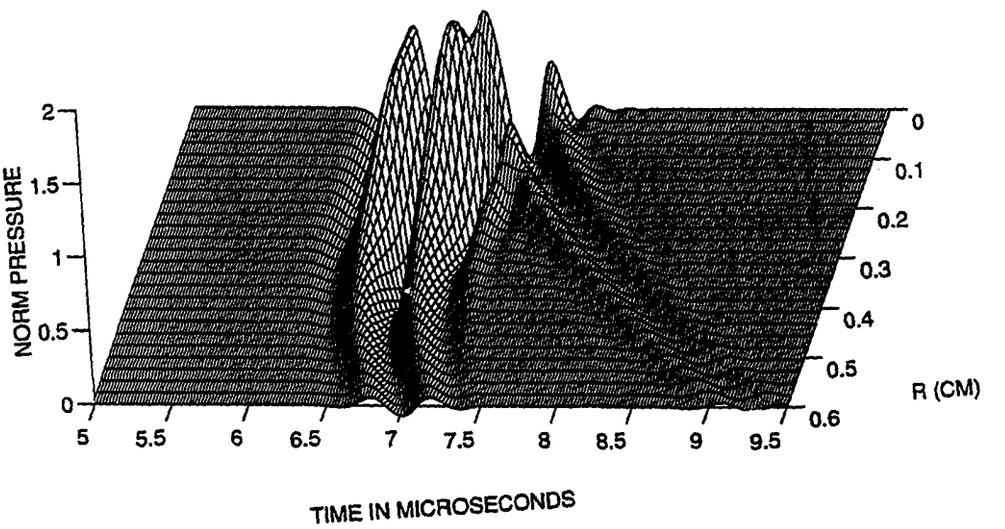

Figure 6.4: Transient fields for the piston in the plane at z=0.9 cm using the finite element approach.

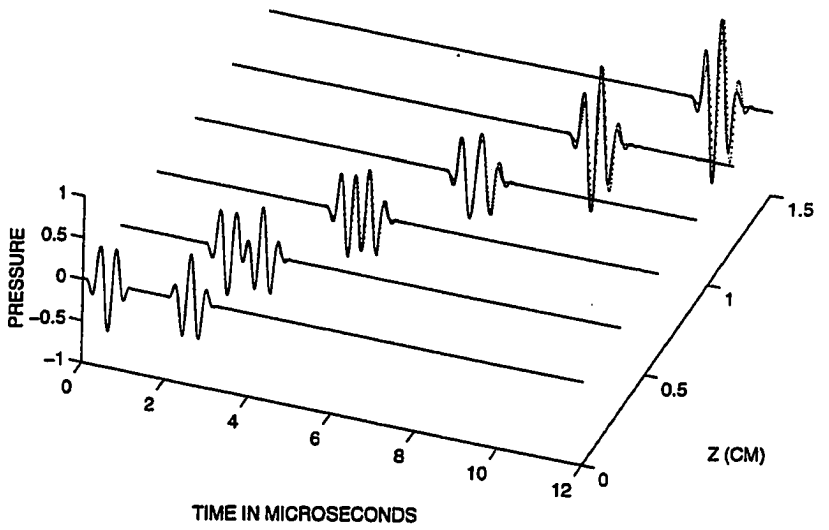

Figure 6.5: Transient pressure fields for the piston on the axis of symmetry normalized with respect to the maximum peak, solid line (Imp), dotted line (FEM).

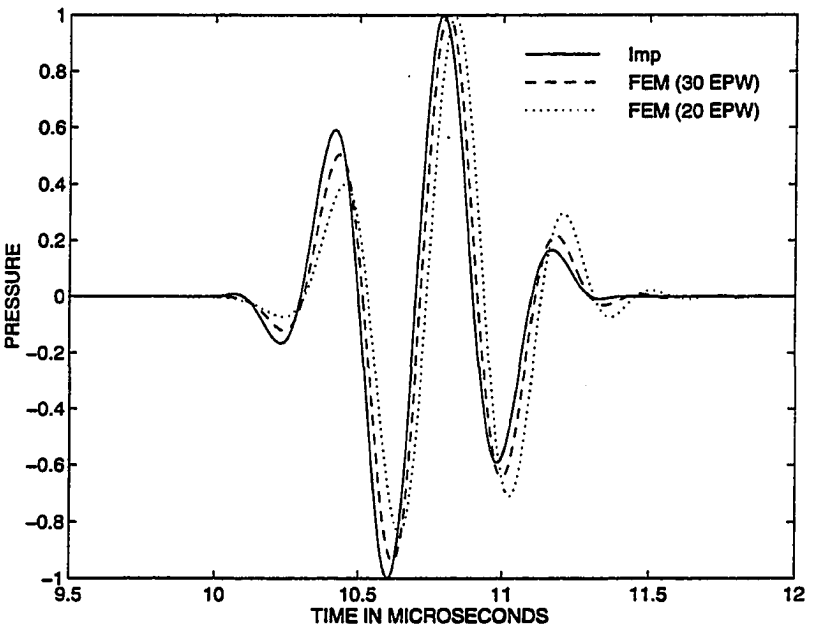

Figure 6.6: Transient pressure fields for the piston on the axis of symmetry at z=1.5 cm.

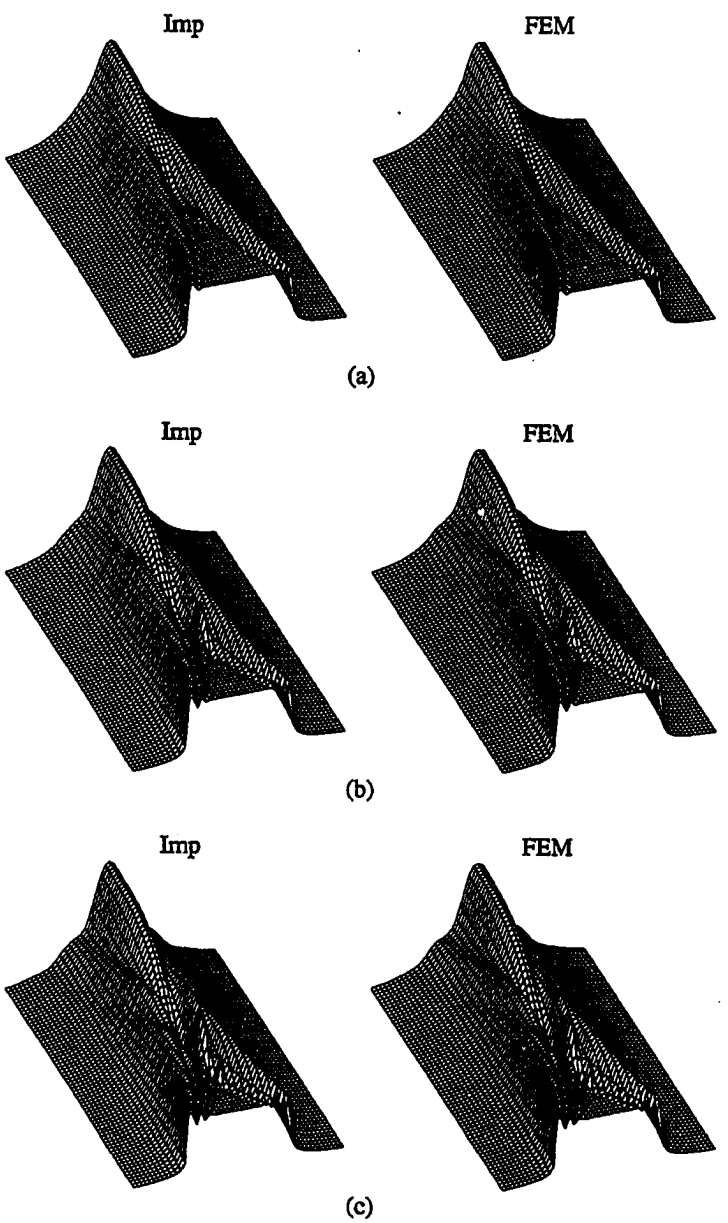

Figure 6.7: Pressure field distribution for the piston with excitation (a) pulse 1, (b) pulse 2 and (c) pulse 3.

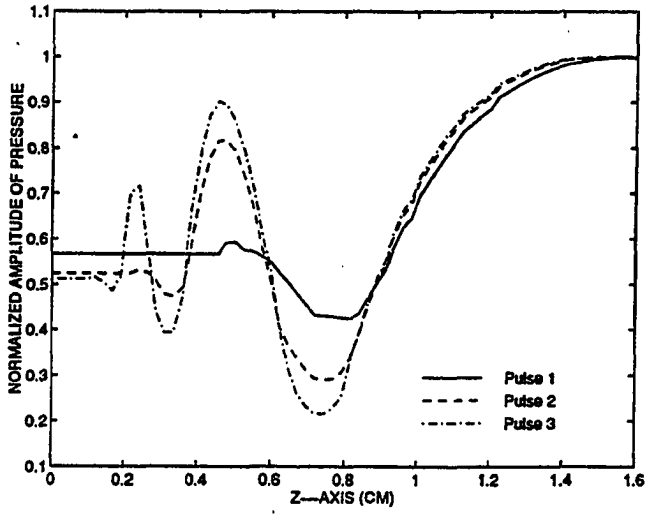

(a)

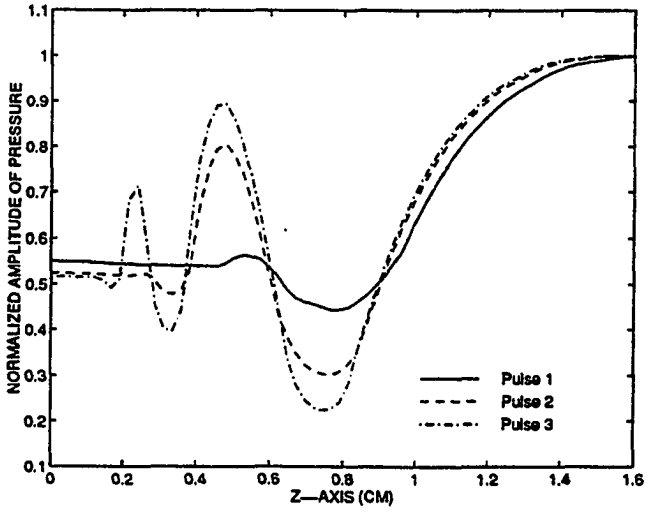

(b)

Figure 6.8: Normalized axial pressure for the piston using (a) FEM, (b) impulse response method.

Field of the Time-delay Array

For the time-delay array the following parameters are chosen, d_1=0.02 cm, d_2=0.01 cm and N=10. Thus the outer diameter is 0.58 cm which is approximately the same as the circular piston presented in the last section. The specified focal length z_f=0.9 cm. The time delays Ti are determined according to Eq. (6.16).

Fig. 6.9 shows the array impulse response at plane z=0.9 cm for r=0 to 0.6 cm. Though it is normalized by itself, the maximum amplitude is 10 times that for the single piston. The peak around the axis has been truncated to only 10 percent of the maximum value. A more abrupt change of magnitude close to the axis is seen here than in Fig. 6.2 for the circular piston. Figs. 6.10 and 6.11 show the corresponding pressure pulses for excitation pulse 1 predicted by the impulse response approach and the finite element approach respectively. Good agreement is seen and the pulses are more concentrated at the axis than in the case of the circular piston. This is expected because of the focusing effect. Figs. 6.12 and 6.13 are the A-scan plots on the axis of symmetry of the array, which are analogous to Figs. 6.5 and 6.6 for the single piston. A time shift can be seen for the array. As expected, the magnitude reaches maximum around the focal point and then decrease along the axis.

Fig. 6.14 shows the wave profiles of the array for excitation pulse 1 with z=0 to 1.8 cm and r=0 to 1.2 cm at three different time instants by the impulse response method on the left half and the finite element approach (30 EPW) on the right half of each plot. Good agreement can be seen for each plot and the focusing effect is clearly indicated. The pressure fields for the array are shown in Fig. 6.15 for the same area as that in Fig. 6.7. But here the focusing effect is clearly indicated. Shown in Fig. 6.16 is the normalized axial pressure field for the array by the two approaches. It

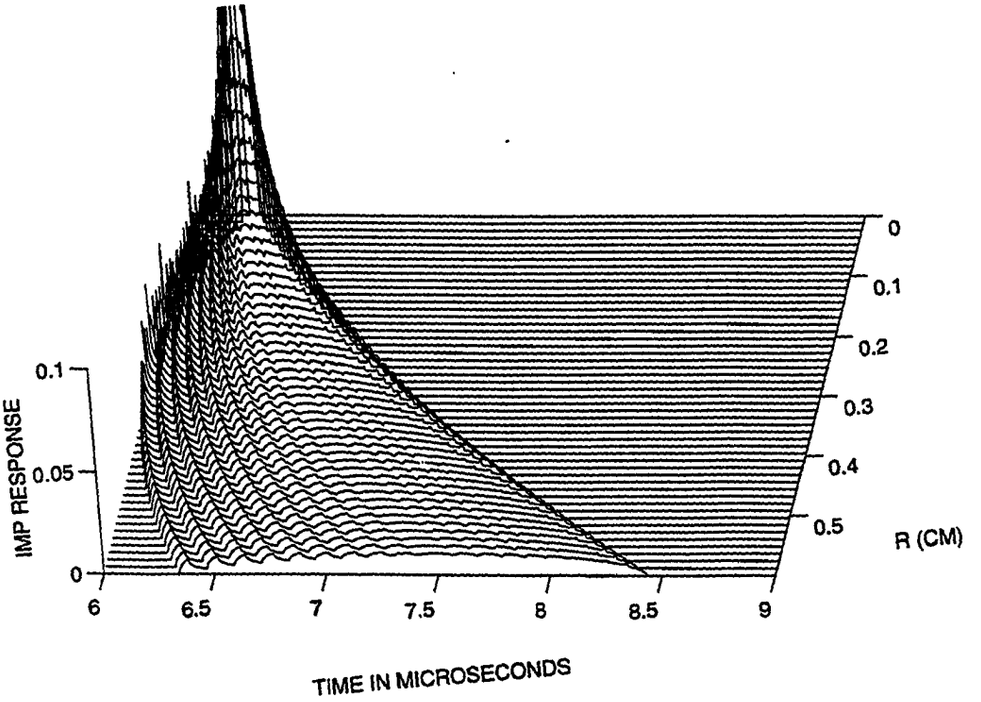

Figure 6.9: Normalized impulse response for the array in the specified focal plane z=0.9 cm. The peak value is 10 times that of Fig. 6.2.

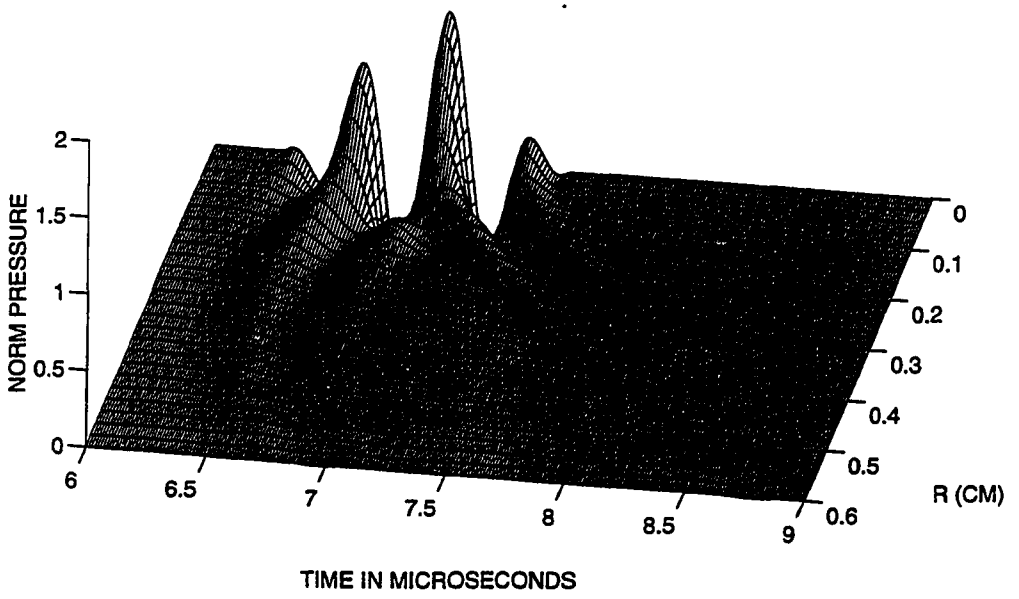

Figure 6.10: Transient fields for the array in the specified focal plane using the impulse response approach.

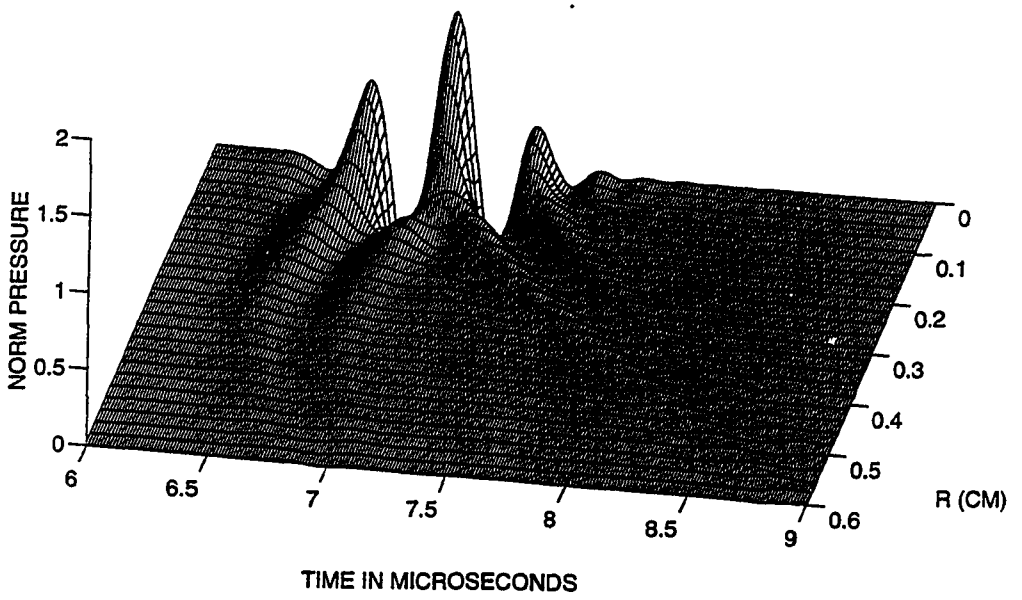

Figure 6.11: Transient fields for the array in the specified focal plane using the finite element approach.

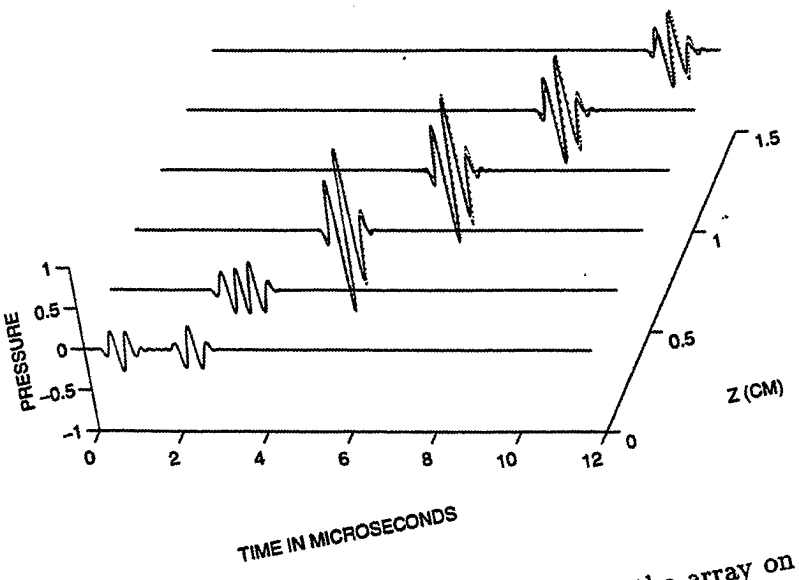

Figure 6.12: Normalized transient pressure fields for the array on the axis of symmetry, solid line (Imp), dotted line (FEM).

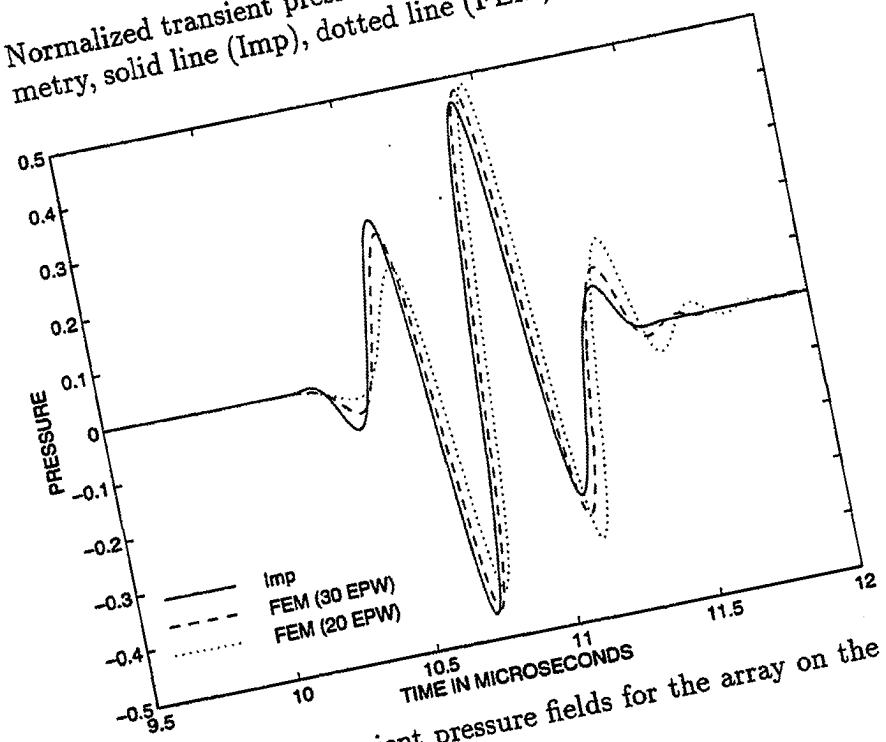

Figure 6.13: Normalized transient pressure fields for the array on the axis of symmetry at z=1.5 cm.

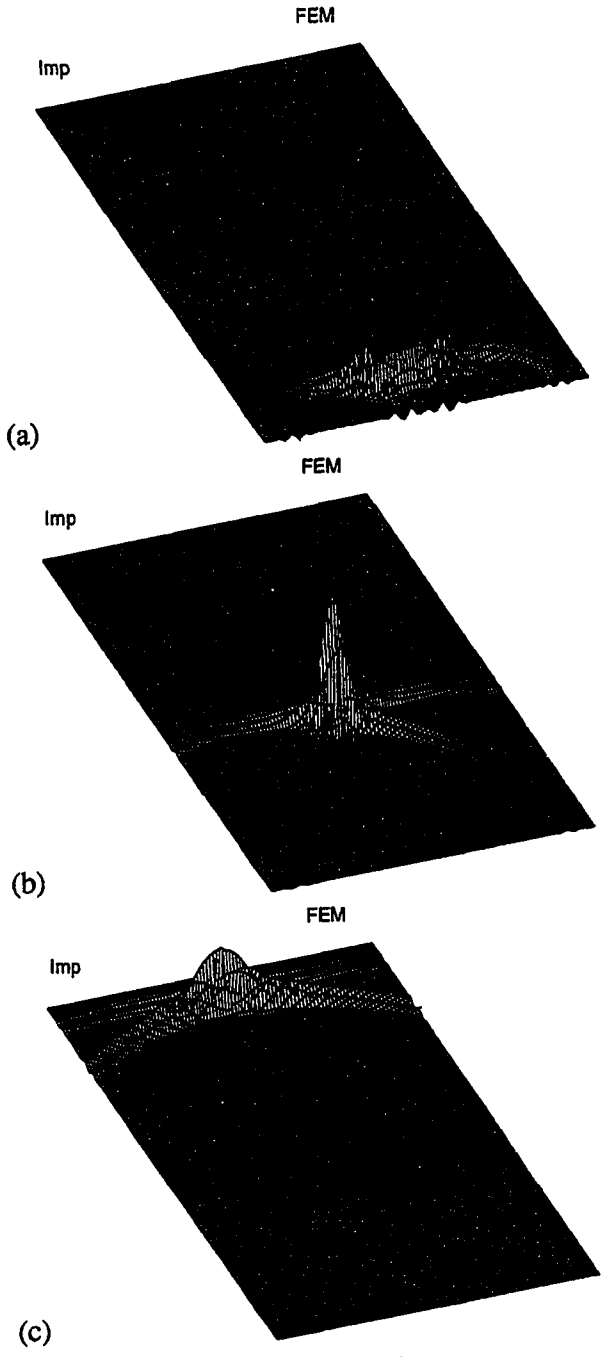

Figure 6.14: Wave profiles for the array with excitation pulse 1 at time instants (a) 2, (b) 6, and (c) 12 μs. (Note: The left half of each plot is predicted by the impulse response method and the right half by the finite element method.)

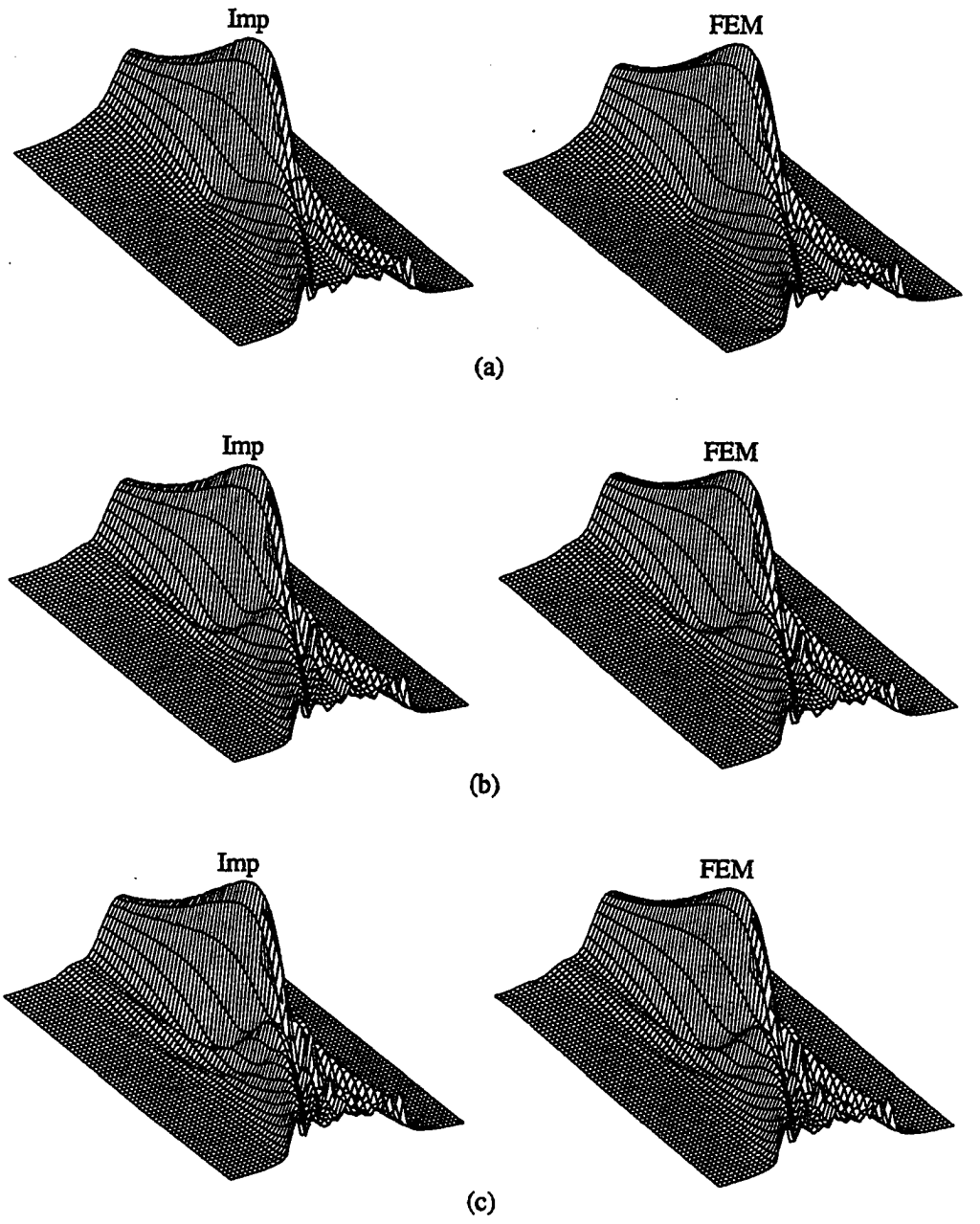

Figure 6.15: Pressure field distribution for the array with excitation (a) pulse 1, (b) pulse 2 and (c) pulse 3.

can be seen that the plots are very similar to those for the spherical radiator. For example, the specified focal plane is at z=0.9 cm but the true focal plane is around z=0.65 cm which is closer to the radiator. The maximum amplitude is twice that for the piston. Fig. 6.17 shows the radial pressure fields in the specified focal plane predicted by the finite element approach on the left half and the impulse response approach on the right half of each plot. It is noted that each plot in Fig. 6.17 has been normalized on its own and the amplitude relationship between them can be seen from Fig. 6.16. It is seen from both Figs. 6.16 and 6.17 that smoother nearfields are obtained by using a short excitation pulse with larger bandwidth. The simple explanation is that, when the bandwidth decreases, the radiation pattern approaches the sinusoidal case.

A summary is as follows. The radiated fields of the circular piston and time-delay array are obtained comparatively using impulse response and finite element approaches. The results include the transient fields at discrete points, the wave profiles over some spatial region at various time instants and also the normalized amplitudes of the pressure fields. Good agreement has been achieved for the two approaches. One feature of the impulse response method is that it allows the transient fields of specific points of interest to be determined without having to work on other points, while the advantage of the finite element method is that it is able to determine the overall fields of a certain spatial region of interest with a greater efficiency. It is noted that beam steering and dynamic focusing for off-axis points require a 3D formulation which in turn demands greater computer resources. Of course, the real power of the finite element method lies in the broad range of simulation of wave propagation and scattering and interaction with multiple media of arbitrary geometry.

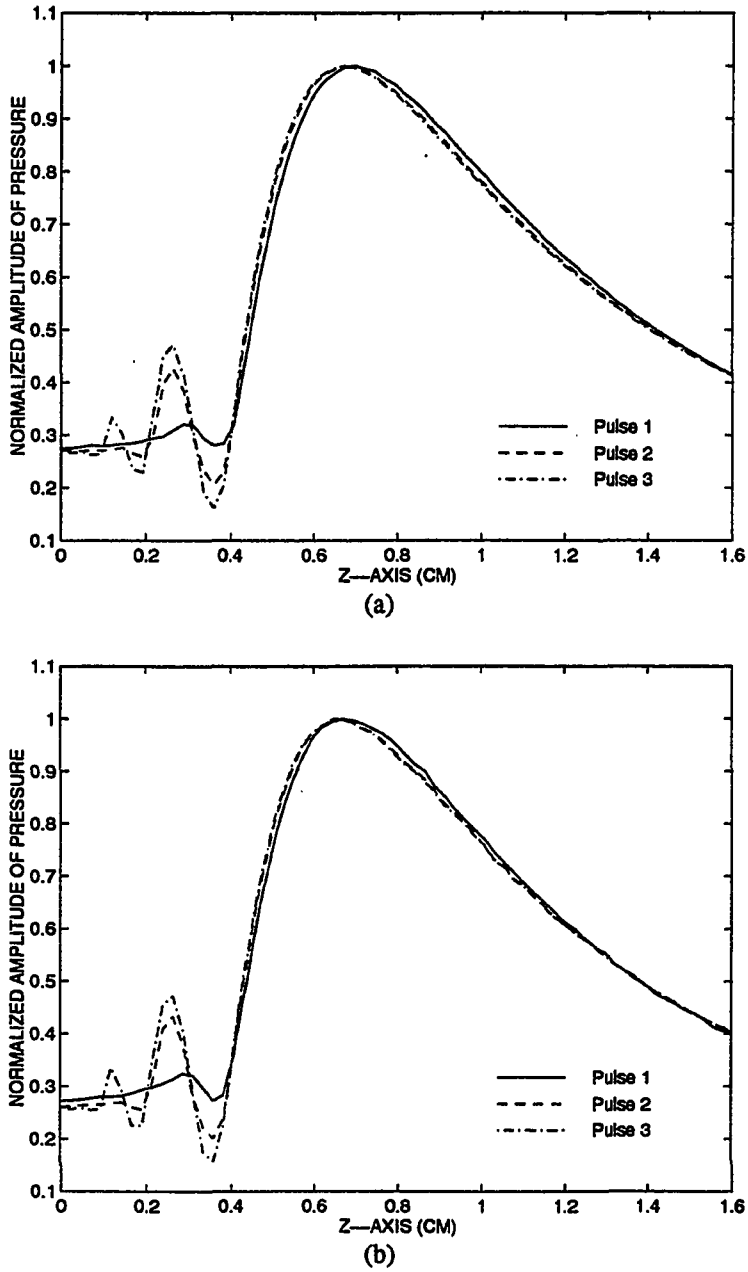

Figure 6.16: Normalized axial pressure for the array using (a) FEM, (b) impulse response method. The peak value is about twice that of Fig. 6.8.

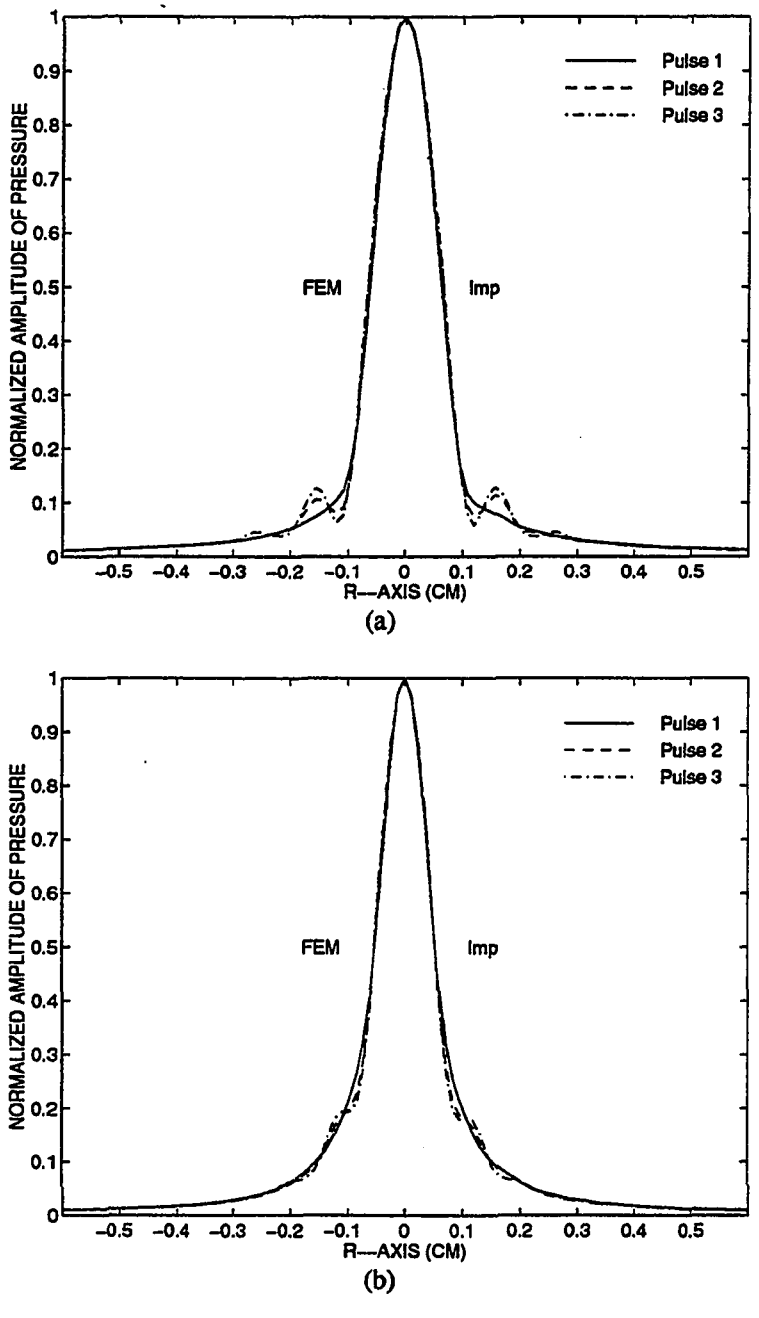

Figure 6.17: Normalized transverse pressure for the array in (a) specified focal plane and (b) true focal plane. (Note: The left half of each plot is predicted by finite element analysis and the right half by the impulse response method.)

Effects of Array Structural Parameters

It has been demonstrated that the finite element method is superior for finding the overall nearfields which are usually of interest for imaging applications. In this section, the finite element method is used for obtaining the field distributions of different array structures including the variation of aperture width, focal length, element width/spacing ratio, etc. The excitation function throughout this study is of the following form

$$f(t) = \left[u(t) - u\left(t - \frac{2(2n-1)\pi}{\omega_o}\right)\right] \cos\omega_o t \tag{6.23}$$

where u(t) is the unit step function, $\omega_o = 2\pi f_o$ and f_o=2.5 MHz. The integer n controls the bandwidth and a larger value of n corresponds to a narrower bandwidth.

Three arrays (Nos. 1, 2 and 3) with outer diameters of 0.6, 1.2 and 1.8 cm are modeled. In one aspect of the study, we assume that the elements in all the arrays have the same width and are equally spaced, e=0.67 and s=0.33 mm, and e/s=2. The focal length is assumed to be 0.75 cm. Fig. 6.18 shows the wave fronts for array 2 with excitation n=2 at three different time instants, t=3, 7 and 11 μs. Though radiated by different elements, the net pressure fields are virtually composed of two major wave fronts, the direct wave and the edge wave, as indicated in Fig. 6.18(a). Fig.6.18(b) indicates that the pulse is around the focal point. Figs. 6.19, 6.20, and 6.21 display the pressure field distributions for the three arrays. The influence of the bandwidth is included in each case. Fig. 6.22 shows the normalized axial pressure fields for the three arrays. The plots are normalized with respect to the highest maximum value and are displayed in dB. Fig. 6.23(a) indicates the effect of focal length variation on the axial pressure fields for array 2 with excitation n=2.

The letters a through h in the plot indicate focal lengths of 0.15, 0.3, 0.45, 0.6, 0.75, 0.9, 1.2 and 1.5 cm, respectively. A sharper focusing is achieved if the focal point is closer to the transducer array. Fig. 6.23(b) shows the effect of the element width/spacing ratio on the axial field. Although the curves look similar, a higher width/ spacing ratio yields a higher pressure magnitude and should be recommended for practical implementation whenever possible. All the above results have been based on a single focusing. Figs. 6.24(a) shows the field distribution with multiple focusing, i.e, different parts of the array (No. 2, n=2) focuses at different points. Of the 20 elements, the inner 12, middle 5 and outer 3 are electronically focused to f=0.6, 0.75 and 0.9 cm respectively. The total effect is an extension of the focal region. Fig. 6.24(b) shows the axial field along with the single focusing (f=0.75 cm).

In summary, factors such as the excitation bandwidth, aperture width, focal length, element width and spacing, as well as multiple focusing, all affect the field patterns and are examined through finite element analysis. The quantitative results may serve as a valuable tool for the design of arrays.

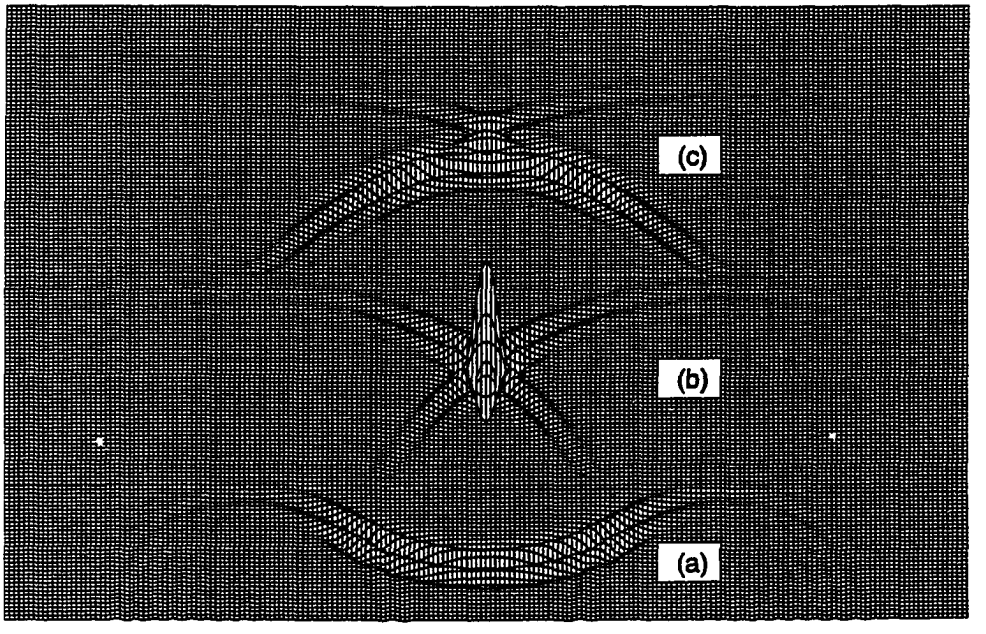

Figure 6.18: Pressure wave profiles of array 2 with excitation n=2 for three different time instants, (a) t=3 μs, (b) t=7 μs, and (c) t=11 μs. The area shown is r=0 to 1.2 cm and z=0 to 1.8 cm.

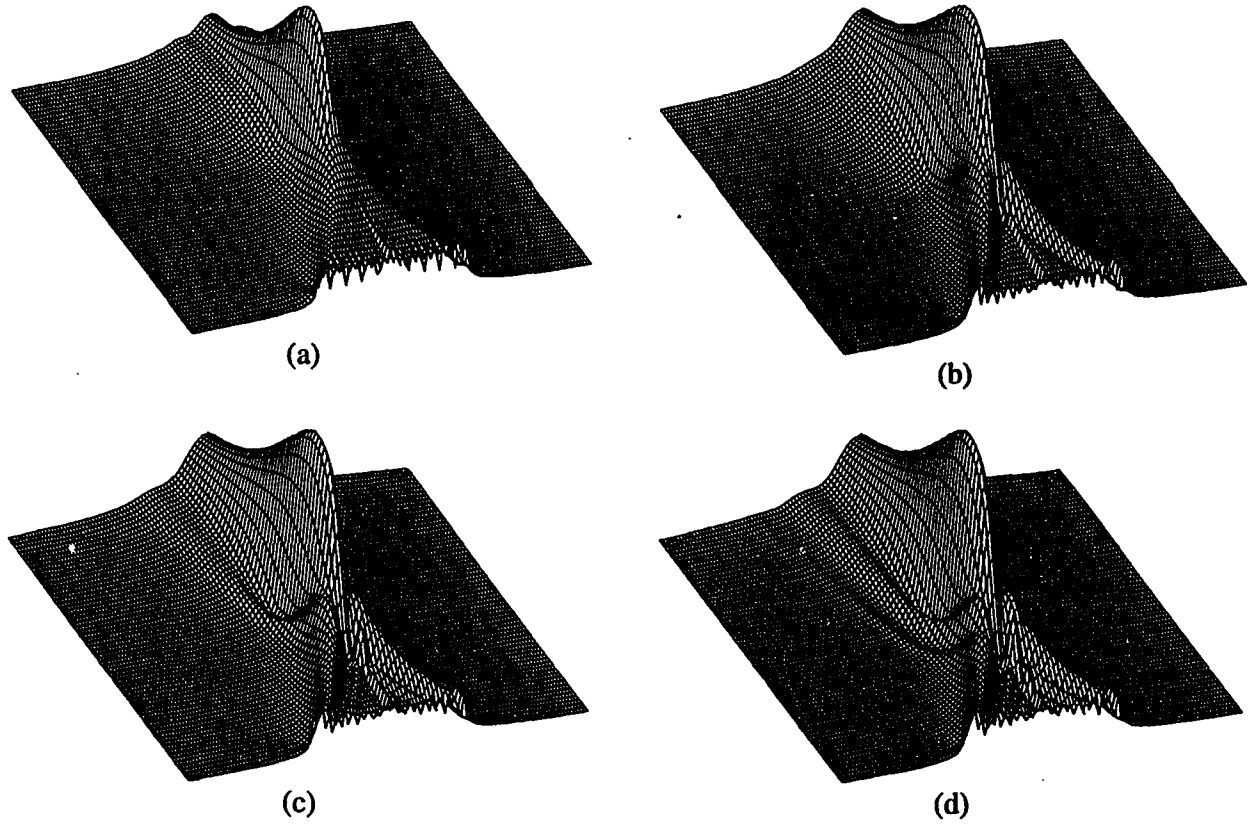

Figure 6.19: Field distribution for array 1 with excitations (a) n=1, (b) n=2, (c) n=3 and (d) n=4. The area shown from now on is r=0 to 0.75 cm and z=0 to 1.5 cm.

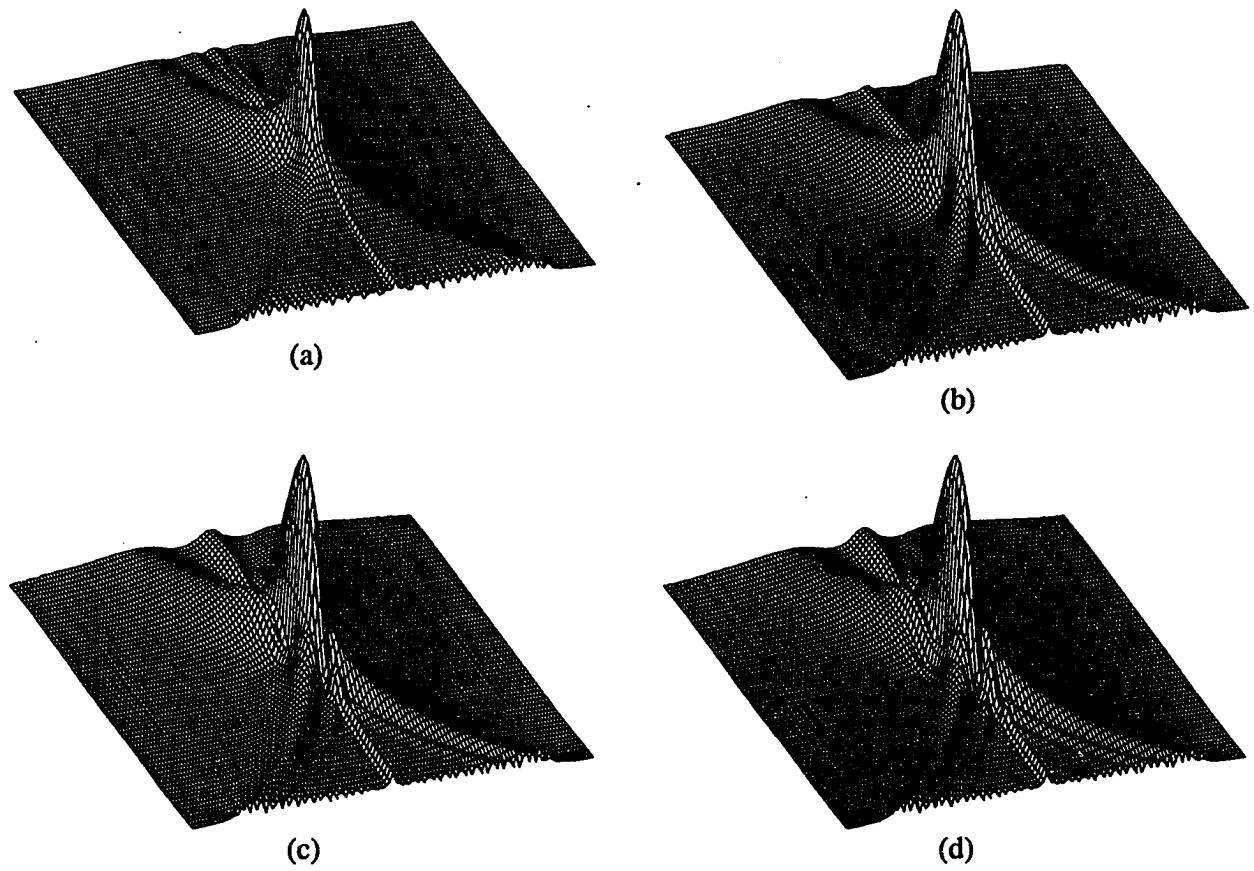

Figure 6.20: Field distribution for array 2 with excitations (a) n=1, (b) n=2, (c) n=3 and (d) n=4.

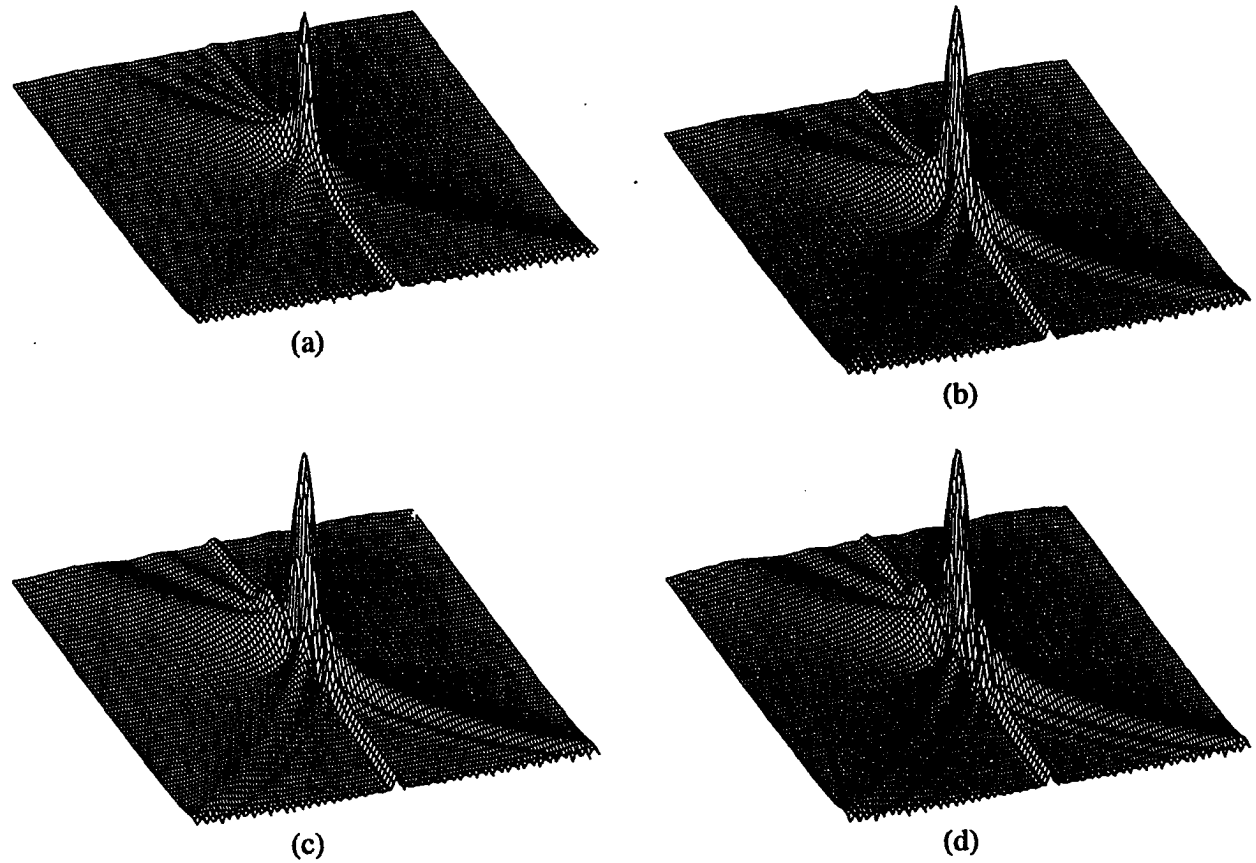

Figure 6.21: Field distribution for array 3 with excitations (a) n=1, (b) n=2, (c) n=3 and (d) n=4.

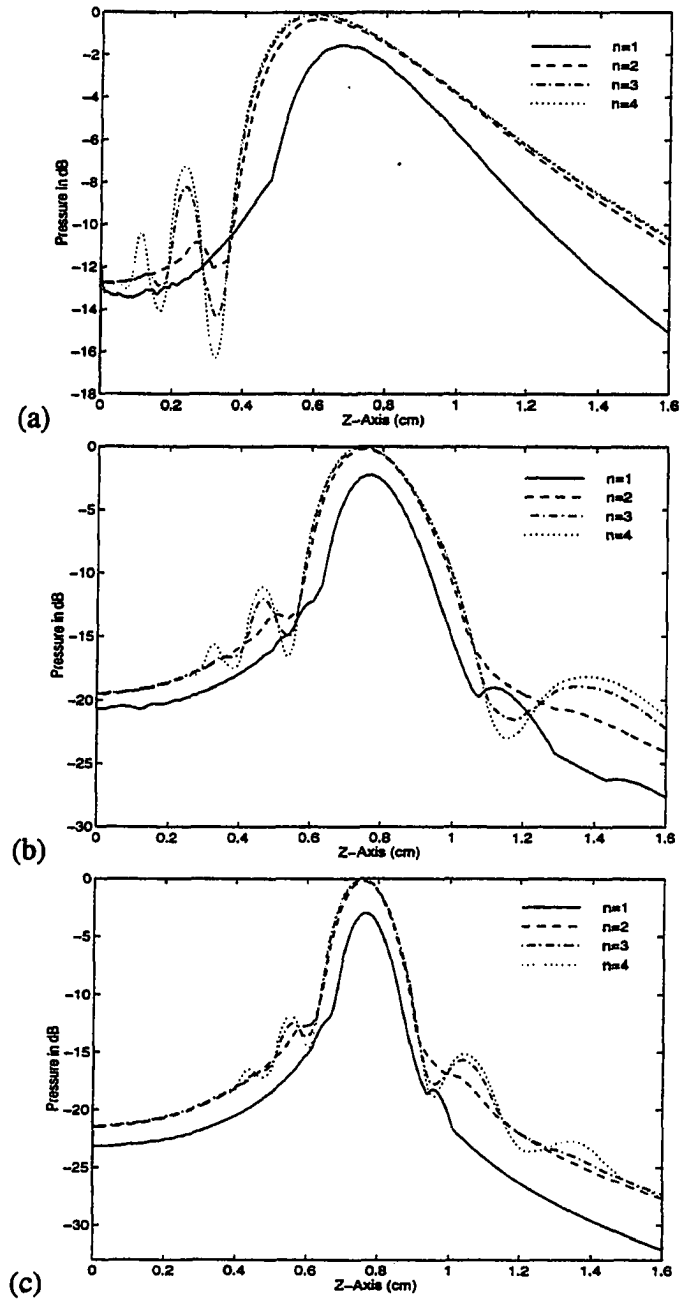

Figure 6.22: Normalized axial pressure fields, (a) array 1, (b) array 2, and (c) array 3, with four different excitations in each case.

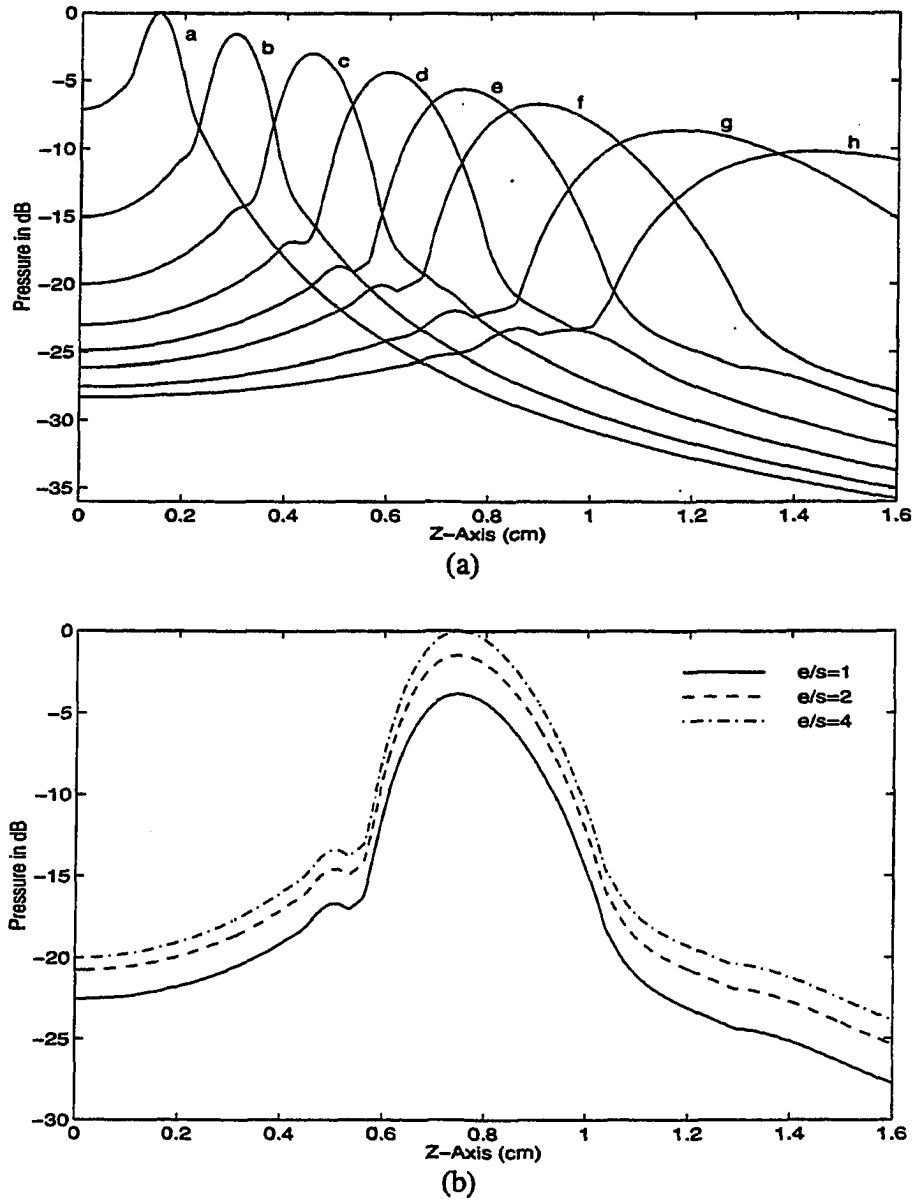

Figure 6.23: Axial pressure fields (array 2 with n=2) based on the variation of (a) focal length, (b) element width/spacing ratio.

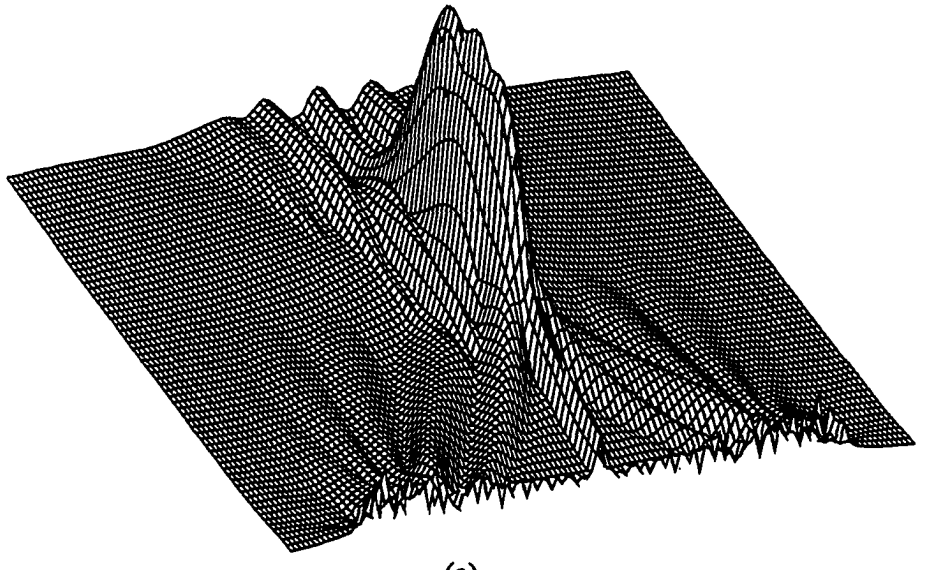

(a)

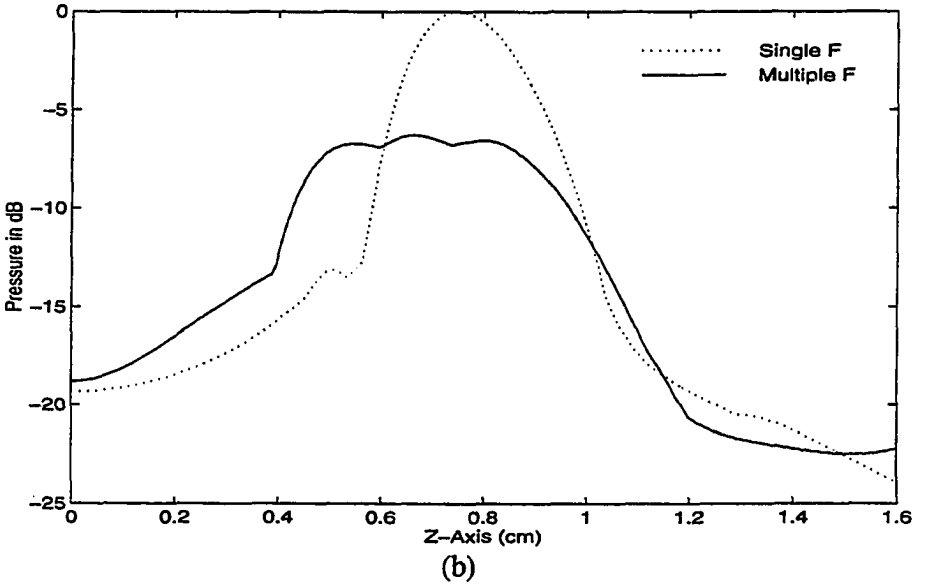

(b)

Figure 6.24: Fields (array 2 with n=2) due to multiple focusing, (a) field profile, (b) axial pressure field compared with single focusing.

CHAPTER 7. WAVE ANALYSIS IN ACOUSTIC MICROSCOPY

An overview of the scanning acoustic microscope has been given in Chapter 1. In addition to imaging purposes, the acoustic microscope can be operated in the non-scanning fashion to determine the elastic properties of materials based on two types of measurements. One is the V(z) curve or acoustic material signature (AMS) [106,107] and the other is the time-resolved measurement [95,108,109]. The V(z) curves obtained by using relative longer pulses not only provide the foundation of the image contrast mechanism of the SAM but also contain information on the leaky Rayleigh wave velocity and attenuation information, as well as the status of defects if there are any involved. By using relatively short excitation pulses, the different wave fronts can be resolved in the time domain and provide pertinent information regarding the sample. Various models have been proposed to illustrate the phenomena and serve as tools for interpreting measurement data. Based on the angular spectrum approach from Fourier optics, Atalar [110,111] derived a simple formulation of the V(z) curves which were subject to paraxial approximation. The key parameter relating to the material property is the reflection function at the coupling medium/sample interface. A similar approach but for the line-focus acoustic microscope has been given by Kushibiki et al. [112,113]. A Fourier spectrum model for surface cracks is given by Somekh et al. [114]. The effects of large angles of beam convergence on the V(z)

curve have been formulated by Sheppard and Wilson [115]. A ray interpretation of the AMS is provided by Parmon and Bertoni [94]. A prediction of the period of the oscillating curve has been given and the approach indicates that the interference of two groups of rays contributes to the voltage output. One group includes specularly reflected rays close to the axis of symmetry. The others are rays radiated back to the coupling medium at the Rayleigh critical angle (particularly the ones symmetric with the input rays at the Rayleigh angle incidence) from the leaky Rayleigh waves excited at the sample surface. More quantitative prediction of the AMS based on the ray representation has been given by Bertoni [116] for the case of leaky Rayleigh waves where the Rayleigh wave velocity in the sample is significantly greater than the compressional wave in the coupling medium, and by Chan and Bertoni [117] for the case of lateral longitudinal waves which occur when the Rayleigh wave velocity is smaller than the compressional wave velocity in the coupling medium. An alternative to the traditional lens for focusing the acoustic beam is the spherical or concave transducer[118,119]. This kind of focusing transducer has the advantage of no aberration, no spurious reflection, as well as low cost of fabrication. The V(z) curves show significant difference from those of the acoustic lens [119,120]. As indicated by Sugawara, et al [120], the amplitude of the V(z), in the defocused region, shows rapid periodic variation not directly associated with the surface Rayleigh wave velocity whereas the phase is related to the surface Rayleigh wave. The nonparaxial formulation of V(z) and its Fourier transform relation with the reflection function at the fluid/sample interface are given by Liang et al. [121] for the spherical transducer, and the measurement data for both the magnitude and phase of the V(z) curve can be inverted to yield the reflection function which is strongly dependent on material

properties. Material characterization using the line-focus-beam acoustic microscope, which overcomes the deficiency of the spherically focused acoustic microscope for anisotropic materials, has been covered in detail in [122] where the wave propagation properties such as the phase velocity and attenuation of the leaky surface acoustic wave were determined based on the V(z) curve analysis. The V(z) formulation for the line-focus acoustic microscope based on the boundary element method has been reported by Achenbach et al. [123]. The approach has also been used to derive the response to surface-breaking and subsurface cracks [124,125]. A formulation based on the Fourier integral /boundary integral approach has been presented by Roberts [126] for the acoustic microscope response to the scattering by a near-surface void. A combined finite element and Green's function approach for simulating the focusing properties of the spherical acoustic lens has been carried out by Winkler and Davies [127]. They demonstrated the discrepancy between their numerical model and the classical ray approach for thick lenses. Latest developments in acoustic microscopy, including time-resolved measurements of short cracks, novel lens geometries, elastic constants measurements for bulk materials and thin films, etc., has been covered in [128]. In this chapter, a finite element model is developed for analyzing the ultrasonic pulses propagating in the acoustic microscope.

Fields of the Spherically Curved Transducer

Fig. 7.1 shows the geometry for modeling the spherically curved transducer, where $2a$=0.36 cm. The excitation signal is in the form of Eq. (4.1) with a center frequency of 5 MHz. Fig. 7.2 displays the transient wave profiles for the curved transducer. The focusing effect is clearly indicated and the maximum field is achieved at

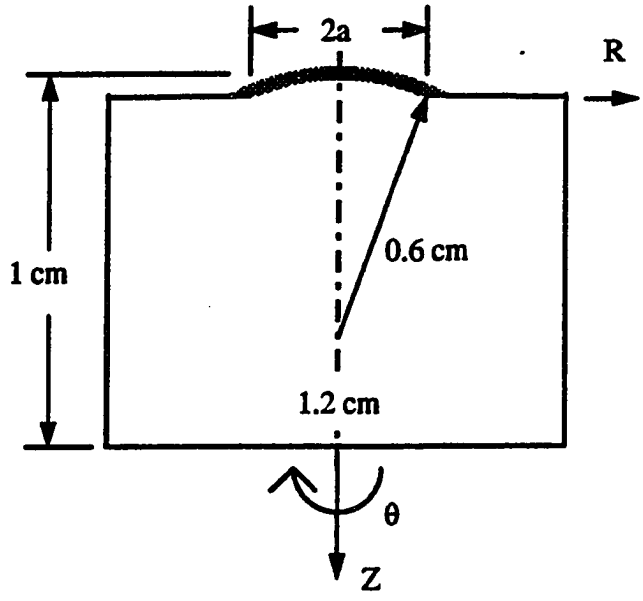

Figure 7.1: Axisymmetric configuration for the curved transducer.

around 4 microseconds. Fig. 7.3 shows the spatial distribution of the normalized fields for the three excitation pulses. There exist significant differences in the nearfields but the farfields (i.e., beyond the focal point) are almost identical. For comparison, the corresponding field distributions for a flat transducer with the same aperture diameter are shown in Fig. 7.4. The focusing property of the curved transducer is further indicated by the axial fields displayed in Fig. 7.5. It is indicated that the true focal point is around 0.48 cm from the transducer which is smaller than the geometrical focal distance fg=0.6 cm. This is explained by the diffraction effect of the curved transducer(2). Fig. 7.6 shows the transverse field in the geometrical focal plane for the different excitations from which it can be seen that shorter pulses or wider bandwidths correspond to greater smoothness of the fields. The CW curve in Fig. 7.6 is

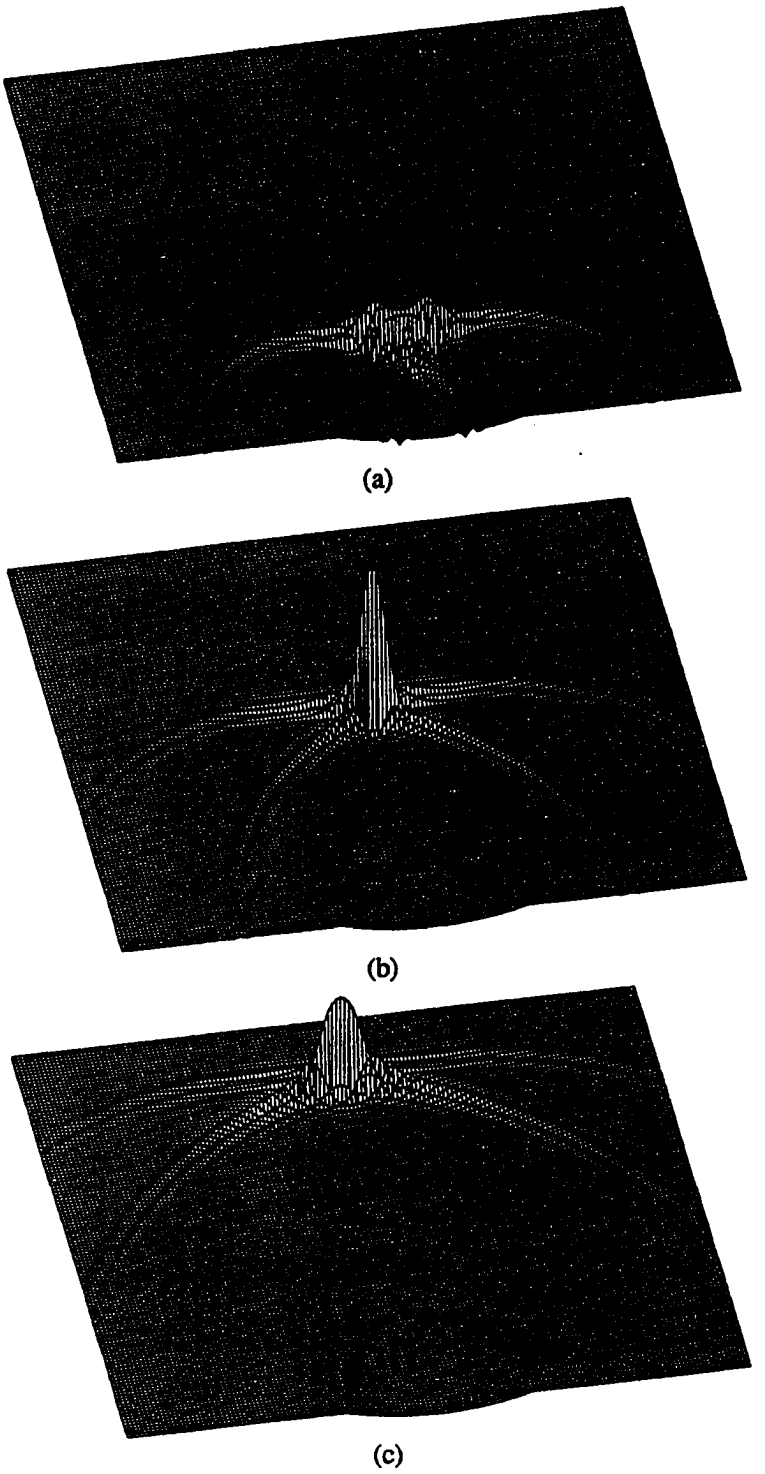

Figure 7.2: Wave profiles for the curved transducer with excitation pulse 1, (a) t=2 μs, (b) 4 μs and (c) 6 μs.

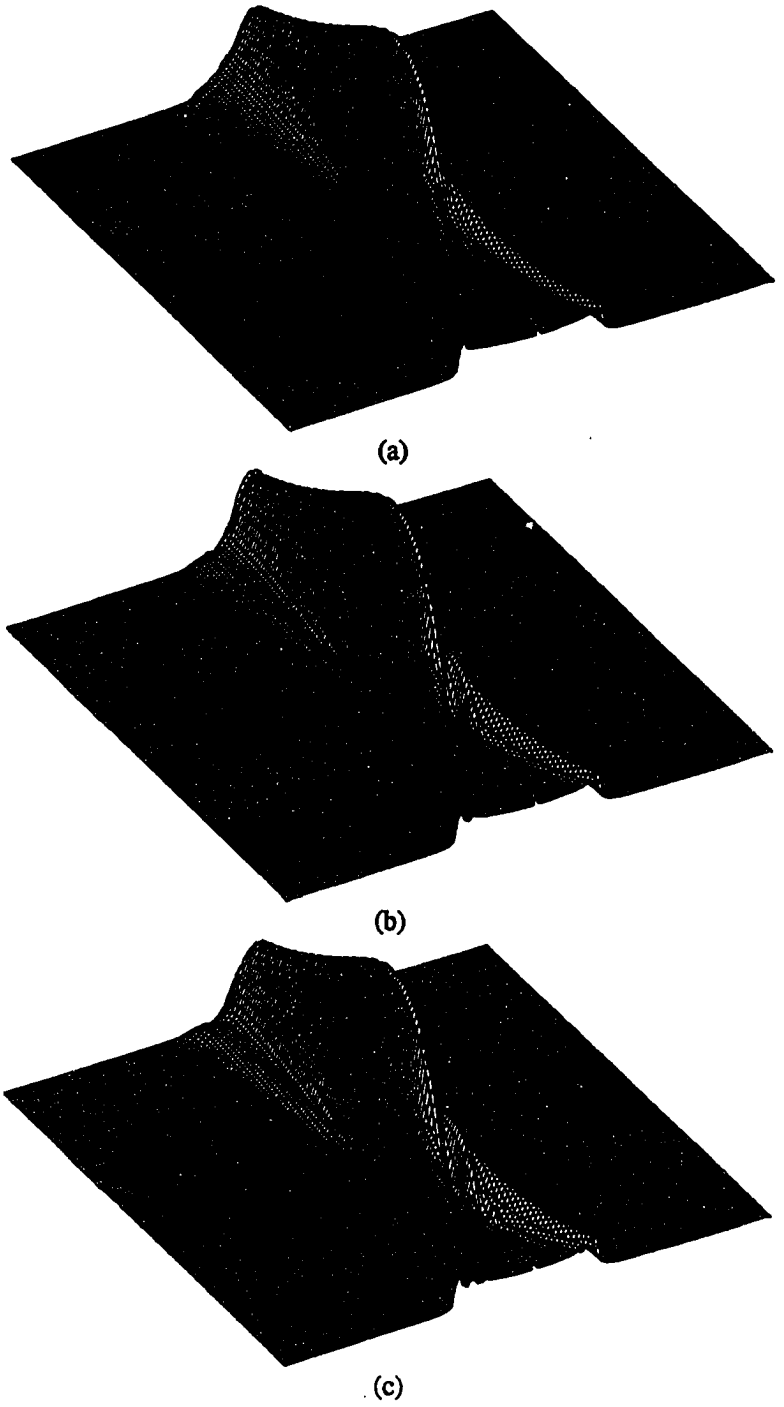

Figure 7.3: Field profiles for the curved transducer for excitation (a) pulse 1 (b) pulse 2 and (c) pulse 3.

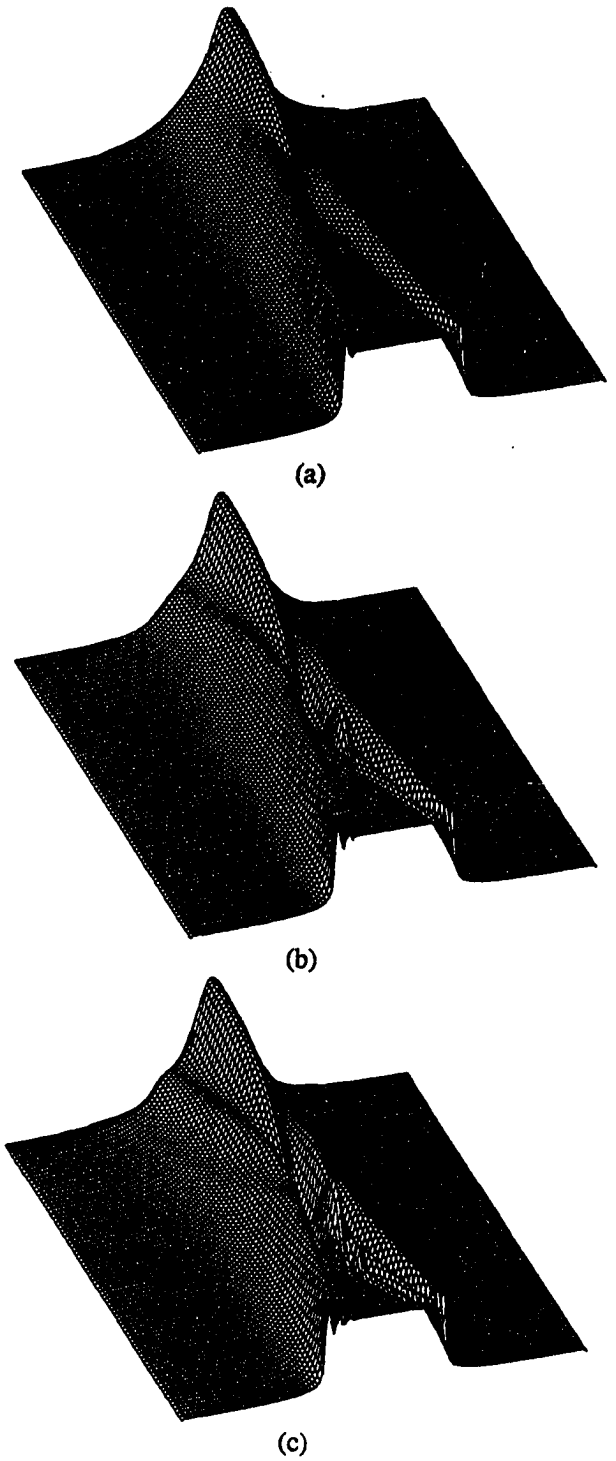

Figure 7.4: Field profiles for the planar transducer for excitation (a) pulse 1 (b) pulse 2 and (c) pulse 3.

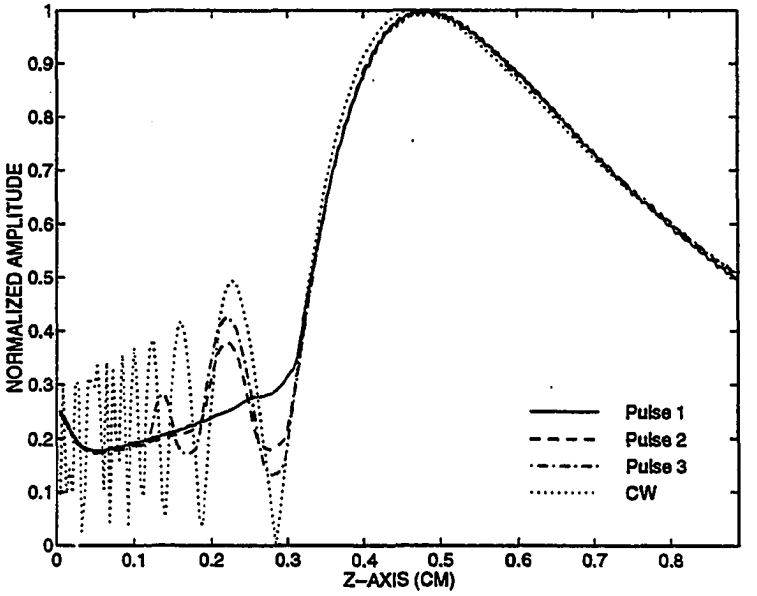

Figure 7.5: Axial field for the curved transducer.

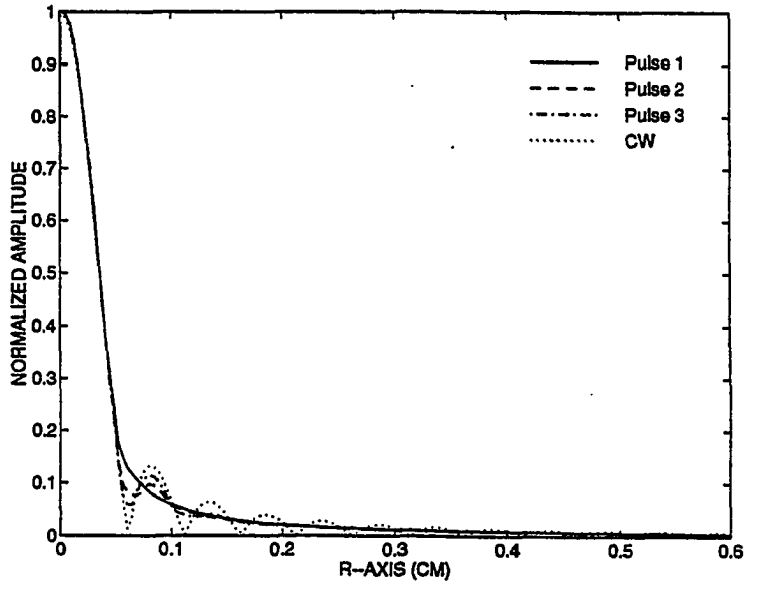

Figure 7.6: Transverse field in the geometrical focal plane for the curved transducer.

equivalent to that in the Fraunhofer region of a flat transducer [85].

Modeling of the Spherical Lens

The lens structure is taken as an axisymmetric aluminum/water cylinder with diameter of 1 cm. The lens radius of curvature is 0.5 cm. Both the transducer and the lens aperture have a diameter of 0.4 cm. The total length of the geometry is 2.25 cm with the thickness ratio of the two media on the axis is 2:1. The driving signal for the transducer is assumed to be a standard raised cosine with center frequency of 5 MHz. The time dependent wave profiles in the lens are shown in Fig. 7.7. The potential wave fields in the fluid have been normalized such that their magnitude is of the same order as the displacement in the lens rod. The fields inside the lens rod are described in Chapter 4. The focusing properties of the lens are clearly illustrated. The field amplitude distribution in water is shown in Fig. 7.8. It is shown by plotting only the axial field that the peak point on the axis is 0.65 cm from the lens surface. This is larger than the radius of curvature and agrees with the prediction of paraxial ray theory.

Focused Fields Probing a Fluid/Solid Interface

In this case a spherical transducer with aperture diameter of 1 cm and curvature radius of 1.5 cm radiates a focused wave of 5 MHz center frequency into the water/aluminum assembly. The two layers have thickness of 0.4 cm and 0.8 cm respectively. The wave profiles are shown in Fig. 7.9. Since in this configuration the maximum half angle is 19.47 degrees which is about 10 degrees less than the Rayleigh critical angle, no leaky Rayleigh waves are generated on the interface. The

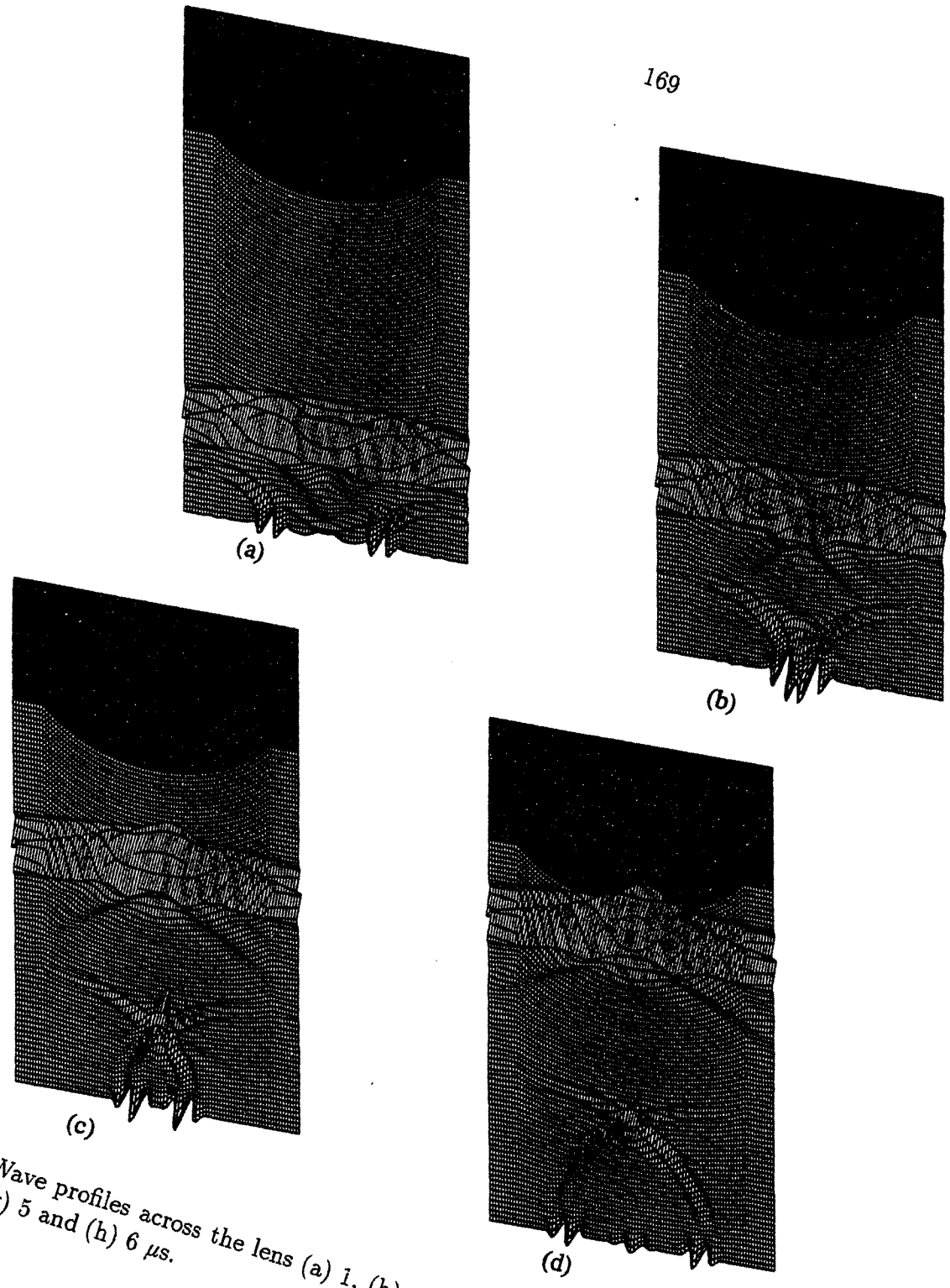

Figure 7.7: Wave profiles across the lens (a) 1, (b) 1.5, (c) 2, (d) 2.5, (e) 3, (f) 4, (g) 5 and (h) 6 μs.

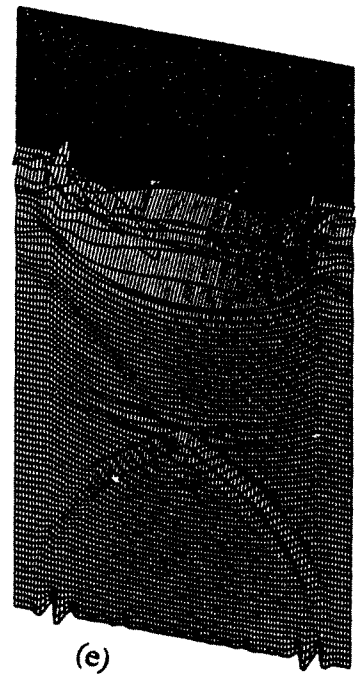

(e)

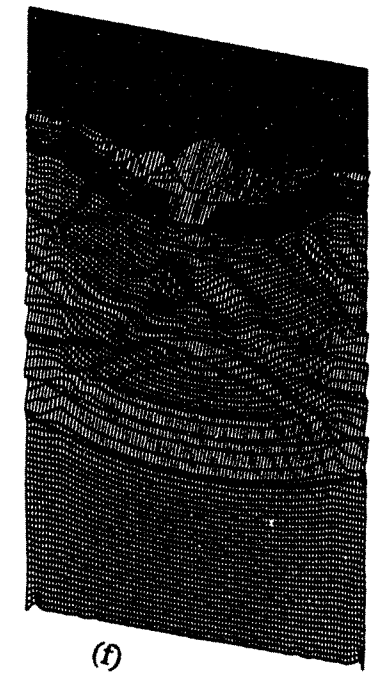

(f)

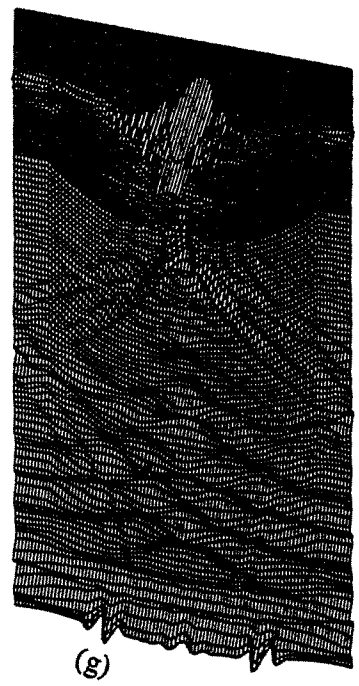

(g)

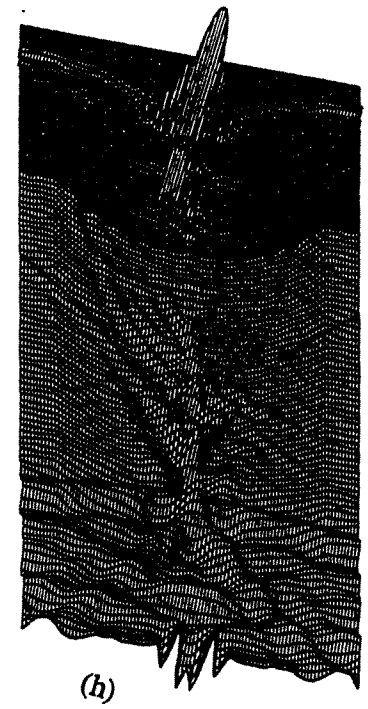

(h)

Figure 7.7 *(Continued)*

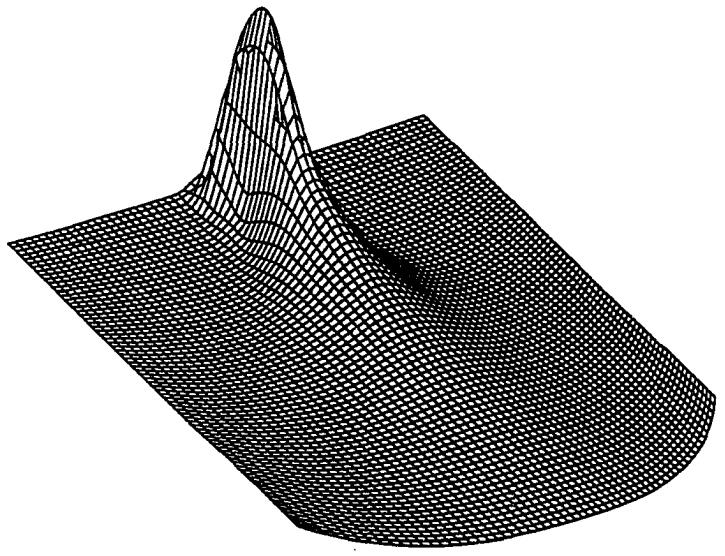

Figure 7.8: Focused wave field distribution in the fluid medium.

transmitted waves include both shear and longitudinal waves. Besides the specularly reflected waves there exist also lateral longitudinal waves propagating back in the fluid medium. This corresponds to one of the cases considered in Chapter 5 where other cases are also treated in detail.

Focused Fields Probing a Solid/Solid Interface

In this study, the acoustic microscope is modeled by the geometries shown in Fig. 7.10, which consists of a coupling medium(V_l=1500 m/s, V_S=800 m/s, ρ=1000 kg/m^3) and a ceramic sample (V_l=9400 m/s,V_S=5640 m/s, ρ=3970 kg/m^3). A raised cosine excitation signal with center frequency of 20 MHz is applied uniformly over the spherical surface. Fig. 7.10(a) differs from (b) in that they represent different

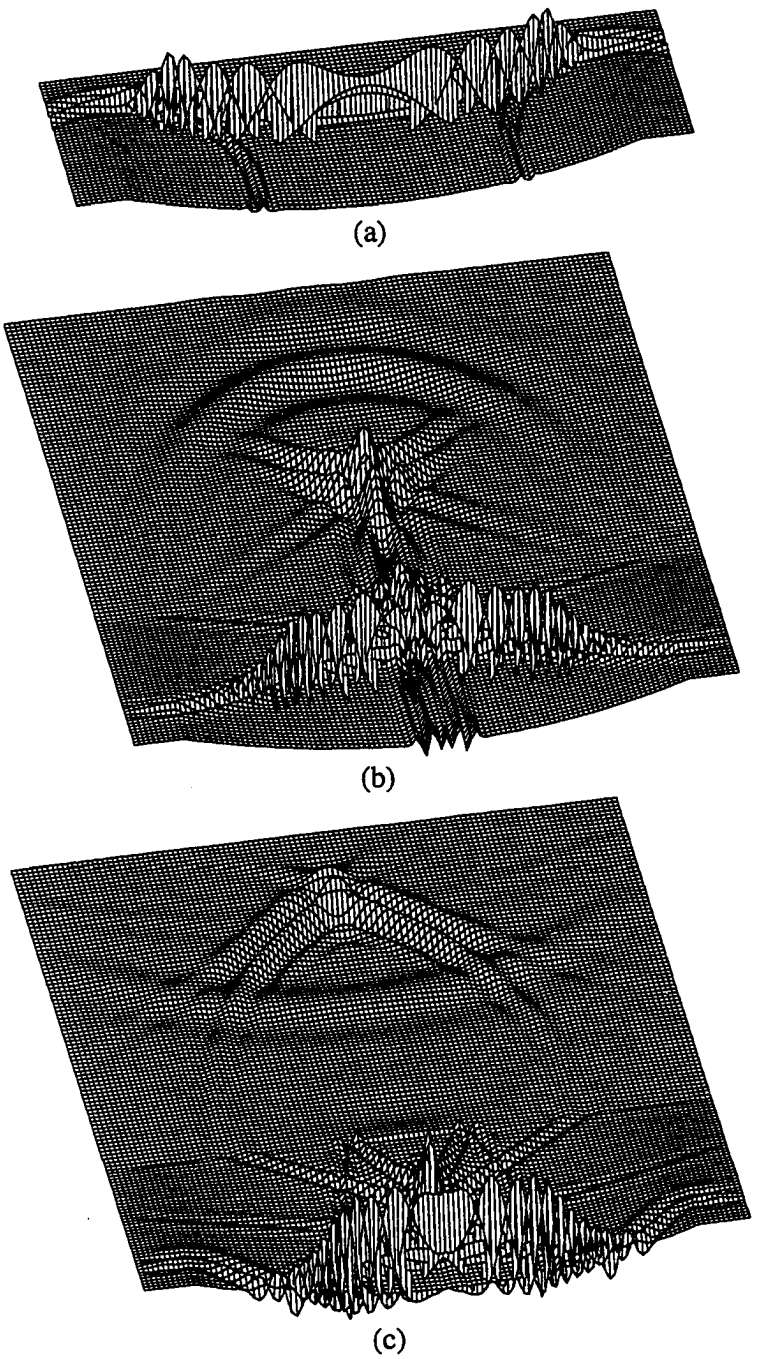

Figure 7.9: Profiles of waves from a spherically focused transducer probing a fluid/solid interface, (a) 2, (b) 4 and (c) 5 μs.

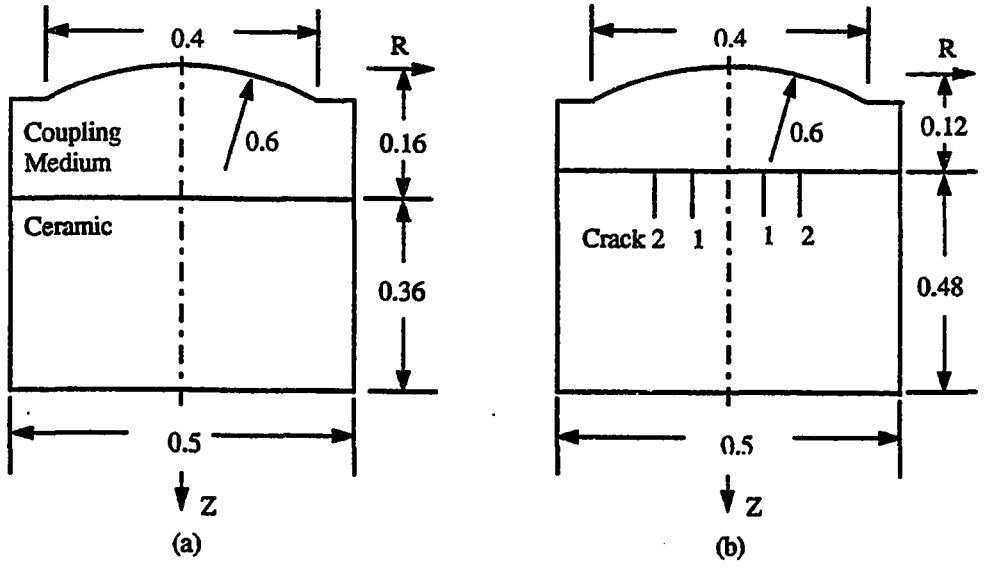

Figure 7.10: Axisymmetric geometries for modeling the acoustic microscope. The length values are in centimeters.

defocusing and the latter configuration includes three cases: without crack, with crack 1 at radial distance r=0.05cm, and with crack 2 at r=0.1 cm, respectively. The thickness of the crack is only a few percent of the longitudinal wavelength in the sample.

Fig. 7.11 displays the wave profiles (Z-displacement) for the configuration in Fig. 7.10(a) at (a) t=1.25, (b) t=1.5 and (c) t=1.75 μs, respectively. At t=1.25 μs, the focused wave front reaches the planar interface and reflects back to the coupling medium. A refraction also occurs. In addition, it can be observed that a Rayleigh wave also propagates along the interface towards the axis of symmetry. It could

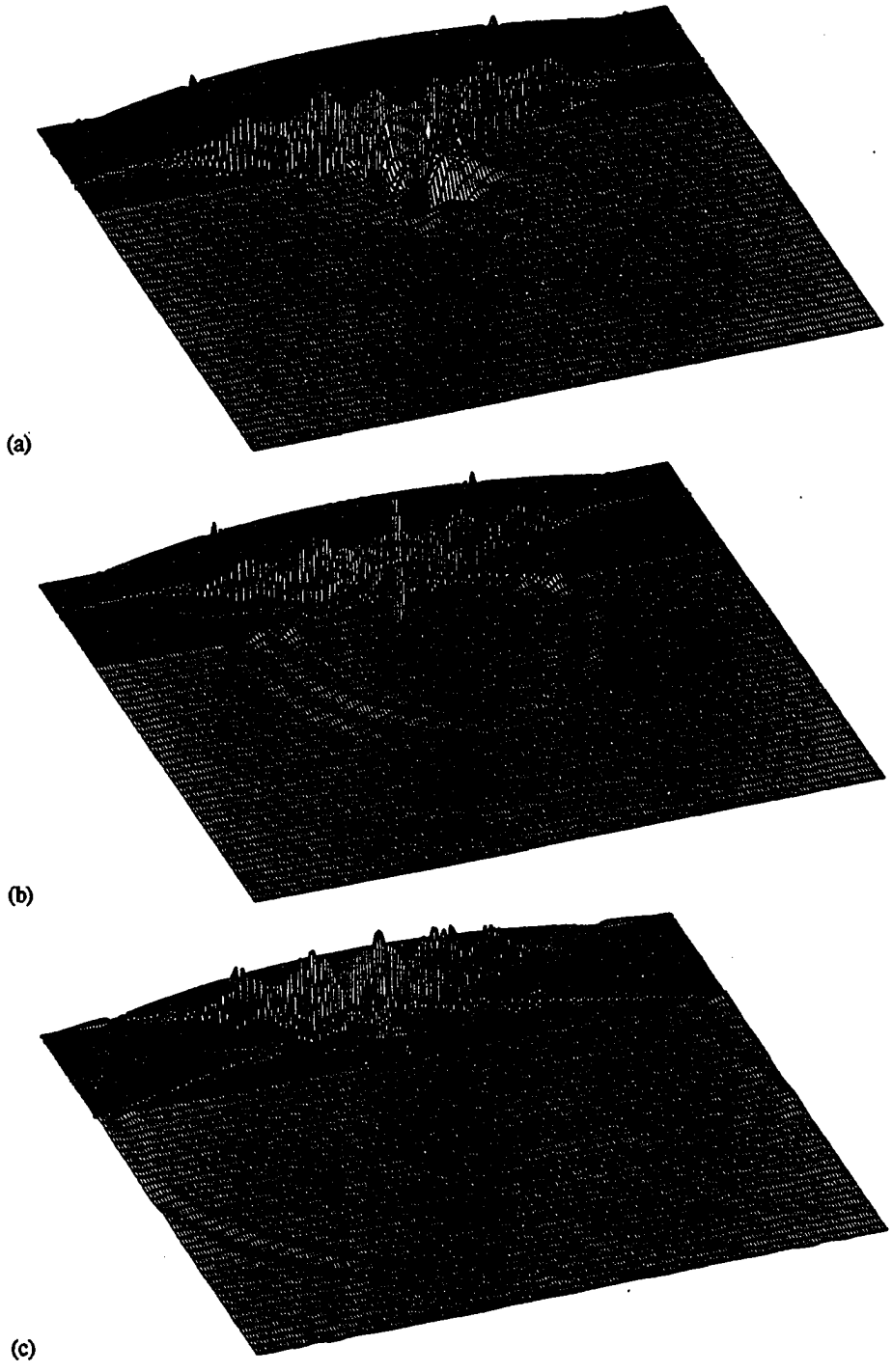

Figure 7.11: Wave profiles for the configuration in Fig. 7.10(a), (a) t=1.25 μs, (b) t=1.5 μs and (c) t=1.75 μs.

be due to that part of the focused beam incident to the interface at or around the Rayleigh angle. The profiles at t=1.5 and 1.75 μs indicate that the Rayleigh wave propagates away from the axis and decreases in magnitude. Associated with this wave there is another wave front propagating back to the coupling medium. Fig. 7.12 shows the transient wave fields at different spatial points for the same geometry. The left column, i.e., Fig. 7.12(a), is for points on the curved surface. There are four major pulses. In the middle plot, for example, the first pulse is the initially excited Z-displacement, the second is a surface Rayleigh wave from the transducer edge, the third is a specular reflection from the planar interface and the fourth one is the wave front excited from the interface Rayleigh wave. The right column, i.e., Fig. 12(b), is for points on the planar interface and two major wave components are indicated. Near the axis of symmetry, the Rayleigh waves propagating inward and outward are just separated. Farther form the axis, the two waves are significantly separated. Beyond some point only the outward propagating Rayleigh wave exists as indicated in the third plot. From these plots, the Rayleigh wave velocity is estimated to be 5200 m/s which is in agreement with the analytical value.

Fig. 7.13 shows the wave profiles at t=1 μs for the geometry in Fig. 7.10(b), (a) without crack, (b) with crack 1 at r=0.05 cm and (c) with crack 2 at r=0.1 cm on the sample surface. The comparison of Fig. 7.13(a) and Fig. 7.11(a) indicates similar wave mechanisms with only a time shift due to different negative defocusing. It is seen from Figs. 7.13(b) and (c) that when the excited Rayleigh wave propagates toward the axis and reaches the crack, it is reflected back and propagates along the interface towards the edge. It is also noted that an associated longitudinal wave front propagates back to the coupling medium. Fig. 7.14 compares the transient

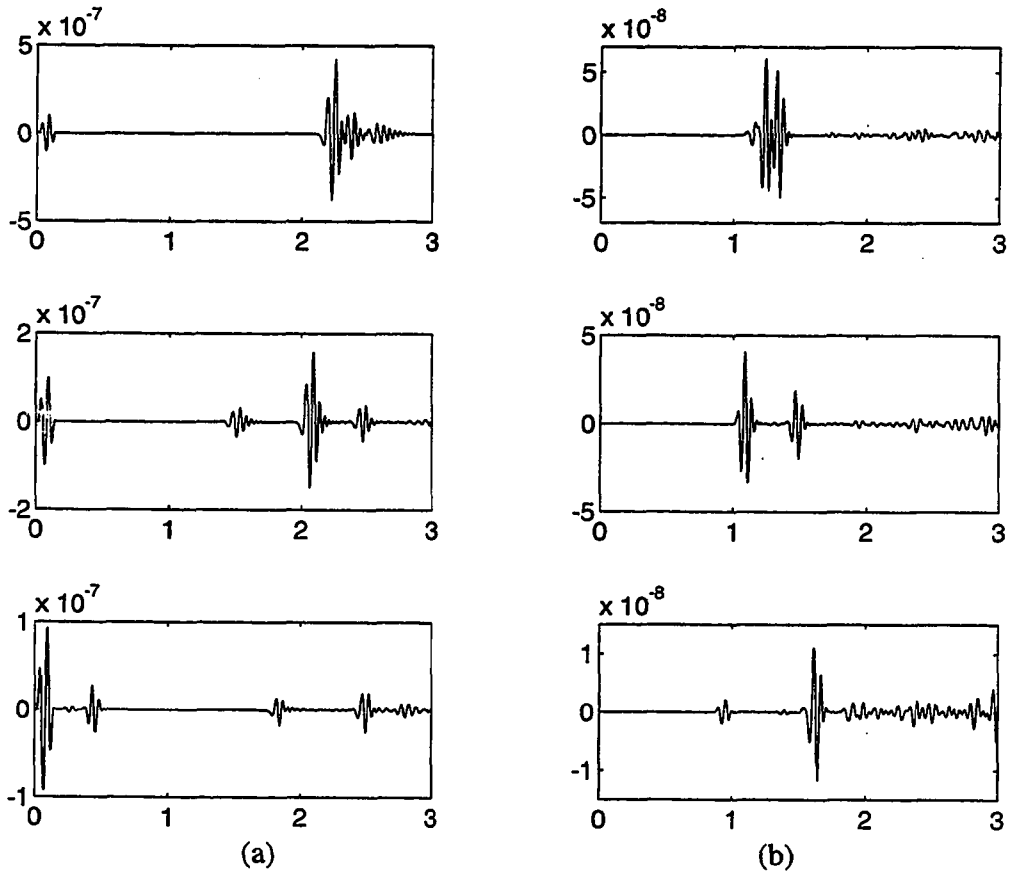

Figure 7.12: Transient wave fields for the configuration in Fig. 7.10(a), (a) on the curved surface, (b) on the planar interface. The three plots in each column are for radial locations r=0.025, 0.1 and 0.175 cm, respectively. The vertical axis is Z-displacement and the horizontal axis is time in microseconds.

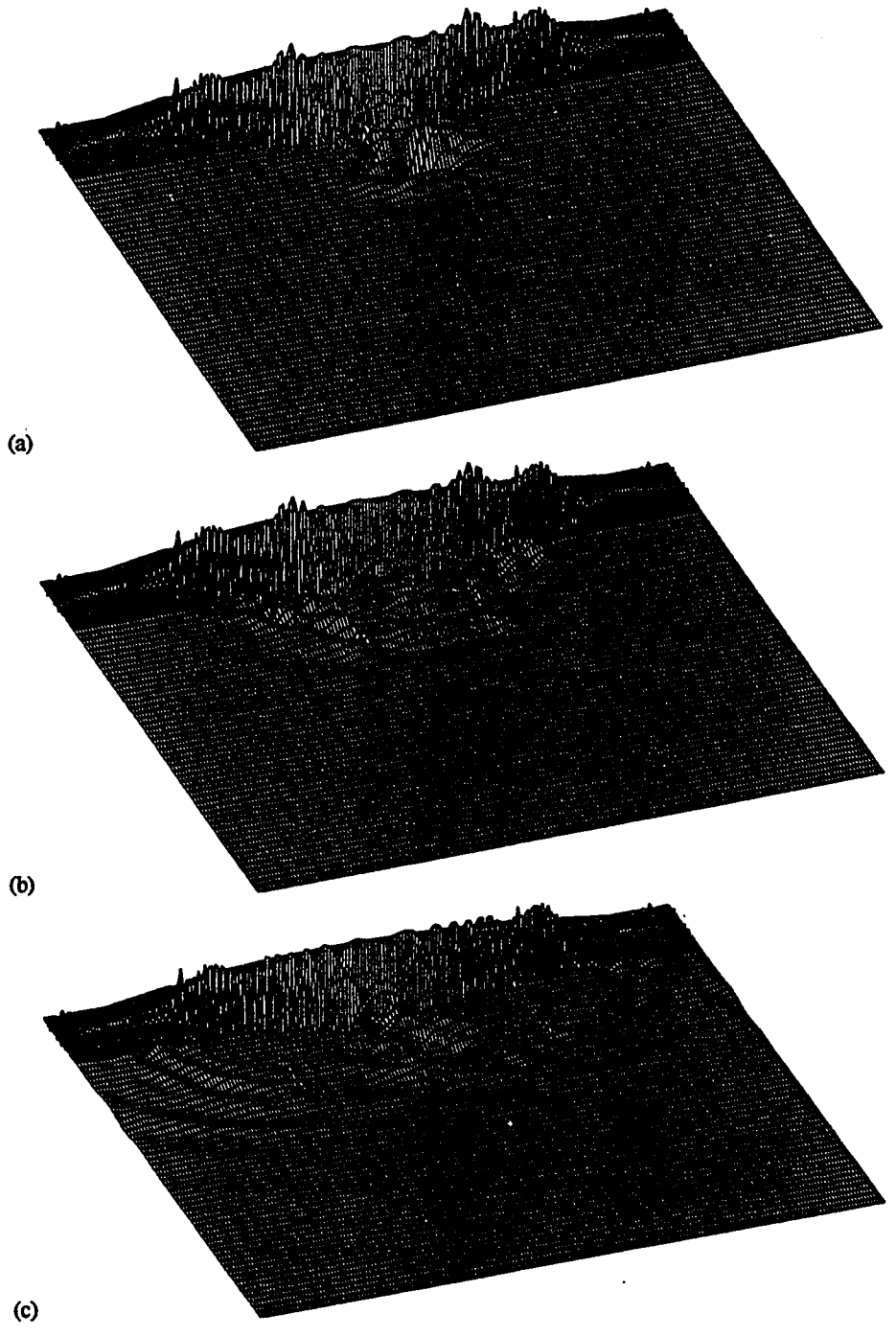

Figure 7.13: Wave profiles for the configuration in Fig. 7.10(b) at t=1 μs, (a) without crack, (b) with crack 1 only and (c) with crack 2 only.

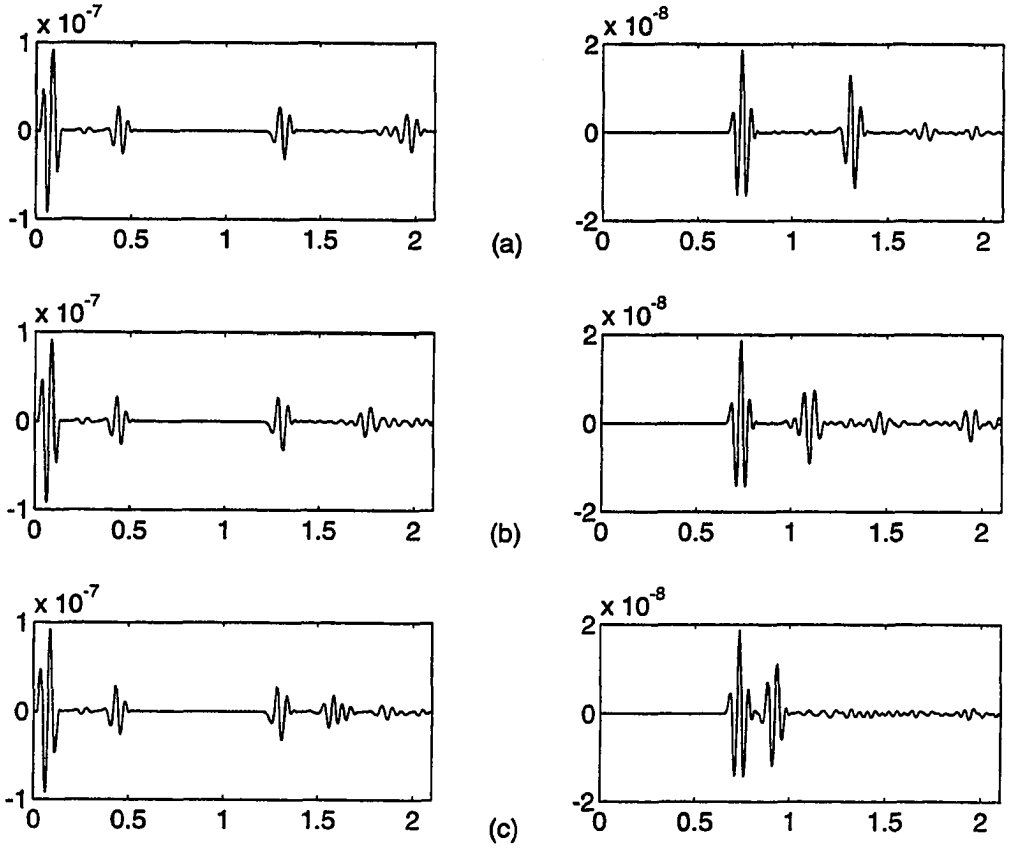

Figure 7.14: Transient wave fields for configuration (b) in Fig. 7.10. (a) Without crack, (b) with crack 1, and (c) with crack 2. The left plot in each case is for radial location r=0.175 cm on the curved surface and the right plot is for radial location r=0.15 cm on the planar interface. Axis labels are the same as in Fig. 7.12.

wave fields for the geometry in Fig. 7.10(b) without or with cracks. It is seen from the left column that when the crack position is farther from the axis (if not out of the Rayleigh angle limit), the time it takes will be shorter for the wave front radiated back to the coupling medium from the interface Raleigh wave to reach the curved surface since the then reflected path to the surface is shorter. The wave fields in column (b) confirm that it takes less time for the interface Rayleigh wave to reach the specified point with the presence of crack 2 which is farther away from the axis than crack 1.

As a summary, the wave fields in an acoustic microscope are analyzed using the finite element method. The results agree with the established analytical formulations. When the spherically focused beam reaches the interface of the coupling medium and the sample, an interface Rayleigh wave, typically called the leaky Rayleigh wave, will be excited along the interface provided that the beam contains rays around the Rayleigh angle. This wave reradiates a longitudinal wave back to the coupling medium. As the leaky Rayleigh wave reaches a crack in its path both reflection and reradiation occur.

CHAPTER 8. CONCLUSIONS

In this study, a finite element model is developed to simulate ultrasonic wave propagation in acoustic and elastic media with application to acoustic microscopy. Based on the governing equations from dynamic elasticity, semi-discretized finite element equations in the space domain are derived according to the variational principle. Direct time integration is carried out through the explicit central difference scheme. Both linear and quadratic elements are implemented with comparison and verifications. While the full 3D implementation consumes enormous computer resources in terms of memory and CPU time, the major results are based on the 2D and axisymmetric geometries. Material properties, including anisotropy, inhomogeneity, viscous damping and arbitrary discontinuities are handled successfully by the model.

Acoustic media are readily handled through the pressure analog approach. For ultrasonic systems containing a fluid/solid interface, the governing equations for both the solid and fluid media have to be solved simultaneously with the interfacing boundary conditions properly satisfied. In this case the solid and fluid media are formulated by the displacement vector and pressure scalar respectively. The coefficient matrices are rendered symmetric by introducing a new potential variable for the fluid medium.

The transient fields of a pulsed transducer in an isotropic medium are characterized by the finite element model. Various wave fronts are predicted, including the

direct longitudinal wave, edge longitudinal wave, edge shear wave, Rayleigh surface wave and head wave. The phase relationships among these waves are in agreement with the literature. The interaction of the finite aperture transducer fields with spherical voids and penny-shaped cracks are presented. Forward and backward scattered wave as well as creeping waves are successfully predicted. Wave mode conversions are implicitly built in the model.

The fields of spherically focused transducers and time-delay arrays are analyzed. The wave field profiles are compared with those obtained by the classical impulse response method and good agreement is achieved. One feature of the impulse response method is that it allows the transient fields of specific points of interest to be determined without having to work on other points, while the advantage of the finite element method is that it is able to determine the overall fields of a certain spatial region of interest with a greater efficiency.

The generation and propagation properties of transient leaky Rayleigh waves are characterized and visualized by the finite element model. Wave propagation in an acoustic lens and focused waves probing a fluid/solid and solid/solid interfaces as situations in acoustic microscopy are presented. Scattering characteristics of surface and subsurface cracks in acoustic microscopy are examined quantitatively. The effects of excitation pulse bandwidths are presented in the majority of simulations. The finite element model proves to be an invaluable tool for acoustic device design and material characterization.

A few comments on possible future work are in order. (1) For the realistic acoustic microscope, a coupled FEM/BEM formulation may be beneficial for efficient computations. While the solid part can be modeled by the FEM, the coupling

medium of the extended region can be modeled by the BEM. (2) Comparisons can be made for the characteristics for various focusing systems as well as lens structures. Harmonic analysis may be carried out by implementing infinite elements. (3) A three dimensional model can be implemented based on cylindrical coordinates. Particular interest lies in the NDE of tubes and pipelines where the load or geometry may not be exactly axisymmetric. (4) The finite element codes can be further optimized for parallel processing on supercomputers to improve execution efficiency and to simulate problems of larger size or greater complexity.

BIBLIOGRAPHY

[1] R. B. Thompson and D. O. Thompson, "Ultrasonics in nondestructive evaluation," *Proceedings of the IEEE*, Vol. 73, pp. 1716-1755, 1985.

[2] J. Krautkramer and H. Krautkramer, *Ultrasonic Testing of Materials*, 4th Edition, Springer-Verlag, Berlin, 1990.

[3] A. Briggs, *Acoustic Microscopy*, Clarendon Press, Oxford, 1992.

[4] B. T. Khuri-Yakub, "Scanning acoustic microscopy," *Ultrasonics*, Vol. 31, No. 5, pp. 361-372, 1993.

[5] C. F. Quate, A. Atalar and H. K. Wickramasinghe, "Acoustic microscopy with mechanical scanning," *Proceedings of the IEEE*, Vol. 67, pp. 1092-1114, 1979.

[6] Lemons, R. A., and C. F. Quate, "Acoustic microscopy," in *Physical Acoustics*, Vol. 14, eds. W. P. Mason and R. N. Thurston, Academic Press, London, pp 1-92, 1979

[7] G. A. Gorden, S. Canumalla and B. R. Tittmann, "Ultrasonic C-scan imaging for material characterization," *Ultrasonics*, Vol. 31, No. 5, pp. 373-380, 1993.

[8] J. J. Bowman, T. B. A. Senior and P. L. E. Uslenghi, *Electromagnetic and Acoustic Scattering by Simple Shapes*, North Holland, Amsterdam, 1969.

[9] R. M. White, "Elastic wave scattering at a cylindrical discontinuity in a solid," *Journal of the Acoustic Society of America*, Vol. 30, pp. 771-785, 1958.

[10] C. F. Ying and R. Truell, "Scattering of a plane longitudinal wave by a spherical obstacle in an isotropically elastic solid." *Journal of Applied Physics*, Vol. 27, p. 1086, 1956.

[11] L. Filipczynski, "Scattering of a plane longitudinal wave on a free surface of a disc in a solid medium." *Proceedings of Vibration Problems*, Vol. 2, pp. 41-54, 1961.

[12] Y-H Pao and C. C. Mow, *Diffraction of elastic waves and dynamic stress concentrations*, Crane and Russak, New York, 1973.

[13] J. E. Gubernatis, E. Domany, J. A. Krumhansl and M. Huberman, "The Born approximation in the theory of the scattering of elastic waves by flaws." *Journal of Applied Physics*, Vol. 48, p. 2812, 1977.

[14] J. H. Rose and J. L. Opsal, "The inverse Born approximation: exact determination of shape of convex voids," in *Review of Progress in Quantitative NDE*, Vol. 2B, eds. D. O. Thompson and D. E. Chimenti, p. 949, Plenum Press, New York, 1983.

[15] C. J. Bowkamp. "Diffraction theory," *Reports on Progress in Physics*, Vol. 17, p. 35, 1954.

[16] J. M. Coffey and R. K. Chapman, "Application of elastic scattering theory for smooth flat cracks to the quantitative prediction of ultrasonic defect detection and sizing." *Nuclear Energy*, Vol. 22, pp. 319-333, 1983.

[17] J. B. Keller, "Geometrical theory of diffraction," *Journal of the Optical Society of America*, Vol. 52, pp. 116-130, 1962.

[18] J. D. Achenbach, A. K. Gautesen and H. McMaken. *Ray Methods for Waves in Elastic Solids*, Pitman, Boston, 1982.

[19] P. C. Waterman, "Matrix theory of elastic wave scattering." *Journal of the Acoustic Society of America*, Vol. 60, p. 567, 1976.

[20] V. K. Varadan and V. V. Varadan, eds. *Acoustic, Electromagnetic and Elastic Wave Scattering – Focus on the T-Matrix Approach*, Pergamon, New York, 1980.

[21] W. M. Visscher, "A new way to calculate scattering of acoustic and elastic waves," *Journal of Applied Physics*, Vol. 51, p. 2, 1980.

[22] A. T. de Hoop, "A modification of Cagniard's method for solving seismic wave problems," *Applied Scientific Research*, Vol. B8, pp. 349-365, 1959.

[23] Z. S. Alterman and D. Loewenthal, "Computer generated seismograms," in *Methods in Computational Physics*, Vol. 12 ed. B. A. Bolt, Academic Press, New York, 1972.

[24] K. Harumi, F. Suzuki and Y. Saito (1973), "Computer simulation of nearfield for elastic wave in a solid half-space." *Journal of the Acoustic Society of America*, Vol. 53, pp. 600-664, 1973.

[25] J. L. Rose and P. A. Meyer, "Model for ultrasonic field analysis in solids," *Journal of the Acoustic Society of America*, Vol. 57, pp. 598-605, 1975.

[26] L. J. Bond. "Methods for the computer modeling of ultrasonic waves in solids." *Research Techniques in NDT*, Vol. 6, ed. R. S. Sharpe, Academic Press, New York, 1982.

[27] L. J. Bond, M. Punjani, and N. Saffari, "Ultrasonic wave propagation and scattering using explicit finite difference methods," in *Mathematical Modeling in NDT*, eds. M. Blakemore and G. A. Georgiou, Clarendon Press, Oxford, pp 81-124, 1988.

[28] P. P. Desalto, R. S. Schechter, H. H. Chaskelis, R. B. Mignogna, R. Kline, "Connection machine simulation of ultrasonic wave propagation in materials, II: The two dimensional case," *Wave Motion*, Vol. 20, pp. 295-314, 1994.

[29] J. Lysmer and L. A. Drake, "A finite element for seismology." *Methods in Computational Physics*, Vol. 11, ed. B. A. Bolt, Academic Press, New York, 1972.

[30] W. D. Smith, 'The application of finite element analysis to body wave propagation problems." *Geophysical Journal of the Royal Astronomical Society*, Vol. 42, p.68, 1975.

[31] O. C. Zienkiewicz and R. E. Newton, "Coupled vibrations of a structure submerged on a compressible fluid," *Symposium on Finite Element Techniques* Stuttgart, Germany, 1969

[32] A. Craggs, "The transient response of a coupled plate-acoustic system using plate and acoustic finite elements," *Journal of Sound and Vibration*, Vol. 15, pp. 509-528, 1971.

[33] O. C. Zienkiewicz. and R. L Taylor, *The Finite Element Method*, 4th Edition, McGraw-Hill, New York, Vol. 1, 1989, Vol. 2, 1991.

[34] Z. P. Bazant, J. L. Glazik and J. D. Achenbach, "Finite element analysis of wave diffraction by a crack." *Journal of the Engineering Mechanics Division*, ASCE, Vol. 102, pp. 479-496, 1976.

[35] R. Ludwig and W. Lord, "The finite element formulation for the study of ultrasonic NDT systems," *IEEE Transactions on Ultrasonics, Ferroelectrics and Frequency Control*, Vol. 35, pp. 809-820, 1988.

[36] R. Ludwig and W. Lord, "A theoretical and numerical study of transient force excitations on an elastic half-space," *IEEE Transactions on Ultrasonics, Ferroelectrics and Frequency Control*, Vol. 36, pp. 342-350, 1989.

[37] W. Lord, R. Ludwig, and Z. You, "Developments in ultrasonic modeling with finite element analysis," *Journal of Nondestructive Evaluation*, Vol. 9, pp. 129-143, 1990.

[38] Z. You, M. Lust, R. Ludwig and W. Lord, "Numerical simulation of ultrasonic wave propagation in anisotropic and attenuative solid materials," *IEEE Transactions on Ultrasonics, Ferroelectrics and Frequency Control*, Vol. 38, pp. 436-45, 1991.

[39] A. Minachi, Z. You, R. B. Thompson, and W. Lord, "Predictions of the Gauss-Hermite beam model and finite element method for ultrasonic propagation through anisotropic stainless steel," *IEEE Transactions on Ultrasonics, Ferroelectrics and Frequency Control*, Vol. 40, pp. 338-346, 1993.

[40] T. Xue, W. Lord and S. Udpa, "Transient fields of pulsed transducers in solids," *Research in Nondestructive Evaluation*, Vol. 7, No. 1, pp. 31-53, 1995.

[41] T. Xue, W. Lord and S. Udpa, "Numerical analysis of the radiated fields of circular pistons and time-delay spherically focused arrays," *IEEE Transactions on Ultrasonics, Ferroelectrics and Frequency Control*, Vol. 43, No. 1, pp. 78-87, 1996.

[42] T. A. Cruse and F. J. Rizzo, "A direct formulation and numerical solution of the general transient elastodynamic problem: I," *Journal of Mathematical Analysis and Applications*, Vol. 22, pp. 244-259, 1968.

[43] F. J. Rizzo, D. J. Shippy and M. Rezayat. "A boundary integral equation method for radiation and scattering of elastic waves in three dimensions." *International Journal of Numerical Methods in Engineering*, Vol. 21, pp. 115-129, 1985.

[44] J.D. Achenbach, *Wave Propagation in Elastic Solids*, North Holland, Amsterdam, 1973.

[45] B. A. Auld. *Acoustic Fields and Waves in Solids*, John Wiley & Sons, New York, 1973.

[46] K. G. Graff, *Wave Motion in Elastic Solids*, Clarendon Press, Oxford, 1975.

[47] C. F. Ying, ed., *Ultrasonics*, Science Press, Beijing, 1989.

[48] K. J. Bathe, *Finite Element Procedures*, Prentice-Hall, Englewood Cliffs, New Jersey, 1996.

[49] D. P. Flanagan and T. Belytschko, "A uniform strain hexahedron and quadrilateral with orthogonal hourglass control," *International Journal of Numerical Methods in Engineering*, Vol. 17, 1981, pp 679-706.

[50] T. J. R. Hughes, *The Finite Element Method: Linear Static and Dynamic Finite Element Analysis*, Prentice-Hall, Englewood Cliffs, New Jersey, 1987.

[51] E. Kausel and J. Tassoulas, "Transmitting boundaries: a closed-form comparison." *Bulletin of the Seismological Society of America*, Vol. 71, No. 1, pp. 143-159, 1981.

[52] R. Clayton and B. Engquist, "Absorbing boundary conditions for acoustic and elastic wave equations." *Bulletin of the Seismological Society of America*, Vol. 67, No. 6, pp. 1529-1560, 1977.

[53] J. Lysmer and R. L. Kuhlemeyer, "Finite dynamic model for infinite media." *Journal of the Engineering Mechanics Division*, ASCE, Vol. 95, pp. 859-877, 1969.

[54] W. D. Smith, "A nonreflecting plane boundary for wave propagation problems." *Journal of Computational Physics*, Vol. 15, pp. 492-503, 1973.

[55] W. White, S. Valliappan and I. K. Lee, "Unified Boundary for Finite Dynamic Models," *Journal of the Engineering Mechanics Division*, ASCE, Vol. 103 pp. 949-964, 1977.

[56] J. W. S. Rayleigh, *The Theory of Sound*, Vol. 1 and 2, Dover Publications, New York, 1945.

[57] G. R. Harris, "Review of transient field theory for a baffled planar piston," *Journal of the Acoustic Society of America*, Vol. 70, pp. 10-20, 1981

[58] D. A. Hutchins and G. Hayward, "Radiated fields of ultrasonic transducers," in *Physical Acoustics*, Vol. 19, pp. 1-81, eds. A. D. Pierce and R. N. Thurston, Academic Press, New York, 1990,

[59] H. Seki, A. A. Granato and R. Truell, "Diffraction effects in the ultrasonic field of a piston source and their importance in the accurate measurement of attenuation," *Journal of the Acoustic Society of America*, Vol. 28, No. 2, pp 230-238, 1956.

[60] E. P. Papadakis, "Diffraction of ultrasound radiating into an elastically anisotropic medium," *Journal of the Acoustic Society of America*, Vol. 36, No. 3, pp. 414-422, 1964.

[61] E. P. Papadakis, "Ultrasonic diffraction loss and phase change in anisotropic materials," *Journal of the Acoustic Society of America*, Vol. 40, No. 4, pp. 863-876, 1966.

[62] J. Zemanek, "Beam behavior within the near-field of a vibrating piston," *Journal of the Acoustic Society of America*, Vol. 49, pp. 181-191, 1971.

[63] E. P. Papadakis and K. A. Fowler, "Broad-band transducers: radiation field and selected applications," *Journal of the Acoustic Society of America*, Vol. 50, No. 3, pp. 729-745, 1971.

[64] P. R. Stephanishen, "Transient radiation from piston in an infinite planar baffle," *Journal of the Acoustic Society of America*, Vol. 49, pp. 1971.

[65] W. L. Beaver, "Sonic nearfields of a pulsed piston radiator," *Journal of the Acoustic Society of America*, Vol. 56, pp. 1043-1048, 1974.

[66] T. M. Mansour, "Evaluation of ultrasonic transducers by cross-sectional mapping of the near field using a point reflector," *Materials Evaluation*, Vol. 37. pp 50-54, 1979.

[67] E. P. Papadakis, "Use of computer model and experimental methods to design, analyze and evaluate ultrasonic NDE transducers," *Materials Evaluation*, Vol. 41, pp 1378-1388, 1983.

[68] A. Weyns, "Radiation field calculations of pulsed ultrasonic transducers," Part 1, *Ultrasonics*, Part 1, pp. 183-188, July 1980; Part 2, pp. 219-223, Sept. 1980.

[69] U. Aulenbacher and K. J. Langenberg, "Transient radiation pattern of ultrasonic transducers on elastic half-spaces," in *New Procedures in Nondestructive Testing*, ed. P. Holler, Springer, Berlin, 1983, pp. 81-92, 1983.

[70] C. Chang and W. Sachse, "Analysis of elastic wave signals from an extended source in a plate," *Journal of the Acoustic Society of America*, Vol. 77, pp. 1335-1341, 1985.

[71] H. L. Zhang, C. F. Ying and M. X. Li, "Direct wave and edge waves radiated by a circular thickness-mode transducer into a solid medium," *Proceedings of IEEE Ultrasonics Symposium*, pp. 897-890, 1983.

[72] K. Kawashima, "Quantitative calculation and measurement of longitudinal and transverse ultrasonic wave pulses in solid," *IEEE Transactions on Sonics and Ultrasonics*, Vol. SU-31, pp. 83-94, 1984.

[73] J. P. Weight, "A model for the propagation of short pulses of ultrasound in a solid," *Journal of the Acoustic Society of America*, Vol. 84, pp. 815-826, 1987.

[74] L. F. Bresse and D. A. Hutchins, "Transient generation of elastic waves in solids by a disk-shaped normal force source," *Journal of the Acoustic Society of America*, Vol. 86, pp. 810-817, 1989.

[75] L. W. Schmerr and A. Sedov, "An elastodynamic model for compressional and shear wave transducers," *Journal of the Acoustic Society of America*, Vol. 86, pp. 1988-1999, 1989.

[76] K. Harumi, T. Saito, and T. Fujimori, "Motion picture of the computer simulation of elastic waves from a transducer," in *Proceedings of the Secondary Congress of the Federal Acoustical Society of Europe,* Warsaw, pp. 51-60, 1978.

[77] A. Ilan and J. P. Weight, "The propagation of short pulses of ultrasound from a circular source coupled to an isotropic solid," *Journal of the Acoustic Society of America*, Vol. 88, pp. 1142-1151, 1990.

[78] F. Fellinger and K. J. Langenberg, "Numerical techniques for elastic wave propagation and scattering," in *Elastic waves and ultrasonic nondestructive evaluation*, eds. S. K. Datta, J. D. Achenbach and Y. S. Rajapakse, North-Holland, Amsterdam, pp. 81-86, 1990.

[79] L. J. Bond, "Numerical techniques and their use to study wave propagation and scattering - a review," in *Elastic Waves and Ultrasonic Nondestructive Evaluation*, eds. S. K. Datta, J. D. Achenbach and Y. S. Rajapakse, Elsevier Science, pp. 17- 27,1990.

[80] M. Sansalone, N. J. Carino and N. N. Hsu, "Finite element studies of transient waves Propagation," *Review of Progress in Quantitative Nondestructive*

Evaluation, Vol. 6A, eds. D. O. Thompson and D. E. Chimenti, pp. 125-133, 1987.

[81] B. R. Tittmann, "Scattering of elastic waves from simple defects in solids, a Review," *Wave Motion*, Vol. 5, pp. 299-306, 1983.

[82] B. R. Tittmann, E. R. Cohen and J. M. Richardson, "Scattering of longitudinal waves incident on a spherical cavity in a solid," *Journal of the Acoustic Society of America*, Vol. 63, pp. 68-74, 1978.

[83] C. F. Ying, S. Y. Zhang and J. Z. Shen, "Scattering of ultrasound in solids as visualized by the photoelastic technique," *Journal of the Acoustic Society of America*, Vol. 4, pp 65-73, 1984.

[84] K. J. Langenberg, U. Aulenbacher, G. Bollig and P. Fellinger, "Numerical modeling of ultrasonic scattering," in *Mathematical Modeling in NDT*, eds. M. Blakemore and G. A. Georgiou, pp. 125-173, Clarendon Press, Oxford, 1988.

[85] G. S. Kino, *Acoustic Waves: Devices, Imaging and Analog Signal Processing*, Prentice-Hall, Englewood Cliffs, New Jersey, 1987.

[86] W. Sachse, N. N. Hsu and D. G. Eitzen, "Visualization of transducer-produced source fields in solids," *Proceedings of IEEE Ultrasonics Symposium*, pp 139-143, 1978.

[87] G. C. Everstine, E. A. Schroeder, and M. S. Marcus, "The dynamic analysis of submerged structures," *NASTRAN: Users' Experiences*, NASA TM X-3278, pp. 419-429, 1975.

[88] G. C. Everstine, "A symmetric potential formulation for fluid-structure interaction," *Journal of Sound and Vibration*, Vol. 79, pp. 157-160, 1981.

[89] A. J. Kalinowski, "Fluid structure interaction," in *Shock and Vibration Computer Programs: Reviews and Summaries*, ed., W. Pilkey and B. Pilkey, The Shock and Vibration Information Center, US Department of Defense, pp. 405-452, 1975.

[90] A. J. Kalinowski and C. W. Nebelung, "Solution of axisymmetric fluid structure interaction problems with NASTRAN," *10th NASTRAN Users' Colloquium*, NASA, pp. 87-111, 1982.

[91] H. L. Bertoni and T. Tamir, "Unified theory of Rayleigh-angle phenomena for acoustic beams at liquid-solid interfaces," *Applied Physics*, Vol. 2, pp. 157-172, 1973.

[92] M. A. Breazeale, L. Adler, and G. W. Scott, "Interaction of ultrasonic waves incident at the Rayleigh angle onto a liquid-solid interface," *Journal of Applied Physics*, Vol. 48, pp. 530-537, 1977.

[93] L. Adler and G. W. Scott, "Applications of ultrasonic leaky waves in NDE," *Proceedings of IEEE Ultrasonics Symposium*, pp. 100-102, 1976.

[94] W. Parmon and H. L. Bertoni, "Ray interpretation of the material signature in the acoustic microscope," *Electronics Letters*, Vol. 15, pp. 684-686, 1979.

[95] K. Yamanaka, "Surface acoustic wave measurements using an impulsive converging beam," *Journal of Applied Physics*, Vol. 54, pp. 4323-4329, 1983.

[96] A. Macovski, "Ultrasonic imaging using arrays," *Proceedings of IEEE*, Vol. 67, no. 4, pp. 484-495, 1979.

[97] K. O. Peng and M. R. de la Fonteijie, "Quasi-paraxial field approximation for phased arrays," *Ultrasonic Imaging*, Vol. 11., pp. 260-272, 1989.

[98] R. H. Tancrell, J. Callerame, and D. T. Wilson, "Nearfield transient acoustic beam-forming with arrays," *Proceedings of IEEE Ultrasonics Symposium*, pp. 339-343, 1978.

[99] A. J. Duerinckx, "Modeling wavefronts from acoustic phased arrays by computer," *IEEE Transactions on Biomedical Engineering*, Vol. 28, pp. 221-234, 1981.

[100] U. Aulenbacher and K. J. Langenberg, "Analytical representation of transient ultrasonic phased-array near- and far-fields," *Journal of Nondestructive Evaluation*, Vol. 1, pp. 53-66, 1980.

[101] D. R. Dietz, S. J. Norton and M. Linzer, "Wideband annular array response," *Proceedings of IEEE Ultrasonics Symposium*, pp 206-211, 1978.

[102] D. R. Dietz, S. I. Parks and M. Linzer, "Expanding-aperture annular array," *Ultrasonic Imaging*, Vol. 1, pp. 56-75, 1979.

[103] M. Arditi, F. S. Foster, and J. W. Hunt, "Transient field of concave annular arrays," *Ultrasonic Imaging*, Vol. 3, pp. 37-61, 1981.

[104] L. G. Ullate and J. L. San Emeterio, "A new algorithm to calculate the transient near-field of ultrasonic phased arrays," *IEEE Transactions on Ultrasonics, Ferroelectrics and Frequency Control*, Vol. 39, no. 6, pp. 745-753, 1992.

[105] L. G. Ullate, A. Ramos and J. L. San Emeterio, "Analysis of the ultrasonic field radiated by time-delay cylindrically focused linear arrays," *IEEE Transactions on Ultrasonics, Ferroelectrics and Frequency Control*, Vol. 41, no. 5, pp. 749-760, 1994.

[106] R. D. Weglein and R. G. Wilson, "Characteristic material signatures by acoustic microscopy," *Electronics Letters*, Vol. 14, pp. 352-354, 1978.

[107] R. D. Weglein, "A model for predicting acoustic material signatures," *Applied Physics Letters*, Vol. 34, pp. 179-181, 1979.

[108] R. S. Gilmore, K. C. Tam, J. D. Young and D. R. Howard, "Acoustic microscopy from 10 to 100 MHz for industrial applications," *Philosophical Transactions of the Royal Society of London*, Vol. A320, pp. 215-235, 1986.

[109] J. M. R. Weaver, C. M. W. Daft and G. A. D. Briggs, "A quantitative acoustic microscope with multiple detection modes," *IEEE Transactions on Ultrasonics, Ferroelectrics and Frequency Control*, Vol. 36, pp. 554-60, 1989.

[110] A. Atalar, "An angular spectrum approach to contrast in reflection acoustic microscopy," *Journal Applied Physics*, Vol. 49, pp. 5130-5139, 1978.

[111] A. Atalar, "A physical model for acoustic signatures," *Journal of Applied Physics*, Vol. 50, pp. 8237-8239, 1979.

[112] J. Kushibiki, A. Ohkubo and N. Chubachi, "Theoretical analysis for V(z) curves obtained by acoustic microscope with line-focus beam," *Electronics Letters*, Vol. 18, pp. 663-664, 1982.

[113] J. Kushibiki, A. Ohkubo and N. Chubachi, "Theoretical analysis of V(z) curves measured by acoustic line-focus beam," *Proceedings of IEEE Ultrasonics Symposium*, pp. 623-628, 1982.

[114] M. G. Somekh, H. L. Bertoni, G. A. D. Briggs and N. J. Burton, "A two-dimensional imaging theory of surface discontinuities with the scanning acoustic microscopy," *Proceedings of the Royal Society London*, Vol. A401, pp. 29-51, 1985.

[115] C. J. R. Sheppard and T. Wilson, "Effects of high angles of convergence on V(z) in the scanning acoustic microscope," *Applied Physics Letters*, Vol. 49, pp. 858-8599, 81.

[116] H. L. Bertoni, "Ray-optical evaluation of V(z) in the reflection acoustic microscope," *IEEE Transactions on Sonics and Ultrasonics*, Vol. 31, pp. 105-116, 1984.

[117] K. H. Chan and H. L. Bertoni, "Ray representation of longitudinal lateral waves in acoustic microscopy," *IEEE Transactions on Ultrasonics, Ferroelectrics and Frequency Control*, Vol. 38, pp. 27-34, 1991.

[118] J. Kushibiki, T. Sannomiya and N. Chubachi, "Broad bandwidth concave transducer for scanning acoustic microscope," *Electronics Letters*, Vol. 17, pp. 663-664, pp. 42-44, 1981.

[119] H. L. Bertoni and M . G. Somekh, "Ray-optical analysis of spherical focusing transducers for acoustic microscopy," *Proceedings of IEEE Ultrasonics Symposium*, pp. 715-719, 1982.

[120] Y. Sugawara, J. Kushibiki and N. Chubachi, "Performance of concave transducers in acoustic microscopy," *Proceedings of IEEE Ultrasonics Symposium*, pp. 623-628, 1982.

[121] K. K. Liang, G. S. Kino and B. Khuri-Yakub, "Material characterization by the inversion of V(z)," *IEEE Transactions on Sonics and Ultrasonics*, Vol. 32, pp. 213-224, 1985.

[122] J. Kushibiki and N. Chubachi, "Material characterization by line-focus-beam acoustic microscope," *IEEE Transactions on Sonics and Ultrasonics*, Vol. 32, pp. 189-212, 1985.

[123] J. D. Achenbach, V. S. Ahn and J. G. Harris, "Wave analysis of the acoustic material signature for the line focus microscope," *IEEE Transactions on Ultrasonics, Ferroelectrics and Frequency Control*, Vol. 38, pp. 380-387, 1991.

[124] V. S. Ahn, J. G. Harris and J. D. Achenbach, "Numerical analysis of the acoustic signature of a surface-breaking crack," *IEEE Transactions on Ultrasonics, Ferroelectrics and Frequency Control*, Vol. 39, pp. 112-118, 1991.

[125] V. S. Ahn, J. D. Achenbach, Z. Li and J. O. Kim, "Numerical modeling of the V(z) curve for a thin-layer/substrate configuration," *Research in Nondestructive Evaluation*, Vol. 3, pp. 183-200, 1991.

[126] R. A. Roberts, "Model of the acoustic microscope response to scattering by a near- surface void," *Journal of Nondestructive Evaluation*, Vol. 9, pp. 181-196, 1990.

[127] J. R. Winkler and J. B. Davies, "Accurate field analysis of the propagation of elastic waves through an acoustic microscope, Part 1 and 2," *IEEE Transactions on Ultrasonics, Ferroelectrics and Frequency Control*, Vol. 33, pp. 644-668, 1986.

[128] A. Briggs, ed., *Advances in Acoustic Microscopy* , Plenum, New York, 1995.

ACKNOWLEDGEMENTS

I would like to thank my major professor Dr. William Lord and Dr. Satish Udpa for their guidance and support throughout this project. They provided me the opportunity to work in an exciting research group and environment. I would also like to thank Dr. Lalita Udpa, Dr. H. C. Hsieh and Dr. L. W. Schmerr for their enthusiasms to serve as my committee members. In addition, I wish to thank Dr. Mani Mina for his encouragement and cooperation. The sponsorship of Takano Corporation is greatly appreciated.